Final Report to

RPSEA

Research Partnership to Secure Energy for America

Improved Drilling and Fracturing Fluids for Shale Gas Reservoirs

09122-41.FINAL

June 2014

Principal Investigator:
Mukul M. Sharma

Participants:
Martin E. Chenevert, Changmin Jung, Junhao Zhou

The University of Texas at Austin
200 E. Dean Keeton St. Stop C0300
Austin, Texas 78712
(512) 471-3257
msharma@mail.utexas.edu

LEGAL NOTICE

This report was prepared by The University of Texas at Austin as an account of work sponsored by the Research Partnership to Secure Energy for America, RPSEA. Neither RPSEA members of RPSEA, the National Energy Technology Laboratory, the U.S. Department of Energy, nor any person acting on behalf of any of the entities:

a. MAKES ANY WARRANTY OR REPRESENTATION, EXPRESS OR IMPLIED WITH RESPECT TO ACCURACY, COMPLETENESS, OR USEFULNESS OF THE INFORMATION CONTAINED IN THIS DOCUMENT, OR THAT THE USE OF ANY INFORMATION, APPARATUS, METHOD, OR PROCESS DISCLOSED IN THIS DOCUMENT MAY NOT INFRINGE PRIVATELY OWNED RIGHTS, OR

b. ASSUMES ANY LIABILITY WITH RESPECT TO THE USE OF, OR FOR ANY AND ALL DAMAGES RESULTING FROM THE USE OF, ANY INFORMATION, APPARATUS, METHOD, OR PROCESS DISCLOSED IN THIS DOCUMENT.

THIS IS A FINAL REPORT. THE DATA, CALCULATIONS, INFORMATION, CONCLUSIONS, AND/OR RECOMMENDATIONS REPORTED HEREIN ARE THE PROPERTY OF THE U.S. DEPARTMENT OF ENERGY.

REFERENCE TO TRADE NAMES OR SPECIFIC COMMERCIAL PRODUCTS, COMMODITIES, OR SERVICES IN THIS REPORT DOES NOT REPRESENT OR CONSTIITUTE AND ENDORSEMENT, RECOMMENDATION, OR FAVORING BY RPSEA OR ITS CONTRACTORS OF THE SPECIFIC COMMERCIAL PRODUCT, COMMODITY, OR SERVICE.

M. M. Sharma June 30, 2014

Mukul M. Sharma Date
Principal Investigator

Abstract

Shales account for 75% of all footage drilled and are responsible for 90% of wellbore stability problems. This issue becomes even more important when long horizontal wells are drilled into shale formations to produce oil and gas. Maintaining wellbore stability is one of the most critical aspects of a successful drilling and completion program. The main cause of shale instability for both soft and hard shales is water absorption and subsequent swelling and sloughing of the wellbore. The wellbore pressure penetrates into the shale pore space when water invades the shale. This increase in pore pressure is the primary cause of shale failure and wellbore instability.

Even though a good bit of research has focused on improving wellbore stability with specially engineered water-based muds, no such inhibitive mud currently exists. We have shown in past work that the average pore throat size of a variety of shales ranges from 10 to 30 nanometers (0.01 to 0.03 microns). Compared with shale pore throat sizes, commonly used drilling fluid additives such as bentonite and barite, have much larger particle diameters, in the range of 100 nm to 10,000 nm. The extremely low permeability and small pore throat size observed in shales is such that conventional filtration additives do not form mud cakes and thus do not stop fluid invasion.

In this research we have shown for the first time that the use of nanoparticles in water-based drilling fluids can significantly reduce water invasion into shales and thereby improve wellbore stability. To the best of our knowledge, the use of nanoparticles in drilling fluids is the first potential large scale application of nanoparticles in the oil and gas industry. We investigated adding various commercial surface-treated and non-treated silica nanoparticles which sizes varying from 5 nm to 22 nm to both laboratory and field drilling fluids to see whether it was possible to reduce the permeability of shales by a significant amount. Among all the nanoparticles tested, it was found that 20nm surface-treated silica nanoparticles were the most effective at both remaining stable in water-based field muds and also at reducing the filtrate invasion into the shale.

We have also investigated the use of nanoparticle stabilized foams for the reduction in permeability of the shale. The increased stability of the foam due to the addition of NP's decreases the amount of liquid contacting the shale surface by adding resistance to the breaking of the bubbles in the foam. Similarly to the surfactant used as the foaming agent, the NP's enhance the exclusion of water contacting the shale surface by forming stable bubbles in the foam. The bubbles cannot enter the pore throats due to the higher entrance pressure of nitrogen into the pores of the shale. Another possible mechanism for the reduction of permeability for NP enhanced foam is the plugging of pores by the NP's in the liquid phase of the foam. The liquid that does enter the pore throats contains NP's and has been shown to plug the pore throats of the shale. The physical blocking of the pore throats restricts the flow of water into the pores of the shale. Nanoparticle enhanced foams lower the permeability of both outcrop and reservoir shale formations. These tests clearly indicate that this technology is applicable to both drilling and fracturing fluids. The use of foams has the added advantage that that the volume of water used is reduced dramatically and the amount of nanoparticles used is reduced by an order of magnitude.

One of the primary challenges facing us in studying shales was that traditional methods for measuring rock petrophysical properties could not be directly applied to shales. Measurements of basic properties such as porosity and permeability could not be conducted using standard

protocols. As such, new methods and modifications to existing methods were developed to reliably measure these properties in shales, which have permeabilities in the nano-Darcy range. In addition new methods are presented for core recovery, preparation and analysis that focus on keeping the shale in it native "preserved" state. This report summarizes the sample preparation protocols and experimental procedures that we have developed and that proved to be invaluable in working with both non-hydrocarbon bearing and organic rich shales.

The two major concerns during drilling and completion of wellbores in unconventional reservoirs are: wellbore instability and proppant embedment. Both of these issues are controlled by the interaction of water-based fluids with the organic-rich shale. Understanding the interaction of water-based fluids with organic-rich shales is the first step towards developing screening tests for their compatibility with the shale. We present a systematic approach to investigate the interaction of water-based drilling and fracturing fluids with organic-rich shales.

We performed a series of measurements to determine shale mineralogy, native water activity, swelling parallel and perpendicular to bedding planes, Brinell hardness, P-wave and S-wave velocities. Changes in hardness and acoustic wave velocities were measured before and after shale samples came into contact with water-based fluids. Shale swelling was determined in two directions simultaneously with our unique 2-D strain indicators. The dynamic Young's modulus and Poisson's ratio were calculated based on the wave velocities. It is shown that these measurements can be used to screen drilling and completion fluids that may interact unfavorably with the shale.

The shale mineralogy was obtained using XRD. The shale native water activity was determined with controlled humidity environments. Multi-scale durometers were used to measure the shale hardness. Anisotropic swelling was observed for all shale samples characterized. The results showed a good correlation with the mineralogy, hardness and wave velocities of the shale. In general, the water adsorption was greater with fresh water than with 4% NaCl and 2% KCl. Changes in hardness, P-wave and S-wave velocities, dynamic Young's modulus and Poisson's ratio after shale's contact with water-based fluids can be used as indicators for wellbore stability and fracture conductivity impairment in these shales.

The measurement techniques and procedures presented in this report can be used as standard screening tests to evaluate the interaction between organic-rich shales and water-based drilling and fracturing fluids. If this testing protocol shows incompatibility of the fluids with the shale, additional fracture conductivity tests should be conducted. The screening protocol presented here minimizes the number of fracture conductivity measurements (that are hard to perform) that need to be conducted to check for shale-fluid compatibility.

Table of Contents

Abstract 5
Table of Contents 7
Executive Summary 10
Chapter 1. Introduction 11
Chapter 2: Experimental Setup, Procedures and Shale Sample Preparation 12
2.1 Shale Handling and Preservation 12
2.2 Sample Preparation 13
2.3 Shale Mineralogy 14
2.4 Native Water Activity 14
2.5 Shale Swelling Test 15
2.6 Brinell Hardness 15
2.7 Acoustic Wave Velocity 16
2.8 Shale Permeability using the Pressure Penetration Test (PPT) 17
2.9 References 19
Chapter 3: Shale Characterization 20
Chapter 4: Use of Nanoparticles for Maintaining Shale Stability 23
4.1 Nanoparticle Properties 23
4.2 Preliminary Plugging and Swelling Tests 24
4.3 Multi-step Tests 24
4.4 Nanoparticle Concentration Tests 27
4.5 Scanning Electron Micrographs 31
4.6 Nanoparticle Type and Size Tests 33
Chapter 5: Decreasing Water Invasion into Atoka Shale Using Silica Nanoparticles 35
5.1. Introduction 35
5.2. Experimental methods 36
5.2.1 Materials used 36
5.2.1.3 Muds used 37
5.2.2 Test equipment for measuring shale permeability 38
5.2.3 Experimental procedures 38
5.3. Results and Discussion 38

5.3.1 Thermal stability tests on fresh water mud containing NPs 38
5.3.2 Rheology of NP containing muds 39
5.3.3 Filtration of NP containing muds 39
5.3.4 Changes in shale permeability with the addition of NPs 40
5.3.5 Effect of mud composition on shale permeability 40
5.3.6 Potential for Field Application 42
5.4. Conclusions 42
5.5 Nomenclature 42
5.6 References 43
Chapter 6: Use of Nanoparticles in Field Muds 49
6.1 Field Mud Properties 49
6.2 Field Muds in contact with Atoka shale 50
6.3 Field Muds in contact with GOM shale 62
6.4 Conclusions 76
Chapter 7: High Performance Nanoparticle Water-based Drilling Fluids for Organic Rich Shales 78
7.1 The Properties of water-base mud 79
7.2 Permeability measurement results 79
Chapter 8: A New Standardized Protocol for Evaluating the Interaction of Drilling and Fracturing Fluids with Hydrocarbon Bearing Shales 83
8.1 Introduction 83
8.2 Experimental Procedures 84
8.3 Results and Discussion 85
8.3.1 Shale Swelling 85
8.3.2 Brinell hardness 89
8.3.3 Acoustic wave velocity 90
8.3 References 93
Chapter 9: The Impact of Shale Preservation on Shale Petrophysical Properties 94
9.1 Introduction 94
9.2 Lab Evaluation of Eagle Ford Shale 94
9.2.1 Original Fluid Content and Physical Properties of Eagle Ford Shale 94
9.2.2 Swelling Effect on Eagle Ford Shale 95
9.3 Sample Preparation 95
9.3.1 Weight Change Measurement 96

9.3.2 Brinell Hardness Test 96
9.3.3 Wave Velocity Measurement 97
9.4 Permeability Measurements 99
9.4.1 Pressure Penetration Technique (PPT) 99
9.4.2 Sea water Permeability Measurement 99
9.4.3 Nitrogen Permeability Measurement 100
9.4 Conclusions 101
9.5 References 101
Chapter 10: Using Nanoparticle Stabilized Foams to Achieve Wellbore Stability in Shales 103
10.1 Abstract 103
10.2 Introduction 103
10.3 Development of Methodology 105
10.4 Experimental Setup 106
10.5 Experimental Procedures 110
10.5.1 Screen Wire Construction 111
10.5.2 Foam and Foam with NP's Pressure Penetration Test 111
10.5.3 Foam Stability Test 112
10.6 Results and Discussion 112
10.6.1 Results 112
10.6.2 Discussion 127
10.7 Conclusions 134
10.8 References 135
Appendix A – Technology Transfer 136
List of Tables 138
List of Figures 140

Executive Summary

The development of shale gas plays is largely dependent on the cost of drilling and fracturing horizontal wells. Rapid decline rates require that new wells be drilled just to maintain production. A reduction in the cost and environmental footprint of drilling and fracturing will have a significant impact on the economics of unconventional hydrocarbon development. This project aims at developing materials and methods for substantially reducing drilling and completion costs and maximizing oil and gas well productivities in unconventional reservoirs. Our primary goal is to reduce the costs and the environmental impact of drilling. To achieve this we have developed nanoparticle additives for water-based drilling fluids that inhibit water invasion into shales, thereby improving wellbore stability in reactive, hydrocarbon-bearing shales and that cost a lot less than the oil-based fluids being used today.

Shales often have a high clay content that can cause wellbore stability problems that necessitate the use of oil-based fluids for drilling. This significantly increases drilling costs and the environmental footprint. Research presented in this report shows that the addition of nanoparticles (in the size range of the pore throats of the shale) to the drilling fluid results in a dramatic reduction in the reactivity of the shale with the drilling fluid. The use of such fluids provides a significant cost savings when drilling water-sensitive shales with water-based fluids without the danger of wellbore collapse.

Finally, in hydrocarbon bearing shales that contain water sensitive clays, it may be desirable to minimize or eliminate contact with a water based fluid. Energized fracturing fluids, such as CO_2 foams, provide a way to accomplish this. The interaction of nanoparticle stabilized energized fluids, such as foams, with shales was studied and the potential benefits quantified. The use of nanoparticles improves foam stability and reduces both the need for water and the quantity of nanoparticles needed to prepare drilling and fracturing fluids.

In summary, this report presents results for novel drilling fluids for water-sensitive shales that have the potential to significantly reduce the cost of drilling horizontal wells in hydrocarbon bearing shale reservoirs. Data is presented to show the effectiveness of these fluids in reducing water and ion invasion into shales, thereby resulting in more stable wellbores. The use of such water-based fluids with nanoparticle additives is expected to both reduce costs and the environmental footprint of drilling operations.

Chapter 1. Introduction

Maintaining wellbore stability is one of the most critical aspects of drilling. With the increasing use of horizontal wells, wellbore stability issues have become even more acute and important. Water invasion into the shale formation weakens the wellbore and causes problems such as hole-collapse, and stuck pipe. The extremely low permeability and low pore throat size of shale is such that normal filtration additives do not form mud cakes and thus do not stop fluid invasion. This research aims to reduce water invasion into shales during drilling and fracturing by using nanoparticles to plug pore throats, build an internal mud cake and thereby reduce the influence of fluid invasion into the shale.

Balanced activity oil-continuous muds are a good solution to the shale stability problem since there is very little chemical interaction between oil and shale, and the water in the mud is only present as emulsified saline water droplets.[2] However, water-based muds (WBM) may be needed in environmentally sensitive areas and in areas where surface disposal of oil-covered drill-cuttings is an issue. Even though there have been many studies that focus on improving the hole stability properties of water-based muds, no such inhibited mud exists for shales. It is thought that pore throat plugging has not been achieved in the past because the size of the solid mud additives currently used is too large to plug nanometer sized pore throat openings in shales.

A statement of the problem and the basic physical properties of the shales, nanoparticles, and muds used in this study are presented first (Chapters 2 and 3). Test procedures developed and used in the experiments to evaluate nanoparticles are presented next (Chapter 4). The results of the tests conducted using shales and lab muds containing nanoparticles are presented in Chapter 5. The results of the field mud tests with and without nanoparticles are presented for Atoka and Gulf of Mexico shales in Chapter 6. Results are compared for each field mud to show the effect of nanoparticles for both Atoka and Gulf of Mexico shales. Results for some preserved organic rich shales are presented in Chapters 7 and 8. In Chapter 9 the use of preserved shale samples in all laboratory tests is shown to be critical to the results obtained. Methods to preserve shales and their handling in the lab are described in detail. Finally, the use of water-based foams is suggested as a way of reducing water and nanoparticle usage in drilling and fracturing fluids in Chapter 10.

Chapter 2: Experimental Setup, Procedures and Shale Sample Preparation

One of the primary challenges facing us in studying shales was that traditional methods for measuring rock petrophysical properties could not be directly applied to shales. Measurements of basic properties such as porosity and permeability could not be conducted using standard protocols. As such, new methods and modifications to existing methods were developed to reliably measure these properties in shales, which have permeabilities in the nano-Darcy range. In addition new methods are presented for core recovery, preparation and analysis that focus on keeping the shale in it native "preserved" state. This chapter summarizes the sample preparation protocols and experimental procedures that we have developed and that proved to be invaluable in working with both non-hydrocarbon bearing and organic rich shales.

Table 2.1 summarizes the measurements conducted and the shale sample requirements in the proposed laboratory protocol. Shale mineralogy, native water activity, swelling perpendicular and parallel to bedding planes, Brinell hardness and acoustic wave velocity were measured. The native shale properties and changes in mechanical properties when the shale is brought into contact with water-based fluids will be the focus of this procedure. The experimental setup, procedures and shale sample preparation protocol will be described in more detail in this chapter.

Table 2.1: Summary of experimental measurements made on shales and the corresponding sample requirements

Measurement	Equipment	Sample Dimension	Expected Results
Mineralogy	X-ray diffraction (XRD)	Small pieces	Percentage composition of minerals such as quartz, calcite and clay.
Native water activity	De-aerated desiccators with saturated salt solutions	Small pieces	The relative humidity that gives no weight change is the native shale water activity.
Swelling in two directions	2-D swelling indicator	1" cube	Swelling percentage as a function of time with water-based fluids.
Brinell hardness	Multi-scale durometer	1" cube	Durometer readings are converted to hardness scales.
Acoustic wave velocity	Ultrasonic wave propagation set-up	1" cube	P-wave and S-wave velocities are converted from wave travel time observed.
Shale permeability	Pressure penetration test (PPT)	2.5" diameter and 0.25" thick disk	Permeability calculated from the change of bottom pressure as a function of time.

2.1 Shale Handling and Preservation

It is imperative that preserved shale samples be used in all of the tests described in Table 2.1. This is because prolonged exposure of a shale to the atmosphere will alter the shale mechanical and flow properties irreversibly (Chenevert, 1970). Shale will gain or lose water depending on its hydration state relative to the surrounding atmosphere. Measurements using unpreserved shales will not yield reliable results that are representative of downhole shale properties. While it is difficult to get high quality preserved shale cores from the field it is very important that great care be taken when the shale is cored and stored in the field and in the laboratory.

Upon receiving preserved shale samples from the field, we prepare and process these samples in a water-free environment. Oil-cooled coring machines are used to cut the cores into a desired size. Specifically, swelling, changes in Brinell hardness and acoustic wave velocity are measured with a cube of shale 1" edge length. The prepared shale cubes and unused remaining

cores are stored in cans filled with mineral oil to minimize exposure to the atmosphere. When the native water activity of the shale is determined later, these samples can also be placed in the desiccator with the appropriate controlled humidity environments.

2.2 Sample Preparation

We have found that in our experience it is often difficult to core preserved shales. The circular motion of the saw causes cracks and shearing of the shale and this results in low sample recovery. Our procedure shown in Table 2.1 minimizes this problem by avoiding the use of cylindrical cores. The samples used are rectangular or cubic so that they can be more easily cut using a straight cut with a precision saw. This significantly increases sample recovery. Figure 2.1 shows two coring machines for cutting shale samples. Figure 2.2 shows an example of the three types of sample prepared. Figure 2.3 illustrates the sample preparation procedure for the permeability test.

Figure 2.1: Oil-cooled coring machines to cut large (left) and small (right) shale samples.

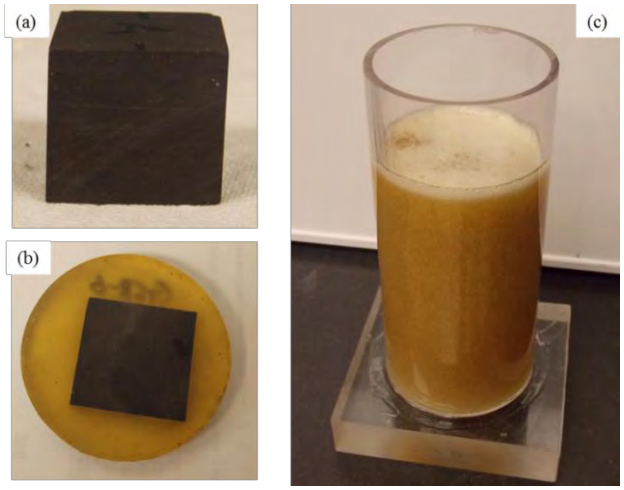

Figure 2.2: Shale samples prepared for characterization: (a) a cube, (b) a disk, and (c) a column.

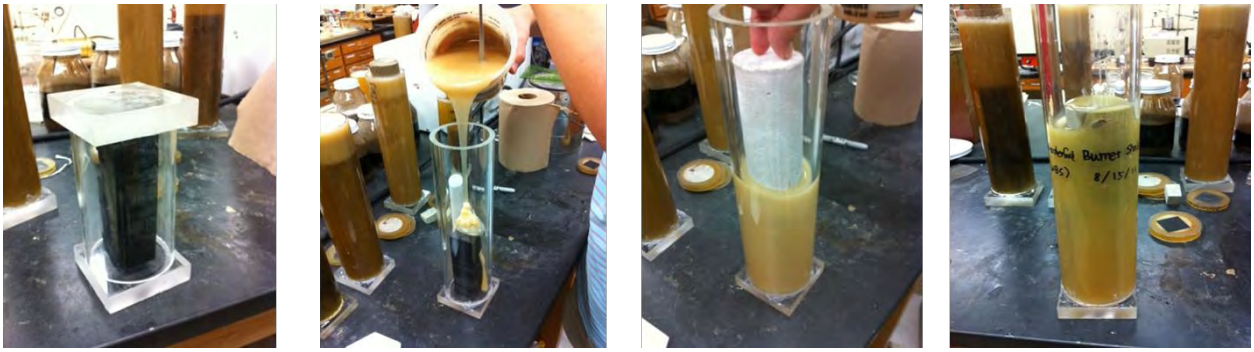

Figure 2.3: Sample preparation procedure for the permeability test.

2.3 Shale Mineralogy

The shale mineralogy is determined with X-ray diffraction and X-ray fluorescence. The crystalline structure of individual minerals can be identified through their angles of diffraction of X-ray beams (Breeden and Shipman, 2004). The diffraction patterns can also be used to quantify the percent composition of individual minerals. We are particularly interested in the composition of quartz, calcite and different types of clay. These minerals are directly related to shale mechanical properties and shale's sensitivity with water-based fluids.

2.4 Native Water Activity

The shale native water activity represents its original hydration state. It is an important fundamental property of shale and is directly related to the performance of drilling and fracturing fluids. It is determined with controlled humidity environments created by saturated salt solutions in de-aerated desiccators (Winston and Bates, 1960). This method ensures that only moisture enters or leaves the shale with no ion movement. The saturated salt solutions and their respective relative humidities are shown in Table 2.2. These solutions cover a wide range of relative humidity.

Shale samples from the same core are placed in desiccators with different relative humidities. The weight change of these samples due to water movement is recorded as a function of time. Equilibrium is usually reached after 7 to 10 days. The relative humidity that results in no weight change overall is the shale native water activity. Figure 2.4 shows a plot of percent weight change as a function of relative humidity for determining the native water activity of a shale.

Table 2.2: Saturated salt solutions and their respective relative humidity

Saturated Salt Solution	Relative Humidity
$K_2Cr_2O_7$	98%
KH_2PO_4	96%
KNO_3	92%,
KCl	85%
NaCl	75.5%
$Ca(NO_3)_2$	50.5%
$ZnCl_2$	10%

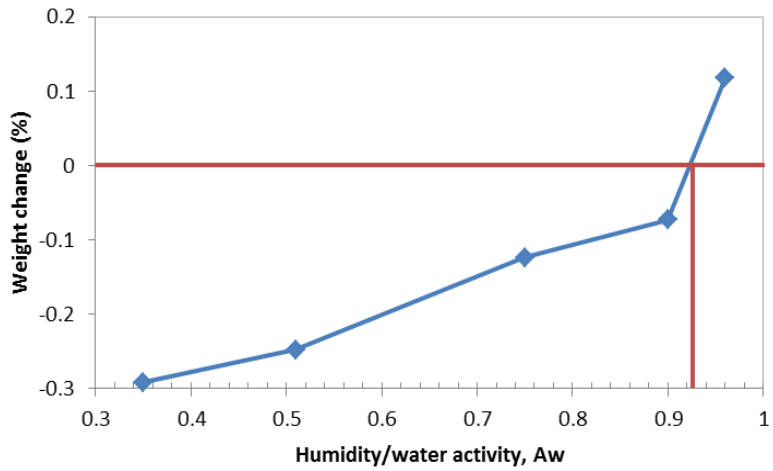

Figure 2.4: Adsorption isotherm test to determine shale's native water activity.

2.5 Shale Swelling Test

The shale swelling test is an effective technique to check the sensitivity of shales to water-based fluids. Strain indicators are used to measure directional swelling of shales when they are immersed in the fluid of interest. The strain induced by interaction with water-based fluids causes a change in electrical resistance, which is measured with a Wheatstone bridge. Swelling in two directions, perpendicular and parallel to bedding planes can be measured with our unique 2-D strain indicator as a function of time. For convenience, cubic shale samples of 1" edge length are used in all swelling tests. Shale hardness and acoustic wave velocities are also measured before and after the swelling tests to investigate the effect of shale-fluid interaction on the mechanical properties changes. Figure 2.5 is the side view of one swelling gauge set-up in one direction. The results reported here were for tests conducted at ambient temperature but the test can be conducted at elevated temperature as well.

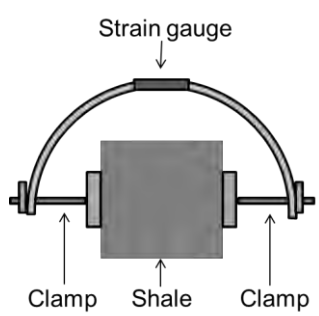

Figure 2.5: Side view of one swelling gauge with shale sample.

2.6 Brinell Hardness

The Brinell hardness of hydrocarbon bearing shales is a very important mechanical property related to wellbore stability and proppant embedment in shale reservoirs. Shales with higher Brinell hardness after contact with drilling and fracturing fluids tend to experience less wellbore stability and proppant embedment problems. The Brinell hardness is determined with an indentation method, originally proposed in Sweden in 1900 (Brinell, 1900). A multi-scale

durometer is used to measure the Brinell hardness of shales. The durometer is equipped with different gauges that can be used on surfaces of different hardness. The shale hardness is typically measured with a type D gauge. Multiple readings are taken on the same surface and averaged. The average reading is then converted to the Brinell scale. For the purpose of investigating fluid sensitivity of shales, Brinell hardness was measured before and after the shale came into contact with a water-based fluid.

2.7 Acoustic Wave Velocity

The acoustic wave velocity is related to the strength of shales. The P-wave (compressional wave) and S-wave (shear wave) velocities of shales are measured with a pulse transmission set-up (Figure 2.6), which consists of a pulser-receiver and an oscilloscope. A viscous coupling agent is needed to make contact between the shale surface and the two transducers. Molasses has been proven to be a good coupling agent. The wave velocities are calculated with the transmission time shown on the oscilloscope. The P-wave and S-wave velocities are measured perpendicular and parallel to bedding planes.

The dynamic Young's modulus and Poisson's ratio can then be calculated from the wave velocities of shales using Eq. (2-1) and Eq. (2-2).

$$E = \frac{v_s^2 \rho \left[3\left(\frac{v_p}{v_s}\right)^2 - 4\right]}{\left[\left(\frac{v_p}{v_s}\right)^2 - 1\right]} \tag{2-1}$$

$$\nu = \frac{1}{2}\frac{\left[\left(\frac{v_p}{v_s}\right)^2 - 2\right]}{\left[\left(\frac{v_p}{v_s}\right)^2 - 1\right]} \tag{2-2}$$

Where E is the Young's modulus, ν is Poisson's ratio, ρ is density of the shale, v_p is the P-wave velocity and v_s is the S-wave velocity.

Similar to the Brinell hardness measurement, acoustic wave velocities of shale are measured before and after contact with water-based fluids to investigate the effect of shale-fluid interaction.

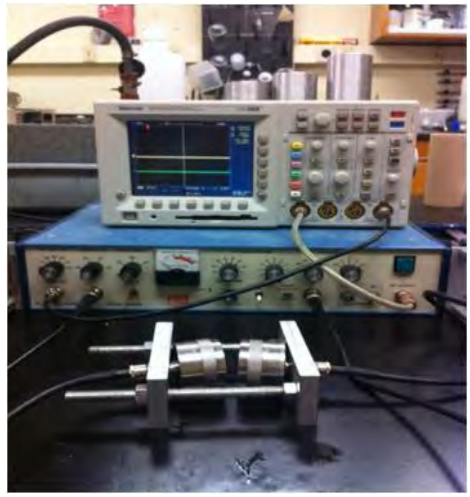

Figure 2.6: Pulse transmission set-up for measuring the acoustic wave velocities of shales.

2.8 Shale Permeability using the Pressure Penetration Test (PPT)

Pressure penetration technique (PPT) tests have been performed to investigate the effect of physical plugging by nanoparticles. Using this technique, we measure the permeability of shale samples in contact with various kinds of fluids: brine, base mud, and base mud with various concentrations of nanoparticles. We measure the shale permeability with 4% NaCl brine first, as a reference permeability, and then test with base mud and nanoparticle mud to observe the change in permeability. A reduction in permeability means that the water invasion into the shale will be reduced, and shale will be more stable when exposed to such drilling fluids.

Figure 2.7 shows the schematic experimental set-up for the pressure penetration test. The experimental set-up consists of several devices used to achieve a continuous flow of the test fluid across the top face of the shale sample. At a constant upstream pressure, a test fluid flows across the top of a shale sample. In a small sealed chamber beneath the shale sample, the fluid pressure build-up is recorded. This test is referred to as the unsteady state method. A transient pressure model is used for calculating the sample permeability. (Al-Bazali et al, 2006).

$$\ln\left(\frac{P_2 - P_1}{P_2 - P_0}\right) = -\frac{Ak}{\mu cVL}t \quad \rightarrow \quad k = -\left[\frac{\ln\left(\frac{P_2 - P_1}{P_2 - P_0}\right)}{t}\right]\frac{\mu cVL}{A} = -(\text{slope}) \times \frac{\mu cVL}{A}$$

where:

P_2: upstream driving pressure, P_1: downstream build-up pressure
P_0: downstream initial pressure, A: sample cross sectional area
k: permeability, μ: viscosity
c: compressibility factor, V: beneath sealed chamber volume
L: sample thickness, t: time

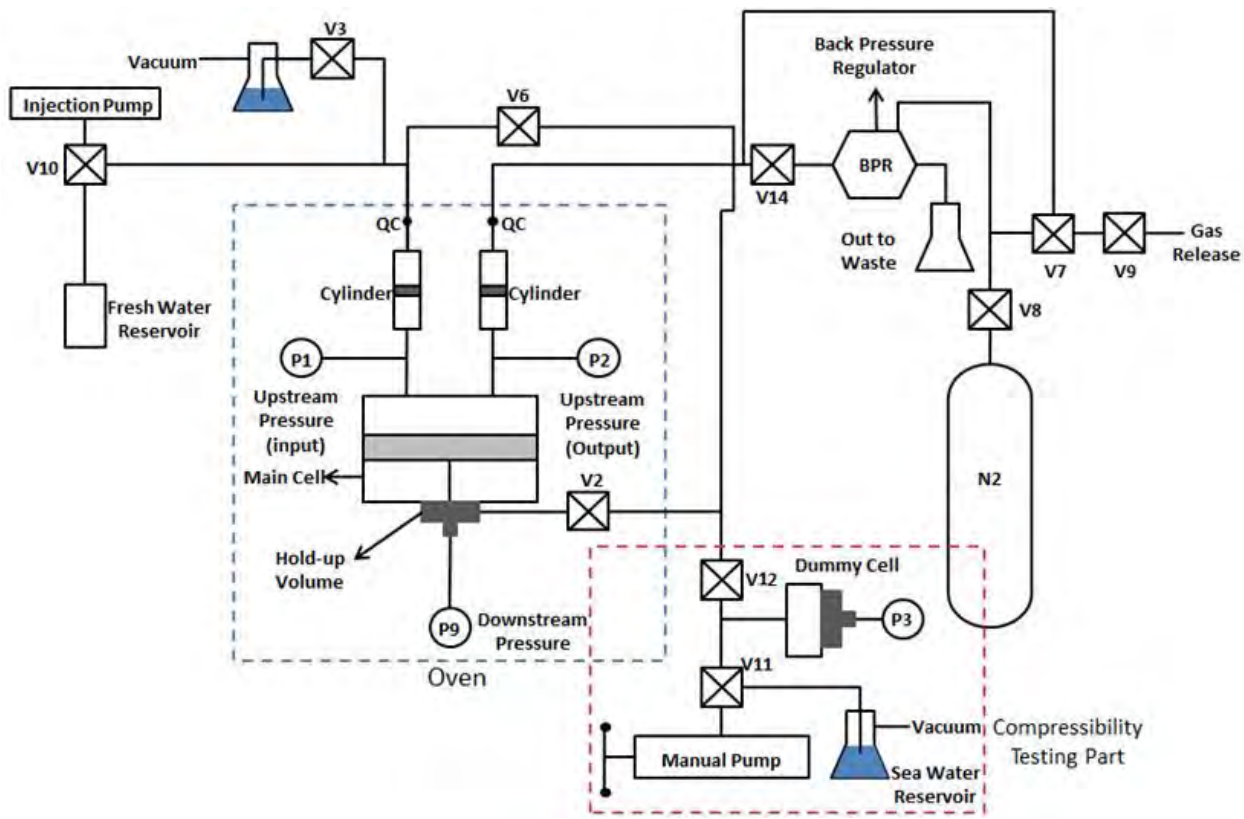

Figure 2.7: Pressure penetration test and compressibility test set-up.

Figure 2.8 shows a typical downstream pressure build-up result and slope interpretation graph of dimensionless pressure versus time. The slope of dimensionless pressure versus time is used in the transient pressure model. We calculate the slope of part of the data that is red-labeled to calculate the permeability.

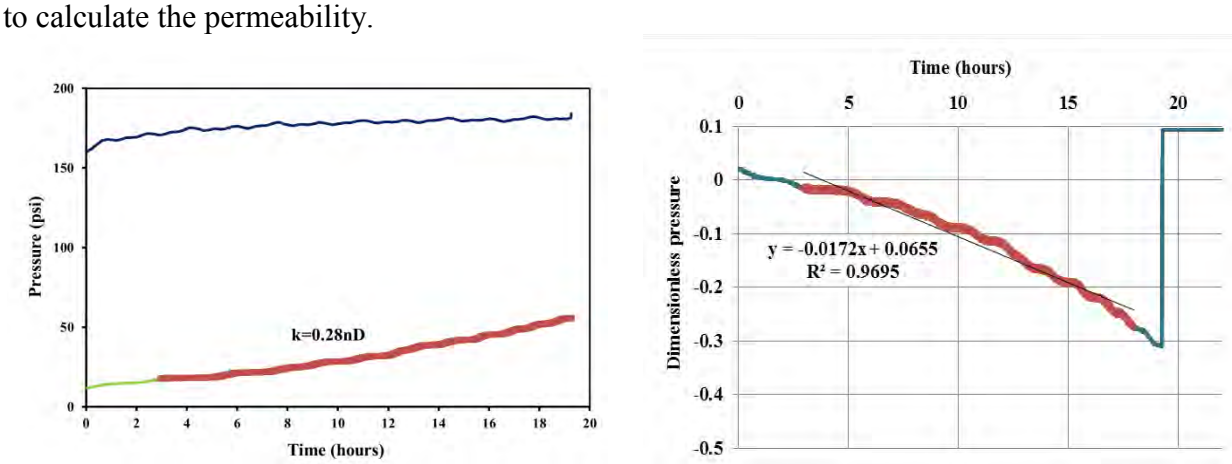

Figure 2.8: Downstream pressure build-up and graphical slope interpretation of dimensionless pressure versus time.

We have the dimensions of the sample and also the fluid viscosity, the compressibility factor is only thing we need to know for the permeability calculation. Figure 1 shows the compressibility testing part of the PPT set-up. To measure the compressibility of brine in the

bottom chamber, a dummy cell with a pressure transducer is attached for the compressibility testing. The system pressure is increased using a manual hand pump. Using the pressure versus injecting volume data, we can calculate the average compressibility of our system. Figure 2.9 shows a typical compressibility test result.

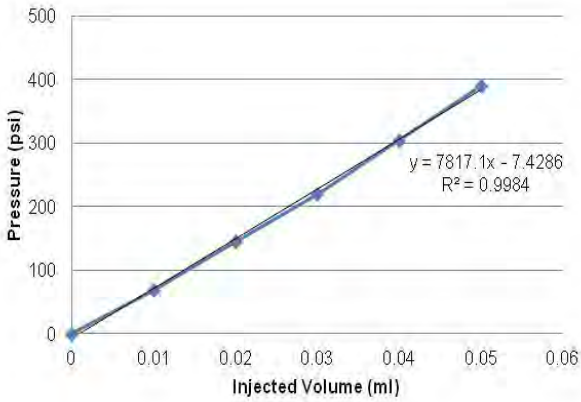

$$c = -\frac{1}{V} \times \frac{(V_1 - V_2)}{(P_1 - P_2)} = -\frac{1}{V} \times \frac{1}{(\text{slope})}$$

where:

- c : compressibility
- V : reference volume
- V_1 : initial volume
- V_2 : final volume
- P_1 : initial pressure
- P_2 : final pressure

Figure 2.9: Brine compressibility test result and compressibility calculation equation.

2.9 References

Al-Bazali, T.M., Zhang, J., Chenevert, M.E., and Sharma, M.M. 2006. Factors Controlling the Membrane Efficiency of Shales When Interacting with Water-Based and Oil-Based Muds, SPE 100735 presented at the International Oil & Gas Conference and Exhibition in Beijing, China, December 5 – 7.

Breeden, D., Shipman, J. 2004. Shale Analysis for Mud Engineers. AADE-04-DF-HO-30 presented at the AADE 2004 Drilling Fluids Conference in Houston, Texas, April 6 – 7.

Brinell. J.A. 1990. Way of Determining the Hardness of Bodies and Some Applications of the Same. *Teknisk Tidskrift*, **5**: 69 – 87.

Chenevert, M.E. 1970. Shale Alteration by Water Adsorption. *J. Petrol. Tech*., 1141 – 1148, Sept.

Winston, P.W., Bates, D.H. 1960. Saturated Solutions for the Control of Humidity in Biological Research. *Ecology*. **41***:* 232 – 237.

Chapter 3: Shale Characterization

Following the procedures described in Chapter 2, the mineralogy and native water activities of seven shales were determined. The four non-hydrocarbon bearing shales were Atoka, C5, Gulf of Mexico (GOM) and Gulf of Mexico 12 (GOM-12). The three hydrocarbon bearing shales were Texas Gas Shale (TGS), Eagle Ford Shale (WGS), and Barnett Shale.

Table 3.1 shows the mineralogy of Atoka, C5 and GOM-12 shales. We can see that all three shales contain more than 30% clay. GOM-12 is the most clay-rich shale among the three, with 65.5% of total clay. Atoka shale is the most quartz-rich shale, with 52% of quartz. The feldspar content of the C5 shale (24%) is ten times that of GOM-12 (2.4%). Table 3.2 shows the mineralogy of TGS, WGS, and the Barnett Shale. We can see that the Barnett shale is quartz-rich (53.1% calcite), while TGS and WGS are calcite-rich (57.9% and 56% respectively). While non-hydrocarbon bearing shales contain more clay and less quartz than hydrocarbon bearing shales, Atoka and Barnett have very similar mineralogical makeup in terms of quartz and clay content. The quartz content of the Atoka shale is 52% while that of the Barnett shale is 53.1%. The total clay content of Atoka shale is 35% while that of the Barnett shale is 33%. Figure 3.1 shows the ternary diagram of the relative abundance of quartz, calcite and clay in these shales.

Table 3.1: Mineralogy of Atoka, C5 and GOM-12 shales

	Wt%		
	Atoka	C5	GOM-12
Quartz	52	32	26.4
Feldspar	15	24	2.4
Total Clay	33	44	65.5
Kaolinite	32	50	21.8
Chlorite	7	1	6.6
Illite	31	13	16.8*
Smectite	19	7	
Mixed Layer	11	29	20.3**

*Illite & mica
**Mixed layer illite/smectie with 40% - 50% smectite

Table 3.2: Mineralogy of TGS, WGS and Barnett shale

	Wt%		
	TGS	WGS	Barnett
Quartz	15.1	10	53.1
K Feldspar	0	1	0.8
Plagioclase	1.5	4	2.6
Calcite	57.9	56	2.1
Dolomite & Fe-Dolomite	0.7	1	1.3
Pyrite	5.7	2	5.1
Total Clay	19	26	35

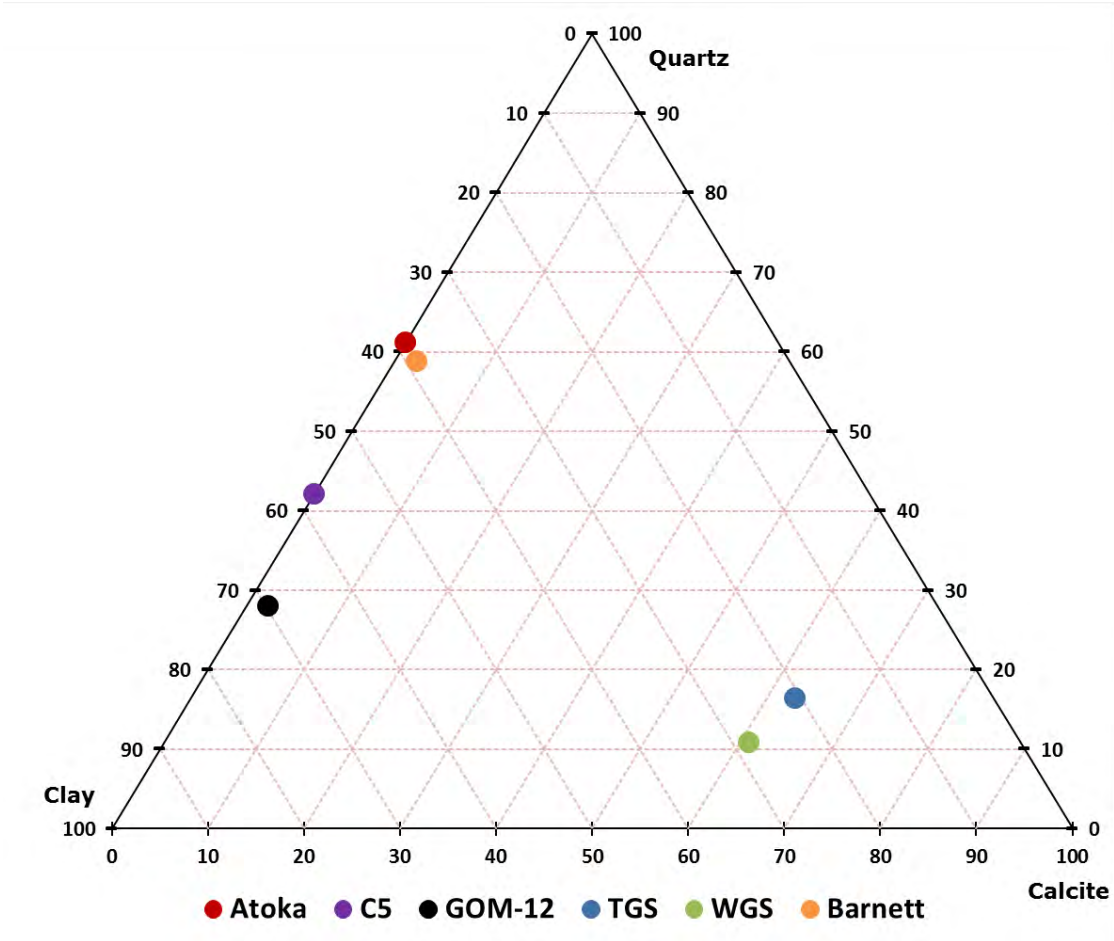

Figure 3.1: Ternary diagram that shows the relative abundance of quartz, calcite and clay

Table 3.3 shows the native water activities of these seven shales. The high values of the native water activity of these shales indicate that the samples were properly preserved in the field after the cores were retrieved from downhole.

Table 3.3: Native water activities of seven shales.

	Native water activity
Atoka	0.72
C5	0.99
GOM	0.96
GOM-12	0.82
TGS	>0.96
WGS	0.75
Barnett	0.92

Figure 3.2 shows the adsorption isotherms used for determining the shales' native water activity. The isotherms of non-hydrocarbon bearing shales were plotted with unfilled circles and that of hydrocarbon bearing shales were plotted with filled circles. The native water activities of C5, GOM and TGS were very close to 1. For TGS, all of the shale samples lost water in controlled humidity desiccators with the highest relative humidity being 96%. Therefore, we can conclude that TGS' native water activity is close to 1.

It is noted that for shales with a native water activity close to one (C5, GOM and TGS), the slope of percent weight change as a function of relative humidity is very small, irrespective of their clay content. It indicates that these shales had very little room for water vapor adsorption, because their native water activity was close to 1. On the other hand, for Atoka, GOM-12, WGS and Barnett, there is a distinct difference in the slope of their percent weight change as a function of relative humidity. It is evident that the slopes of the clay-rich Atoka and GOM-12 shales are much higher than that of the clay-poor WGS and Barnett shale. This can be due to the fact that Atoka and GOM are more water-sensitive than WGS and Barnett shales because of the significantly higher amount of clay present in the non-hydrocarbon bearing shales. One other interesting observation worth mentioning is the slope of the hydrocarbon bearing shales (TGS, WGS and Barnett). These shales underwent very small weight gain regardless of their native water activity. Their slopes of weight change are very similar. This can be caused by the low clay content in these shales, which result in these shales being not very water-sensitive.

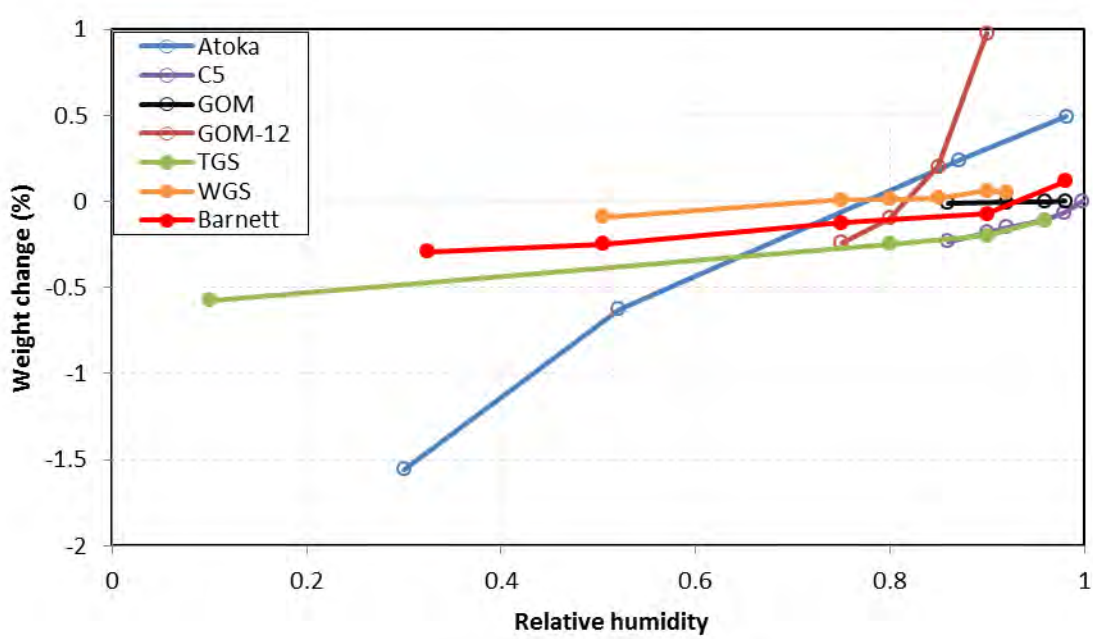

Figure 3.2: Adsorption isotherms for determining the native water activities of shales

Chapter 4: Use of Nanoparticles for Maintaining Shale Stability

Introduction

This experimental study presents the effect of adding nanoparticles to water-based drilling muds and their effect on fluid penetration into hard and soft shale. Use of water-based muds during drilling can cause fluid penetration from the mud into shale formations resulting in swelling and wellbore instability. The nanometer sized pore throat diameters in shales are too small for conventional drilling fluid particles to invade and build a mud cake. Nanoparticles in the shale pore size range were added to lab and field muds to effectively reduce fluid invasion. The sensitivity of nanoparticle dispersions to temperature and salt concentration in the mud was also determined. Four different field muds were studied with and without the addition of nanoparticles using Atoka and Gulf of Mexico shales. Penetration of fluids into the shales was shown to decrease dramatically when nanoparticles were properly sized and applied.

Results show that nanoparticles reduce the permeability of the Atoka shale by a factor of 5 to 50. Similar results are obtained for the GOM shale. Using a nanoparticle dispersion, water penetration into Atoka shale was reduced by 98% as compared to sea water. The membrane efficiency of the shale (a measure of the osmotic pressure contribution) was found to increase by an order of magnitude. Scanning electron micrographs of the Atoka shale taken after exposure to nanoparticle dispersions show that the nanoparticles do indeed penetrate and plug the shale pore throats. These results suggest that nanoparticles could significantly reduce wellbore instability problems in reactive shales.

This plugging of pore throats by the use of nanoparticles is a new approach for controlling fluid invasion into shales, and could have a major impact on solving the chronic problem of wellbore instability.

4.1 Nanoparticle Properties

A particle that has at least one dimension less than 100 nm is referred as a nanoparticle (NP). Nanotechnology refers to measurements in the scale of 1-100 nm. These materials have been applied in optical, electronic and biomedical sciences.

Commercial nanoparticle companies provided us samples of coated silica nanoparticles (CSN) which have 5 and 20 nm diameter with different concentrations. The properties in our nanoparticle inventory are listed in Table 4.1. The effect of the salt concentration on NP stability was investigated with preliminary tests. 10 ml samples from each NP dispersion were taken and mixed with increasing salt concentrations and heated up until precipitation was observed. As seen in Table 4.1, the precipitation temperature is reduced with increasing salt concentration.

Filtration tests were performed using 5-20 nm nanoparticle dispersions. CSN-4 nanoparticles were more compatible with field muds than the 3M NPs and CSN-4 was used for all field mud testing with both Atoka and GOM shales.

Table 4.1: Precipitation temperatures of NP dispersions.

Nanoparticle type	Precipitation Temperatures, F	Salt %wt
3M, 5nm, 17 wt %	180	2.4
3M, 5nm, 17 wt %	160	4
3M, 20 nm, 40 wt %	125	4
CSN-1, 20 nm, 30 wt %	160	0.9
CSN-2, 20 nm, 30 wt %	145	4
CSN-3, 5 nm, 15 wt %	160	4
CSN-4, 20 nm, 40 wt %	170	4

4.2 Preliminary Plugging and Swelling Tests

A preliminary study was performed to see if a 1.3 nano-darcy mud cake could be plugged with nanoparticles. Using past filtration data [5] as a guide this cake was made using a mud that contained 10 ppb bentonite and 1 ppb carboxy-methyl cellulose (CMC). Again, the NP dispersion easily passed through the mud cake.

While waiting for shale equilibrium, a third study was performed using two 1 inch by ½ inch by ½ inch pieces of C5 shale and a swell meter. In these tests, one sample was immersed in water and second sample was immersed in a 41 wt % dispersion of 20 nm particles. As shown in Figure 4.1, after about 1080 minutes, the C5 shale that was immersed in the water had experienced about 10.8 % swelling and the NP dispersion experienced only 6.4 % swelling. In other words, swelling was reduced by 41 % by using the NP dispersion.

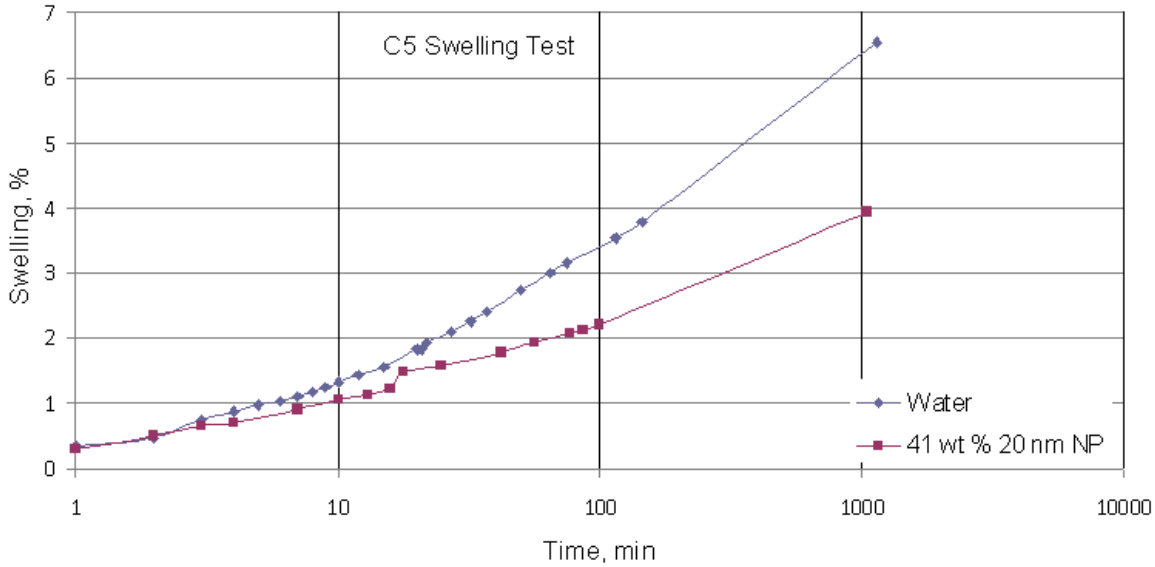

Figure 4.1: C5 Shale swelling test performed with fresh water and NP dispersion.

4.3 Multi-step Tests

In Test 4.1, (Figure 4.2), a three-step procedure was followed. Using the flow equipment described in Appendix A, first, low salinity brine (sea water) was flowed across the shale sample (step 4.1.a) and it easily penetrated the shale completely in about 25 hours. The test was continued by reducing the bottom pressure of the shale and again the sea water easily penetrated

the shale (see 25 to 34 hours of Figure 4.2). Then in the third step (4.1.c) the NP dispersion flowed across the same shale sample and complete shale plugging occurred in only 5 hours (see 34 to 39 hours). Again we see that the NP dispersion can reduce flow into the shale. As shown in Figure 4.2, 3M's 20 nm 41 wt % silica NP dispersion reduced the fluid penetration by 95 % in 6 hours compared to the brine. The test configuration is shown in Table 4.2.

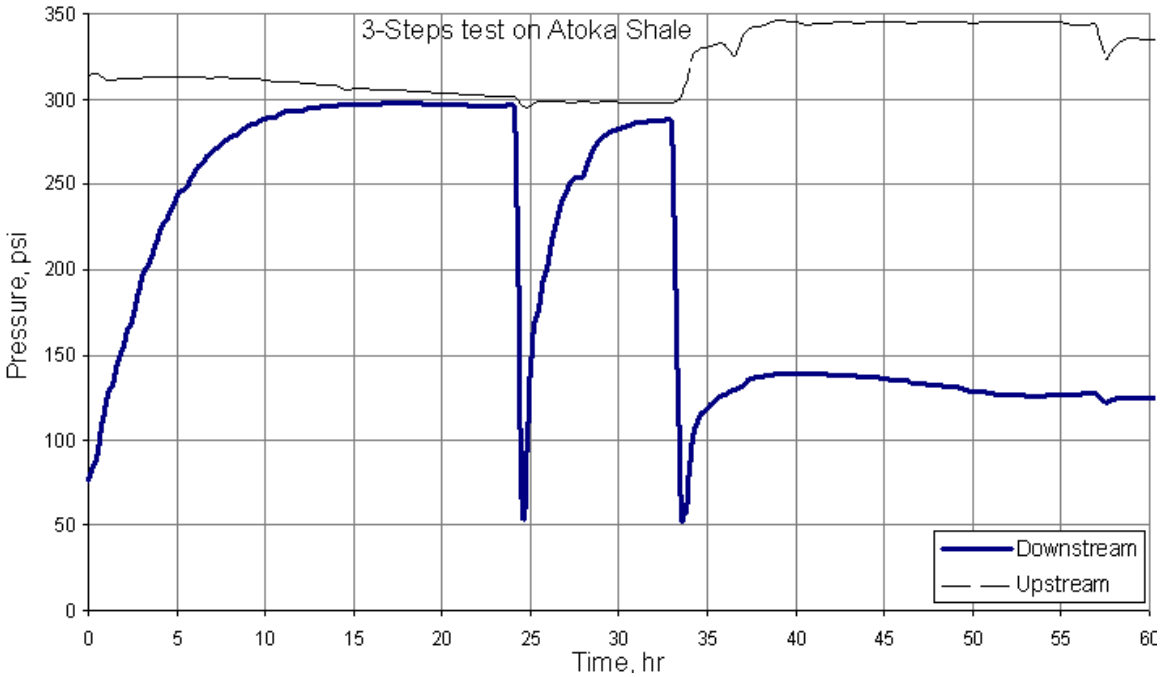

Figure 4.2: Three steps test in contact with Atoka shale

Table 4.2: 3M two steps test in contact with Atoka shale

Test	4.1.a	4.1.b	4.1.c
Date	4/3-5/2008	4/3-5/2008	4/3-5/2008
Shale	Atoka	Atoka	Atoka
Brand	3M	3M	3M
Top Fluid	Brine	Brine	NP
NP wt%	0	0	41
NP Size (nm)	-	-	20
Bottom Fluid	Brine	Brine	Brine
Aw top	0.98	0.98	0.98
Aw Bottom	0.98	0.98	0.98
Aw shale	0.98	0.98	0.98
Top Pres. (Psi)	325	325	350
Bottom Pres. (Psi)	75	50	50

Test 4.2 was performed by following a two-step procedure to see if a high concentration of NP would completely plug the pore throats. In the first step, (4.2.a), (0-28 hours), 3M's 20 nm particle dispersion was used, and the plugging occurred in two hours. In the second step (4.2.b), (28-55 hours), brine was used without NP and the bottom pressure built up to 250 psi differential pressure after 25 hours, which means that there was a very little penetration through the shale. As

shown in Figures 4.2 and 4.3, 3M's 20 nm 41 wt % silica NP dispersion reduced the fluid penetration by 98 % in 6 hours compared to brine. This result shows that the NP dispersion had permanently plugged the shale. The test configuration is shown in Table 4.3.

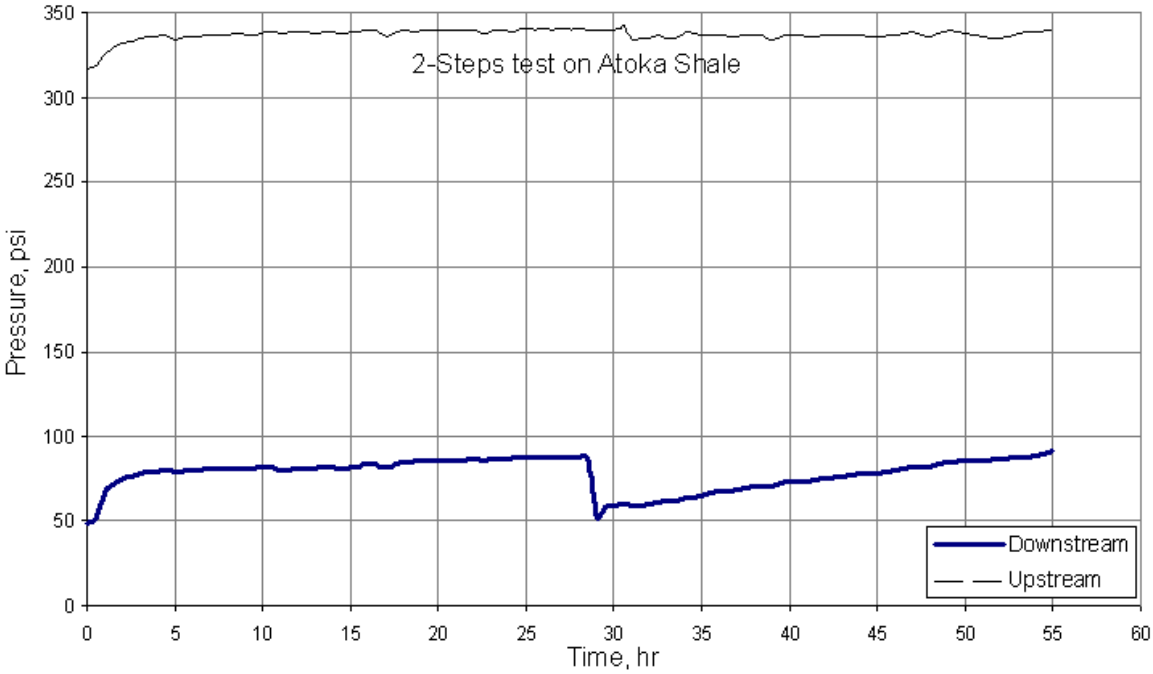

Figure 4.3: Two step test with and without NP

Table 4.3: 3M 20 nm two step test in contact with Atoka shale

Test	4.2.a	4.2.b
Date	4/6-9/2008	4/6-9/2008
Shale	Atoka	Atoka
Brand	3M	3M
Top Fluid	NP	Brine
NP wt%	41	0
NP Size (nm)	20	-
Bottom Fluid	Brine	Brine
Aw top	0.98	0.98
Aw Bottom	0.98	0.98
Aw shale	0.98	0.98
Top Pres. (Psi)	340	340
Bottom Pres. (Psi)	50	50

Test 4.3 was performed to see how a NP dispersion works in another type of shale, the C5. The test consisted of three-steps as shown in Figure 4.4. In the first step (4.3.a), (0-6 hours), negative osmotic pressure was applied to the sample with a lower water activity brine (aw= 0.85). The bottom pressure built up to the top pressure in 6 hours. The second step (4.3.b), (6-10 hours) was performed with a brine solution which had a 0,98 Aw, the same Aw as the sample and the bottom fluid. The bottom pressure built up to the top pressure in 3 hours. In the third step (4.3.c), a 20 nm 41w% NP dispersion was used as a top fluid and pressure built up to a

differential pressure of 150 psi after 7 hours. As shown in Figure 4.4, 3M's 20 nm 41 wt % silica NP dispersion reduced the fluid penetration by 96 % in 6 hours compared to brine. The test configuration is shown in Table 4.4.

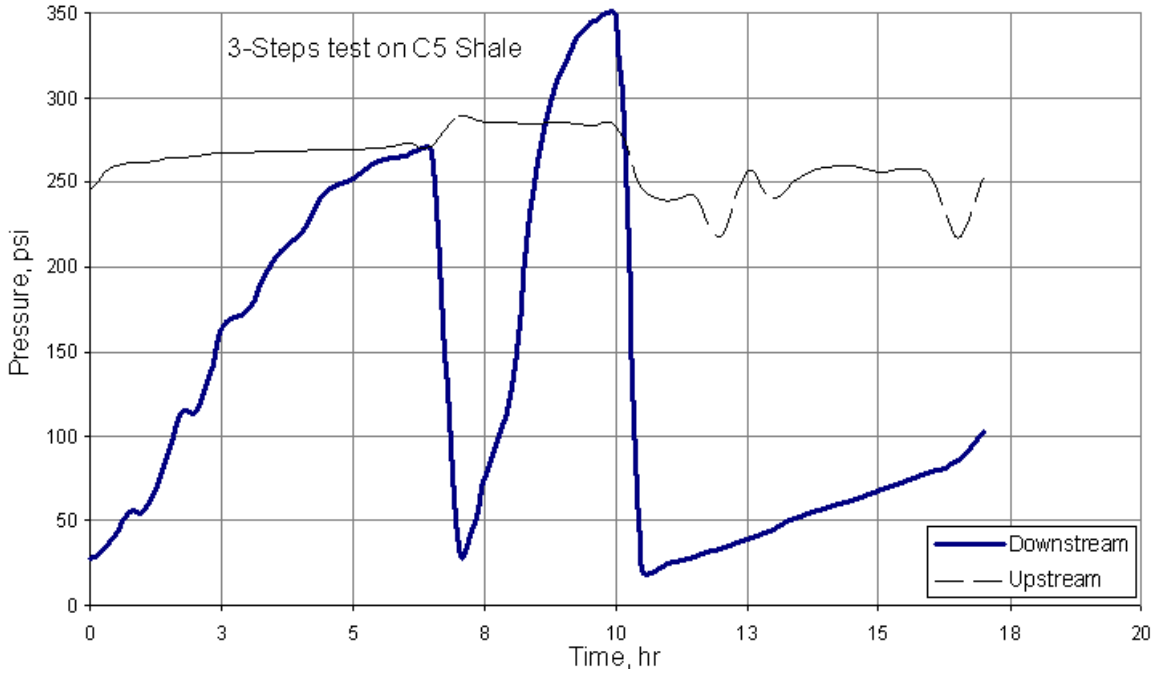

Figure 4.4: Three step test with C5 shale without and with NP

Table 4.4: 3M 20 nm three step test on C5 shale

Test	4.3.a	4.3.b	4.3.c
Date	4/17/2008	4/17/2008	4/17/2008
Shale	C5	C5	C5
Brand	-	-	3M
Top Fluid	Brine	Brine	NP
NP wt%	0	0	41
NP Size (nm)	-	-	20
Bottom Fluid	Brine	Brine	Brine
Aw top	0.98	0.98	0.98
Aw Bottom	0.85	0.98	0.98
Aw shale	0.98	0.98	0.98
Top Pres. (Psi)	250	250	250
Bottom Pres. (Psi)	40	40	40

4.4 Nanoparticle Concentration Tests

Test 4.4 was performed to investigate if a reduced weight percentage (29 wt %) of NP dispersion would work as well as 41 wt %. As seen in Figure 4.5, the bottom pressure did not build up at all. Complete plugging was achieved. The test configuration is shown in Table 4.5.

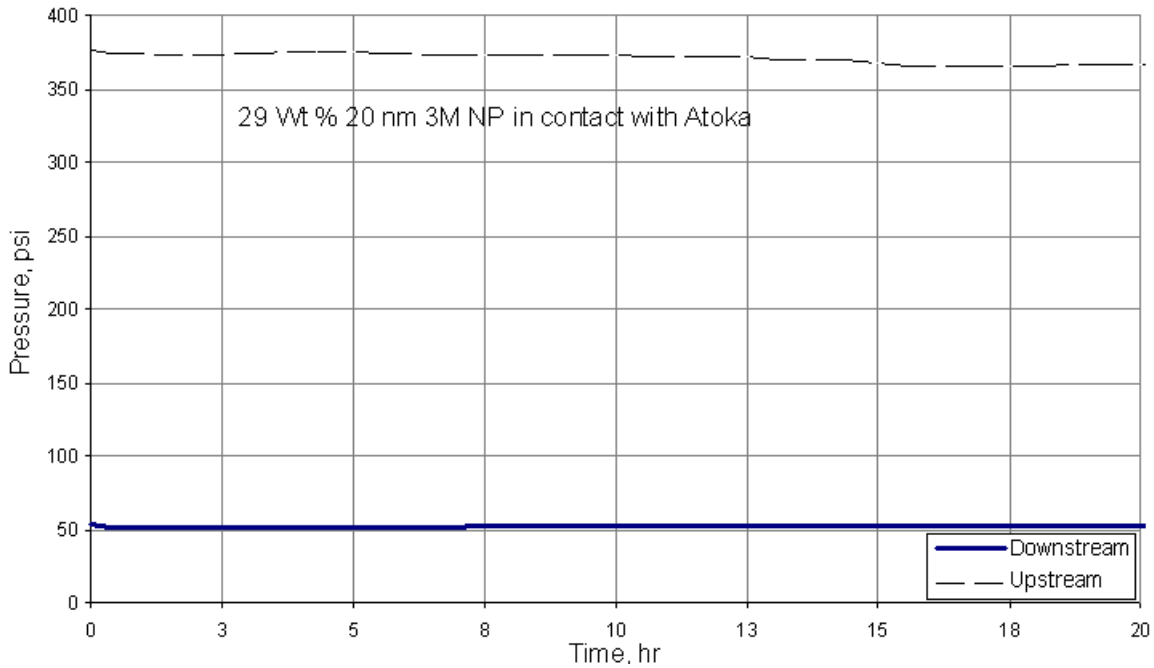

Figure 4.5: Results of the Atoka/ 29 wt % NP dispersion test.

Table 4.5: 3M 20 nm 29 wt % test in contact with Atoka shale

Test	4.4
Date	5/2-3/2008
Shale	Atoka
Brand	3M
Top Fluid	NP
NP wt%	29
NP Size (nm)	20
Bottom Fluid	Brine
Aw top	0.98
Aw Bottom	0.98
Aw shale	0.98
Top Pres. (Psi)	350
Bottom Pres. (Psi)	50

Test 4.5 was performed under the same conditions as the seventh test, except for the NP dispersion weight percentage. The test was performed with 5 wt % NP dispersion and resulted in a bottom pressure buildup of 100 psi differential in 35 hours. As shown in Figure 4.6, 3M 5 wt% NP dispersion concentration is not as effective as 10 wt %. It can be concluded that a 10 wt % is the minimum concentration for penetration reduction. The test configuration is shown in Table 4.6.

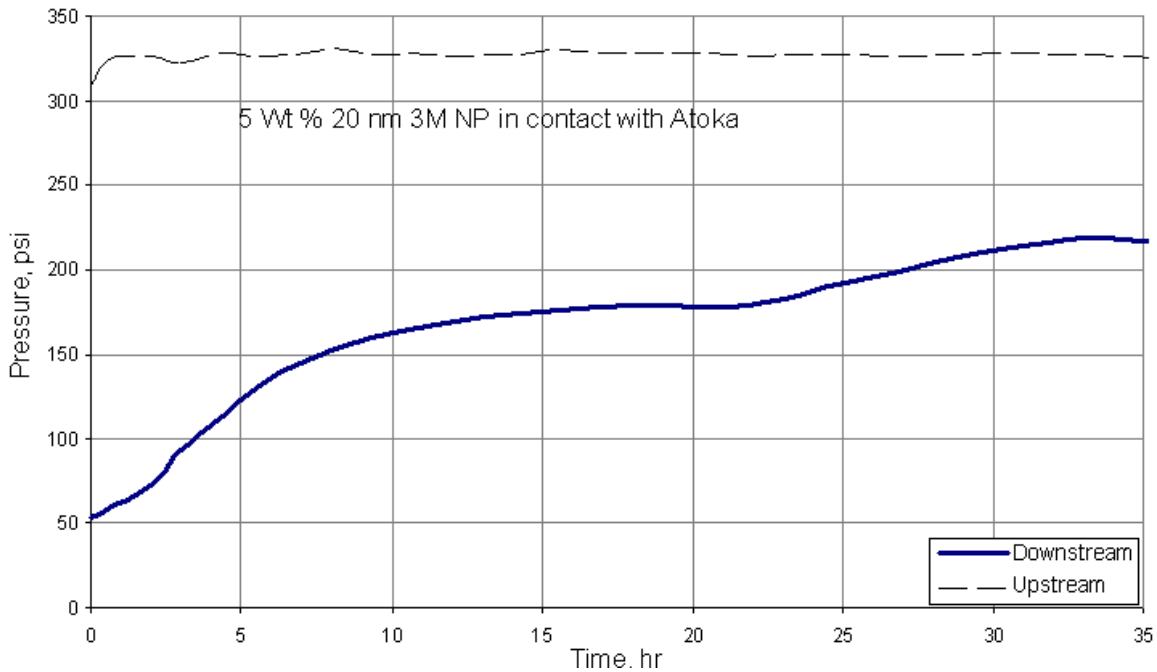

Figure 4.6: Results of the Atoka/ 5 wt % NP dispersion test.

Table 4.6: 3M 20 nm 5 wt % test in contact with Atoka shale

Test	4.5
Date	5/13-14/2008
Shale	Atoka
Brand	3M
Top Fluid	NP
NP wt%	5
NP Size (nm)	20
Bottom Fluid	Brine
Aw top	0.98
Aw Bottom	0.98
Aw shale	0.98
Top Pres. (Psi)	325
Bottom Pres. (Psi)	50

Test 4.6 was performed under the same conditions as the eighth test except for the NP dispersion weight percentage. The test was performed with 10 wt % NP dispersion and the bottom pressure stabilized at a 250 psi differential pressure in 8 hours as shown in Figure 4.7. The test configuration is shown in Table 4.7.

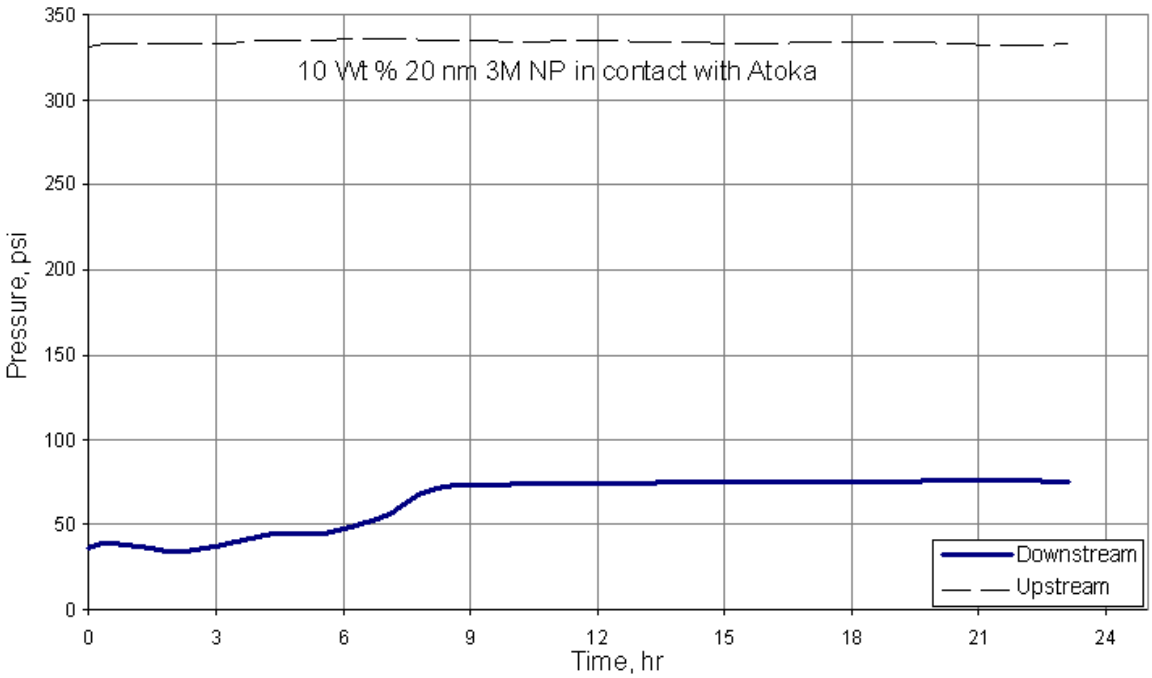

Figure 4.7: Results of the Atoka/ 10 wt % NP dispersion test.

Table 4.7: 3M 20 nm 10 wt % test in contact with Atoka shale

Test	4.6
Shale	Atoka
Brand	3M
Top Fluid	NP
NP wt%	10
NP Size (nm)	20
Bottom Fluid	Brine
Aw top	0.98
Aw Bottom	0.98
Aw shale	0.98
Top Pres. (Psi)	325
Bottom Pres. (Psi)	40

As shown in Figure 4.8, silica nanoparticles reduce the fluid invasion into the shale compared to the brine. Another conclusion is that the minimum concentration required to reduce the fluid penetration is 10 wt % NP.

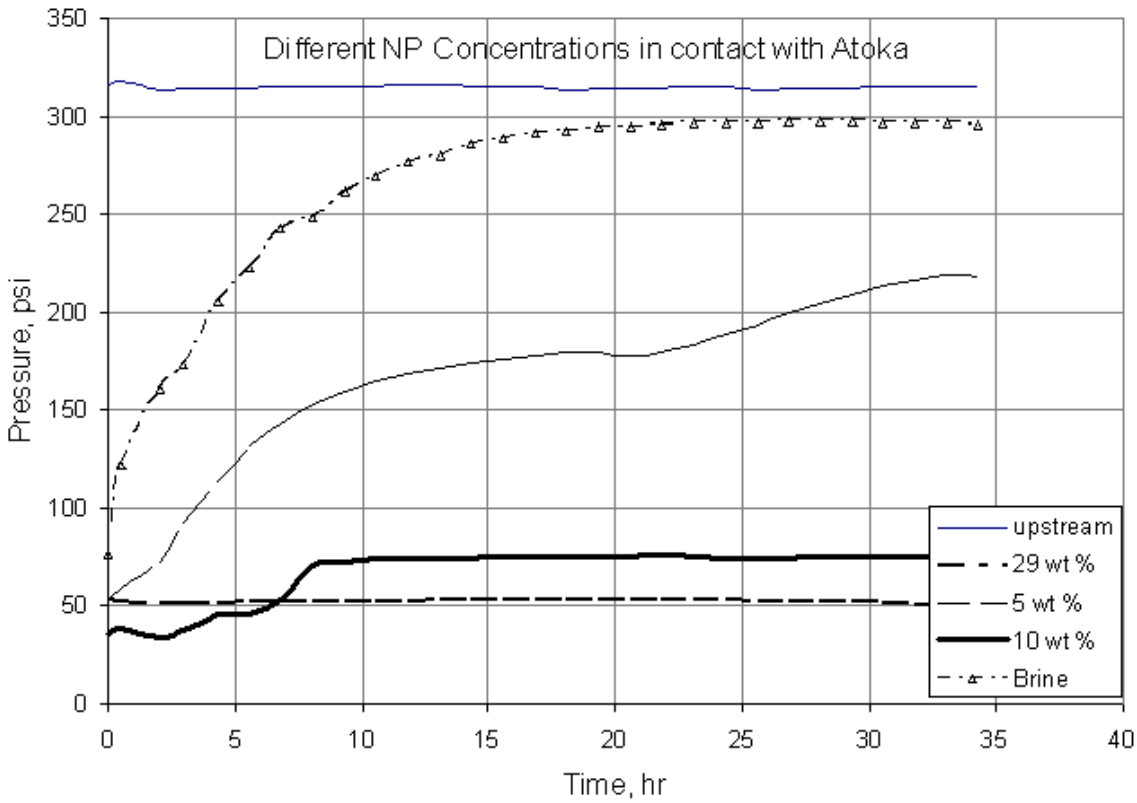

Figure 4.8: NP tests with different concentrations in contact with Atoka shale.

4.5 Scanning Electron Micrographs

The next study consisted of using Scanning Electron Micrographs to visualize the type of plugging that was taking place. Figures 4.9 to 5.11 were obtained using an Atoka shale sample that had been tested with 3M's 20 nm 29 w% silica NP dispersion.

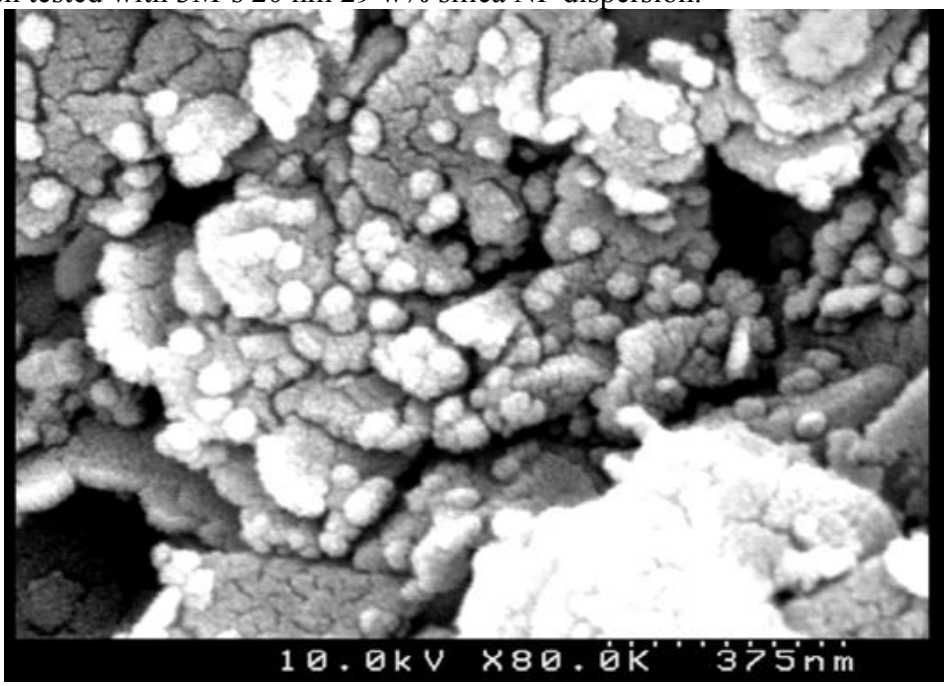

Figure 4.9: SEM of 20 nm particles in contact with Atoka shale. (Dotted scale is 375 nm)

In Figures 4.9 and 4.10, it is seen that Atoka shale has a wide range of pore throats and 20 nm particles could plug just the ones that fit that size. This result suggests that if a NP mixture which consists of different sized particles between 5-50 nm, more pores could be plugged. It is easily seen in the lower-center of Figure 4.11 that the group of 20 nm nanoparticles can plug one big sized pore throat.

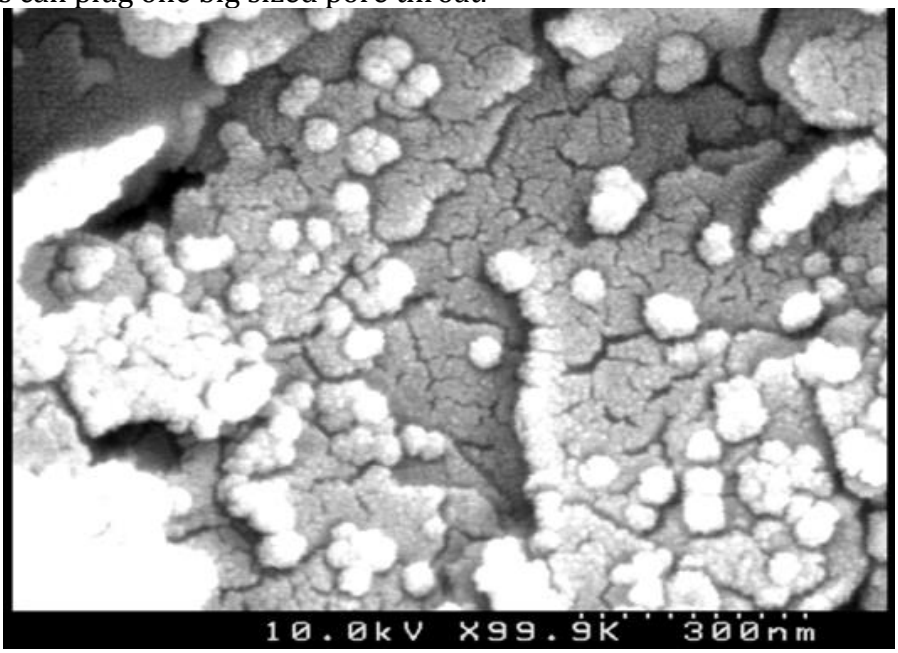

Figure 4.10: 20 nm silica NP in different scale

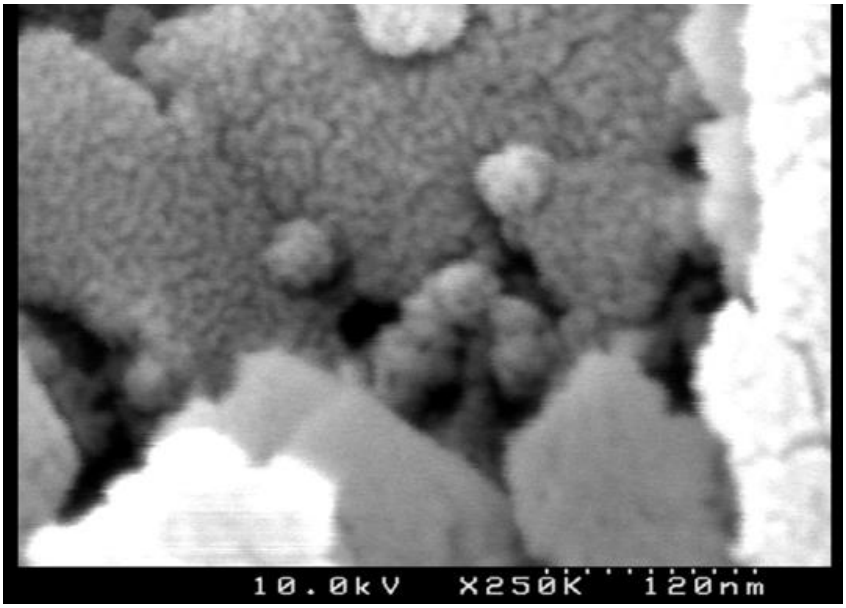

Figure 4.11: Group of particles plugged a pore throat

4.6 Nanoparticle Type and Size Tests

Test 4.7 was performed to investigate the effect of the CSN-4 in contact with Atoka shale. This test is the first straight application of CSN-4 dispersion. In this test a sample of Atoka shale was exposed to a 40 wt %, 20 nm NP dispersion. Table 4.7 shows the test condition. As seen in Figure 4.12, the bottom pressure built up in 17 hours at about 12 psi /hour, which is considered high. CSN-4 did not plug the pores as well as 3M's 20nm NP did in tests 4.2, 4.3, 4.4 and 4.6.

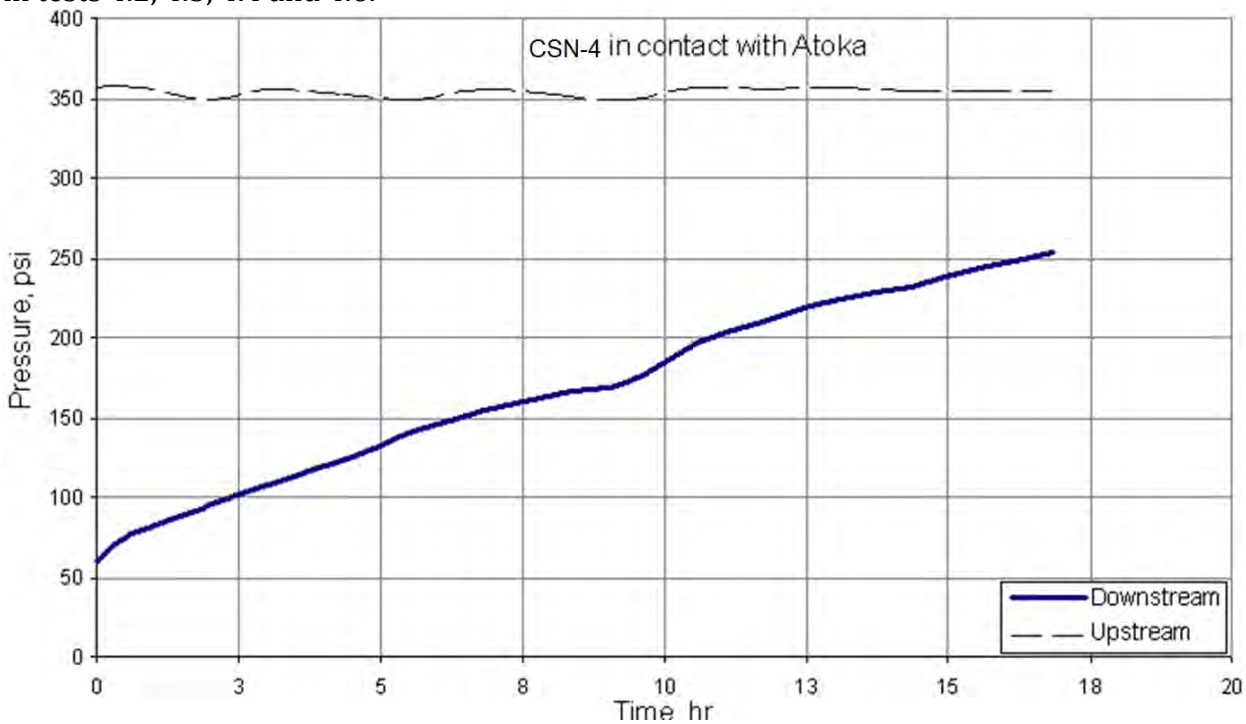

Figure 4.12. Results of the Test 4.8 which was performed with CSN-4 40 wt % 20 nm dispersion.

Table 4.8: Conditions in Test 5.7.

Test	5.7
Date	9/13/2008
Shale	Atoka
Top Fluid	NP
NP wt%	41
NP Size (nm)	20
Bottom Fluid	Brine
Aw top	1
Aw Bottom	0.98
Aw shale	0.98

Test 4.8 and 4.9 were performed to investigate the effect of 5nm NPs in contact with Atoka shale. These tests are the first trials of 5nm particles. 3M's 17 wt % NP and CSN-3 dispersions flowed across the surface of the Atoka shale sample. Test conditions are shown in

Table 4.8. As seen in Figure 4.13, the bottom pressure built up to top pressure in 25 hours. 5nm particles did not plug the pores as much as 20 nm particles did.

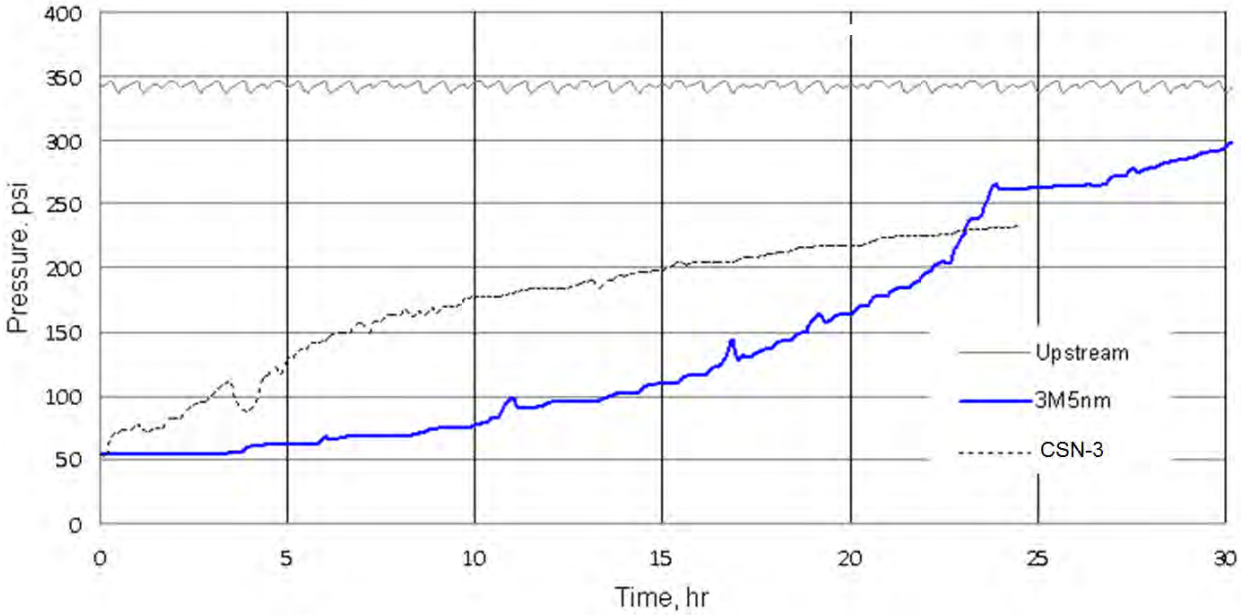

Figure 4.13. 3M's 17 wt % and CSN-3 dispersions in contact with Atoka.

Table 4.9: Conditions in Test 4.8 and 4.9.

Test	4.8	4.9
Date	9/19/2008	9/20/2008
Shale	Atoka	Atoka
Brand	N/A	3M
Top Fluid	NP	NP
NP wt%	15	17.71
NP Size (nm)	5	5
Bottom Fluid	Brine	Brine
Aw top	0.98	0.98
Aw Bottom	0.98	0.98
Aw shale	0.98	0.98
Top Pres. (Psi)	340	340
Bottom Pres. (Psi)	55	55

Chapter 5: Decreasing Water Invasion into Atoka Shale Using Silica Nanoparticles

Abstract

Fluid penetration from water-based muds into shale formations results in swelling and wellbore instability. It was found in a later study (Sensoy, Chenevert and Sharma, 2009) that specially coated silica nanoparticles (NPs), were able to not only tolerate various types of muds but also reduce the shale's permeability by up to 98%. This reduction of fluid into shale was thought to be the result of plugging of the shale's pore throats by the NPs.

Such coated NPs can be excessively expensive and this limits their usefulness. It was therefore decided to search for lower cost, non-treated NP that can produce high levels of permeability reduction in shale. This study presents laboratory data showing the positive impact of adding commercially available, inexpensive, non-modified silica nanoparticles to water-based drilling muds and their effect on water invasion into shale.

Six of the original seven brands of commercial and non-modified nanoparticles (NP) were tested and screened by running a three-step pressure penetration test (brine - base mud - NP mud). Two types of common water-based muds (a bentonite mud and a low solids mud, or LSM) in contact with Atoka shale were studied with and without the addition of 10 wt% nanoparticles. We found that a large reduction in shale permeability was observed when using the muds to which the non-modified NPs had been added. For the bentonite muds, the permeability of Atoka shale decreased by 57.72% to 99.33% and for the low solid muds, the permeability of Atoka shale decreased by 45.67% to 87.63%. Higher plastic viscosity (PV), lower yield point (YP) and fluid loss (FL) of the NP muds compared with base muds were also observed by the addition of NPs. We also found that nanoparticles varying in size from 7 nm to 15 nm and a concentration of 10 wt% are shown to be effective at reducing shale permeability thereby reducing the interaction between Atoka shale and a water-based drilling fluid.

This study shows for the first time that it is possible to formulate water based muds using inexpensive non-modified and commercially available silica nanoparticles and that these muds significantly reduce the invasion of water into the shale. The addition of silica nanoparticles to water based muds may offer a powerful and economical solution when dealing with wellbore stability problems in troublesome shale formations.

5.1. Introduction

Shales account for 75% of the all footage drilled (Steiger, 1992) and are responsible for 90% of wellbore stability problems. Maintaining wellbore stability is one of the most critical aspects of oil and gas drilling. The main cause of shale instability for both soft and hard shales is water absorption and subsequent swelling and sloughing of the wellbore (Chenevert, 1970). The wellbore pressure penetrates into the shale pore space when water invades the shale. This reduction of true overbalance, which acts like a support pressure for the hole, can result in shale failure and wellbore instability (Ewy and Morton, 2009).

Even though a good bit of research has focused on improving wellbore stability with specially engineered water-based muds, no such inhibitive mud currently exists (Sensoy and

Chenevert, 2009). Al-Bazali et al (2005b) found that the average pore throat sizes of a variety of shales range from 10 to 30 nanometers (0.01 to 0.03 microns). Compared with shale pore throat sizes, commonly used drilling fluid additives such as bentonite and barite, have much larger particle diameters, in the range of 100 nm to 10,000 nm. Figure 5.1 presents a scale showing this particle size range. The extremely low permeability and small pore throat size observed in shales is such that conventional filtration additives do not form mud cakes and thus do not stop fluid invasion.

Only nano-size particles have the possibility of plugging pore throats in shales. Nanotechnology represents the development and application of materials, methods, and devices in which the critical length scale is on the order of 1nm to 100 nm. The technology is an enabler that may prove to be a game changer for exploiting fossil-based fuels and, over the next 30 years, and will certainly be a critical component in developing fossil-based energy technologies (Krishnamoorti, 2006). To the best of our knowledge, the use of nanoparticles in drilling fluids is the first potential large scale application of nanoparticles in the oil and gas industry. Other applications of nanoparticles as tracers for reservoir engineering and formation evaluation applications have been suggested (Pourafshary, 2009; Amanullah, 2009).

In our lab, Sensoy, Chenevert and Sharma (2009) showed that at least 10 wt% of nanoparticles is necessary to achieve significant plugging of shale pore throats to reduce the permeability and minimize fluid invasion into shales. They also reported the results of four field muds in contact with Atoka and Gulf of Mexico (GOM) shales with and without the addition of two kinds of experimental "modified" NPs.

Modified NPs (those NPs coated with specific chemicals or charged functional groups) are much more expensive than non-modified NPs and may prove to be prohibitively expensive. We, therefore, decided to investigate the possibility of using non-modified NPs for reducing the permeability of shales. Based on the results of prior research, we decided to investigate adding various commercial and non-treated silica nanoparticles which sizes varying from 5 nm to 22 nm to the drilling fluids to see whether it was possible to reduce the permeability of shales by a significant amount.

5.2. Experimental methods

5.2.1 Materials used

5.2.1.1 Nanoparticles

A total of 22 different types of NPs were obtained from four manufacturers. Of these samples, only 7 were non-modified, non-acidic, and commercially available, as shown in Table 5.1. This paper focuses on these 7 NP products.. Their performance was first evaluated using a thermal stability test and then a Pressure Penetration (PP) test. All PP tests contained in this chapter were performed using preserved Atoka shale.

Table 5.1: Inventory of selected silica nanoparticle dispersions

No.	Label	NP, wt %	NP size, nm	SG, g/cc	pH
1	G	15.5	5	1.103	10.2
2	D	39.7	12	1.299	9.6
3	A	30.2	7	1.22	10
4	E	50	22	1.242	9
5	B	30.4	10~15	1.2	10
6	C	30.7	7~9	1.2	10
7	F	40.8	10~20	1.307	10.1

5.2.1.2 Shale properties

Shale is a sedimentary rock that consists of clays, quartz, and other silicate and carbonate minerals. Because of their high clay content, shale tends to absorb water from a water-based mud, which results in swelling and sloughing of the wellbore. In this study, a hard, preserved Atoka shale was used. Its handling, and properties are presented in Chapter 2.

The mineralogical composition of this shale as listed in Table 5.2, contains 33% clay which mainly included kaolinite (32%), chlorite (7%), illite (31%), smectite (19%) and mixed layer (11%) clays.

Table 5.2: Composition of Atoka shale

X-Ray Diffraction	wt%
Quartz	52
Feldspar	15
Total clay	33

5.2.1.3 Muds used

Three types of water-based muds were used in this study, a fresh water mud (FWM), a thick bentonite mud and a low solids mud (LSM). It was found that in all tests the presence of 10 wt% NPs reduced the permeability of the shale. The following tables (Tables 5.**3** to 5.**5)** show the formulation and properties of the muds tested.

a) Fresh Water Mud

Table 5.3: Formulation and properties of fresh water mud

Water, g	Bentonite, g	Rev Dust, g	Lignosulfonate, g	Lignite, g	PV	YP	API-FL	pH
350	22.5	10	3	3	12	2.5	9.2	10.5

b) Thick bentonite mud

Table 5.4: Formulation and properties of thick bentonite mud

Water, g	Bentonite, g	PV	YP	API-FL	pH
350	30	41	50	8.6	7

c) Low Solids Mud

Table 5.5: Formulation and properties of low solid mud (LSM)

Water, g	FLO-TROL, g	Rev Dust, g	Duo-Vis g	PV	YP	API-FL	pH
350	3	4.62	2	8	28.5	13.2	10

5.2.2 Test equipment for measuring shale permeability

The pressure penetration (PP) test equipment used to measure the shale's permeability is presented in Chapter 2.

5.2.3 Experimental procedures

5.2.3.1 Thermal stability test

The thermal stability test consisted of adding 10 wt% NPs to a water-base mud (fresh water mud) then heating it to 176 ºF for 16 hours. The mud-NP mixtures that had unacceptable properties were rejected and the remaining mud-NP mixtures were then subjected to the PP test.

5.2.3.2 Pressure penetration tests (PPTs)

The three step testing procedure was used because it was found that the shale test samples did not have the same original permeability. It was decided to first flow sea water through the shale sample until equilibrium was reached so as to produce saturated shale samples that have the same starting conditions.

For the second step, a PP test was run using the base mud to obtain a "base mud" permeability for that sample. Finally a PP test was run using the base mud that contained 10 wt% NPs. The percent permeability reduction was obtained by dividing the permeability difference achieved during step 3 by that of step 2 (times 100).

For the tests performed with the LSM, a similar procedure was followed.

5.3. Results and Discussion

5.3.1 Thermal stability tests on fresh water mud containing NPs

The seven non-modified and commercial NP dispersions (as shown in **Table 1**) were mixed with FWM so as to obtain a 10 wt% mixture. They were then heated at 176ºF for 24 hrs,

then aged at room temperature for another 24 hours. The rheology and filtration results are listed in Table 5.6.

Table 5.6: Properties of FWM w/wo NPs after 24 hours @ 176°F and 24 hours aging.

No.	Label	PV	YP	API-FL	pH
0	FWM	28.5	8.0	8.4	8.5
1	FWM + NP-G	5.5	2.0	flowing	9
2	FWM + NP-D	26.5	8.0	6.1	9
3	FWM + NP-A	41.5	14.0	6	9.5
4	FWM + NP-E	33.0	14.0	6.4	8
5	FWM + NP-B	18.0	4.5	7.3	8.5
6	FWM + NP-C	20.5	2.5	5.8	8.5
7	FWM + NP-F	29	7.5	5.7	9

From Table 5.6, we can see that all muds were acceptable except for NP-G. This mud had very poor rheology and unlimited filtration. For this reason PP tests were not performed using NP-G.

5.3.2 Rheology of NP containing muds

The rheology properties of NP containing muds are listed in Table 7 and Table 8. We can see that the presence of NPs resulted in higher PV, lower YP and API filtration. The addition of NPs results in a higher solids content and this results in a higher PV. On the other hand, the addition of extra water in the NP dispersion diluted the mud and decreased the YP.

5.3.3 Filtration of NP containing muds

The API filtration properties of NP containing muds are listed in Table 5.7 and Table 5. 8**.** Nano-sized silica could plug the throats of the filter paper and formed a thin and hard mud cake which led to a decline in the API filtration.

Table 5.7: Rheological and filtration performances of bentonite muds w/wo nanoparticles in pressure penetration (PP) tests

No.	Mud formulation	PV	YP	API-FL	pH
0	Thick bentonite Mud	41	50	8.6	7
1	Thick bentonite mud+extra water	12	12.5	10.8	8.5
	Thick bentonite mud + NP-A	15	8.5	6.2	9
2	Thick bentonite mud+extra water	12.5	11.5	11.8	9
	Thick bentonite mud + NP-B	19	5.5	6.5	9
3	Thick bentonite mud+extra water	12	17.5	11.7	8.5
	Thick bentonite mud + NP-C	13	5.5	6.6	9
4	Thick bentonite mud+extra water	16.5	16	10.5	8.5
	Thick bentonite mud + NP-D	21	12.5	6.1	9
5	Thick bentonite mud+extra water	20	21.5	9.7	8.5
	Thick bentonite mud + NP-E	25	17.5	6.5	7
6	Thick bentonite mud+extra water	16.5	16	10.2	8.5
	Thick bentonite mud + NP-F	20.5	8.5	5.9	9

Table 5.8: Rheological and filtration performances of LSM w/wo nanoparticles in PP tests.

No.	Mud formulation	PV	YP	API-FL	pH
1	Thick LSM + extra water	7.5	18.5	14.7	10
	Thick LSM + NP-A	9	17.5	10.8	10
2	Thick LSM + extra water	6	18.5	15.7	10
	Thick LSM + NP-B	9	17.5	11.2	10
3	Thick LSM + extra water	9.5	15.5	16.8	11
	Thick LSM + NP-C	9	18.5	11.6	10
4	Thick LSM + extra water	8	21	14.9	10
	Thick LSM + NP-D	8.5	20.5	11.0	9.5
5	Thick LSM + extra water	9.5	26	13.5	11
	Thick LSM + NP-E	9	17	11.2	10
6	Thick LSM + extra water	11	26.5	15.2	10
	Thick LSM + NP-F	11	26.0	11.0	10

5.3.4 Changes in shale permeability with the addition of NPs

The results obtained for the 6 selected NP dispersions for the thick bentonite mud and the LSM are presented in Table 5.9.

As seen in Table 5.9, all 6 non-modified NP dispersions were able to significantly reduce the permeability of Atoka shales, as compared to the two mud types studied. Selected individual data sets obtained for these tests are plotted in Figure 5.2 to Figure 5.5. Histograms of the permeability reduction are shown in Figure5.6 and Figure 5.7.

Table 5.9: Permeability changes of Atoka shales w/wo nanoparticles in PP tests

Base mud	Shale's No.	NP Brand	NP size, nm	NP wt% in dispersion, %	NP wt% in muds, %	Permeability, nD			Δk, %
						brine	base mud	NP mud	
Bentonite mud	Atoka 21B	NP-A	7	30.2	10	0.18	0.015	0.0001	99.33
	Atoka 18B	NP-B	10~15	30.4		0.476	0.050	0.003	94.00
	Atoka 16B	NP-C	7~9	30.7		0.08	0.022	0.0006	97.27
	Atoka 14B	NP-D	12	39.7		0.99	0.15	0.0058	96.13
	Atoka 37C	NP-E	22	50		39.94	2.72	1.15	57.72
	Atoka 36C	NP-F	10~20	40.8		63.67	6.25	0.97	84.48
Low solid mud/LSM	Atoka 34C	NP-A	7	30.2	10	0.17	0.0258	0.0034	86.92
	Atoka 33C	NP-B	10~15	30.4		0.174	0.01	0.0015	85.00
	Atoka 32C	NP-C	7~9	30.7		0.99	0.41	0.11	73.17
	Atoka 46D	NP-D	12	39.7		0.65	0.034	0.0085	75.00
	Atoka 30C	NP-E	22	50		1.26	0.108	0.0587	45.67
	Atoka 29C	NP-F	10~20	40.8		0.125	0.0097	0.0012	87.63

5.3.5 Effect of mud composition on shale permeability

5.3.5.1 Effect of NP size

The average pore throat sizes of a variety of shales range from 10 to 30 nm. Figure 5.8 shows the plot of NP size vs. permeability reduction percent (Δk). It was found that NPs with size varying from 7 nm to 15 nm had better plugging performance than those with size greater

than 20 nm. We speculate that only nanoparticles whose particle size falls in this range could enter and plug the pore throat of shales and, therefore, minimize fluid invasion into shales. It also must be pointed out that 7 nm to 15 nm NPs work well for Atoka shale while other sizes may be needed for other shale types.

5.3.5.2 Effect of NP concentration in pure NP dispersions

Shale permeability tests were performed at NP concentration levels of 30.2%, 10% and 5% with NP-A for comparative purposes. A summary of these tests is provided in Table 5.10 and Table 5.11. Figure 5.9 presents the plot of NP concentration in pure dispersions vs. permeability reduction percent.

Table 5.10: Summary of PP tests using pure NP-A dispersion.

Shale's No.	NP name	wt% NP	Permeability, nD			Δk, %
			brine	pure NP dispersion	brine	
Atoka 24B	NP-A	30.2	0.77	4.02E-05	1E-04	99.99
Atoka 50E		10.0	0.82	0.0017	-	99.79
Atoka 52E		5.0	0.312	0.159	-	49.04

Table 5.11: Summary of PP tests using pure NP-B dispersion.

Shale's No.	NP name	wt% NP	Permeability, nD			Δk, %
			brine	pure NP dispersion	brine	
Atoka 22B	NP-B	30.4	17.16	0.029	0.009	99.83
Atoka 53E		10.0	0.453	0.0475	-	89.51
Atoka 55E		5.0	13.31	1.37	-	89.71

From Table 5.10 we can conclude that the pure NP dispersions with a concentration greater than or equal to 10 wt% were more effective at shale pore plugging and reducing fluid invasion into shale samples.

5.3.5.3 Effect of NP concentration in muds

For a drilling mud, filtration and rheology properties need to be suitable to fulfill drilling requirements. The tests below were performed to study the effect of NP concentration in muds on permeability reduction percent of shales. Table 5.12 and Figure 5.10 show a summary of results.

Table 5.12: Overview of basic three-step PP tests using various NP concentrations.

Shale's No.	NP name	wt% NP in muds	Permeability, nD			Δk, %
			brine	LSM	LSM+NP	
Atoka 34C	NP-A	10	0.17	0.0258	0.0034	86.92
Atoka 39D		5	5.0	0.216	0.168	22.22
Atoka 33C	NP-B	10	0.174	0.01	0.0015	85.00
Atoka 44D		5	0.22	0.0136	0.007	48.53

It's obvious that the PP tests run with 5% NP produced significantly inferior results than when a 10wt% NP dispersion was used. From this comparative study we can see that 10 wt% is the preferred concentration to be used in muds for acceptable plugging of the Atoka shale.

5.3.6 Potential for Field Application

Water-based inhibitive muds containing non-modified nanoparticles have been formulated for the first time. These non-modified nanoparticles based mud may hold great promise in the future to address shale instability problems.

We have also seen that non-modified pure nanoparticles dispersions with a concentration equal to or over than 10 wt% can be squeezed into unstable shale formations to plug pore throats, stop fluid invasion and increase wellbore stability. This can be especially useful for drilling through a short section of a particularly unstable shale formation.

Furthermore, it may be possible to use non-modified nanoparticles as a component in a fracturing fluid, to minimize fluid invasion into shale formations and enhance return permeability as a whole.

5.4. Conclusions

1. The results presented in this chapter show that it is definitely possible to significantly reduce the invasion of water-based fluids into shales using non-modified NPs.
2. Of the six selected NP dispersions, NP-A, NP-B, NP-C, NP-D and NP-F, performed very well when tested with Atoka shale. The permeability reduction for a preserved Atoka shale was in a range of 73.17% to 99.13% by the addition of 10wt% NPs.
3. For the bentonite muds, the permeability reduction for a preserved Atoka shale was in a range of 57.72% to 99.33% by the addition of 10 wt% NPs.
4. For the low-solids muds, the permeability reduction for a preserved Atoka shale was in a range of 45.67% to 87.63% by the addition of 10 wt% NPs.
5. Nanoparticles varying in size from 7 nm to 15 nm and a concentration of 10 wt% are shown to be effective at reducing shale permeability and thereby reducing the interaction between the shale and a water-based fluid.

Based on the results obtained it is now possible to envision a water-based drilling fluid containing nanoparticles that will have a much smaller interaction with the shale. This lower water invasion will lead to less wellbore instability problems and may lead to the use of water-based fluids that are suitable for drilling long sections of horizontal laterals. Such water-based drilling fluid formulations are now being developed.

5.5 Nomenclature

PV = plastic viscosity, cp;

YP = yield point, lbf/100 sq ft;

API-FL = fluid loss under API standard test conditions, cm^3.

5.6 References

Abrams, A. 1977. Mud Design to Minimize Rock Impairment due to Particle Invasion. *Journal of Petroleum Technology* 29(5): 586-592.

Al-Bazali, T. M. 2005a. Experimental Study of the Membrane Behavior of Shale during Interaction with Water-based and Oil-based Muds. Dissertation presented at the Faculty of the Graduate School of The University of Texas at Austin, Austin, Texas, May.

AL-Bazali, T.M., Zhang, J., Chenevert, M.E., and Sharma, M.M. 2005b. Measurement of the Sealing Capacity of Shale Caprocks, paper SPE 96100 presented at SPE Annual Technical Conference and Exhibition, 2005, Dallas, Texas, October 9-12. DOI: 10.2118/96100-MS.

Amanullah, M., Al-Tahini, A. M. 2009. Nano-Technology – Its Significance in Smart Fluid Development for Oil and Gas Field Application, paper SPE 126102 presented at SPE Saudi Arabia Section Technical Symposium in AlKhobar, Saudi Arabia, May 9 – 11. DOI: 10.2118/126102-MS.

Carminati, S., Gaudio, L.D., Brignoli M. 2000. Shale Stabilization by Pressure Propagation Prevention, paper 63053 presented at SPE Annual Technical Conference and Exhibition in Dallas, Texas, October, 1 – 4. DOI: 10.2118/63053-MS.

Chenevert, M.E. 1970. Shale Control with Balanced-activity Oil-continuous Muds. *Journal of Petroleum Technology*, 22(10): 1309-1316.

Chenevert, M.E., Amanullah, M. 2001. Shale Preservation and Testing Techniques for Borehole-Stability Studies. *SPE Drilling & Completion*, 16(3): 146-149. SPE 73191-PA. DOI: 10.2118/73191-PA.

Ewy, R.T., Morton E. K. 2009. Wellbore-Stability Performance of Water-Based Mud Additives. *SPE Drilling & Completion*, 24(3): 390-397. SPE 116139-PA. DOI: 10.2118/116139-PA.

Hands, N., Kowbel, K., Maikranz, S., and Nouris, R. 1998. Drill-in Fluid Reduces Formation Damage, Increases Production Rates. *Oil and Gas Journal* (July): 13.

Hayatdavoudi, A., Apande, E. 1986. A Theoretical Analysis Of Wellbore Failure And Stability In Shales, paper 86-0571 presented at the 27th U.S. Symposium on Rock Mechanics (USRMS) in Tuscaloosa, AL, June 23 - 25.

Ramanan, K. Extracting the Benefits of Nanotechnology for the Oil Industry. *Journal of Petroleum Technology*, November 2006: 24-26.

Pourafshary, P., Azimipour, S.S., Motamedi, P., Samet, M., Taheri, S.A., Bargozin, H., and Hendi, S.S. 2009. Priority Assessment of Investment in Development of Nanotechnology in Upstream Petroleum Industry, paper SPE 126101 presented at SPE Saudi Arabia Section Technical Symposium in AlKhobar, Saudi Arabia, May 9 – 11. DOI: 10.2118/126101-MS.

Sensoy, T., Chenevert, M.E., and Sharma M. M. 2009. Minimizing Water Invasion in Shales Using Nanoparticles, paper SPE 124429 presented at SPE Annual Technical Conference and Exhibition in New Orleans, Louisiana, October 4 – 7. DOI: 10.2118/124429-MS.

Steiger, R.P. and Leung, P. K. 1992. Quantitative Determination of the Mechanical Properties of Shales. *SPE Drilling Engineering*, 7(3): 181-185. SPE 18024-PA. DOI: 10.2118/18024-PA.

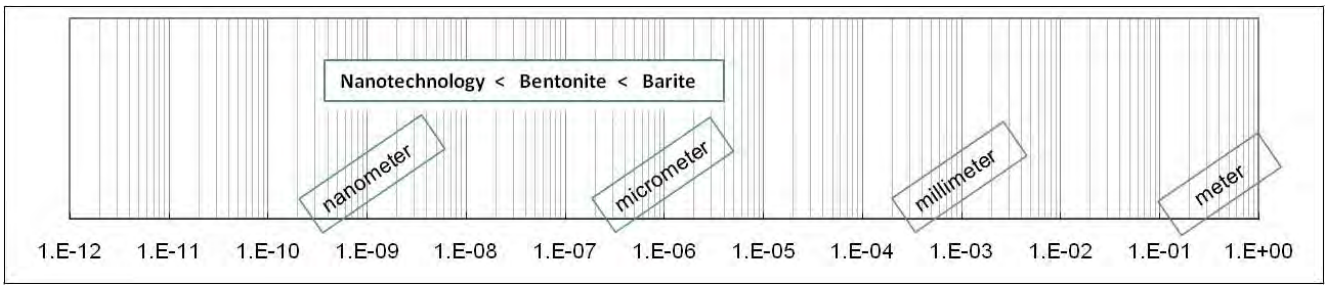

Figure 5.1: Particle size scale, adapted from Abrams (1970)

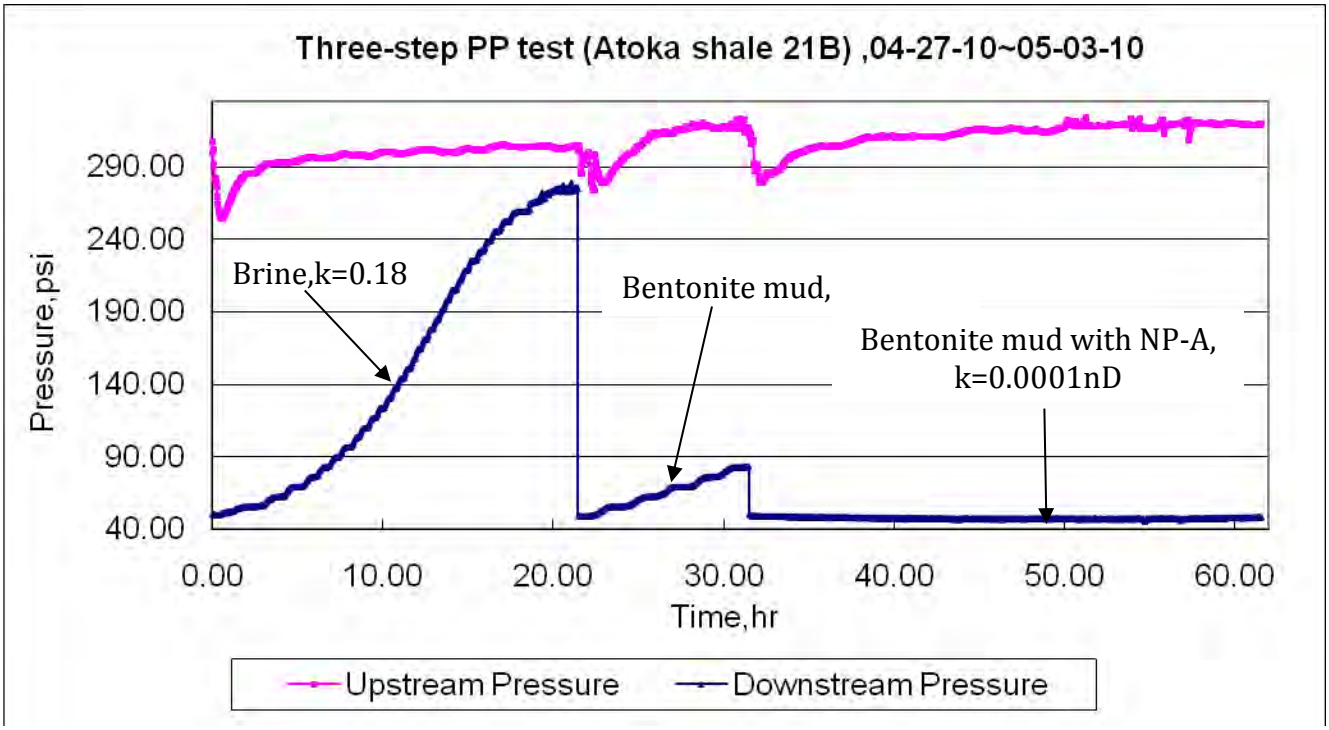

Figure 5.2: Continuous PP plot of Atoka Shale 21B, in Bentonite Mud Containing NP-A

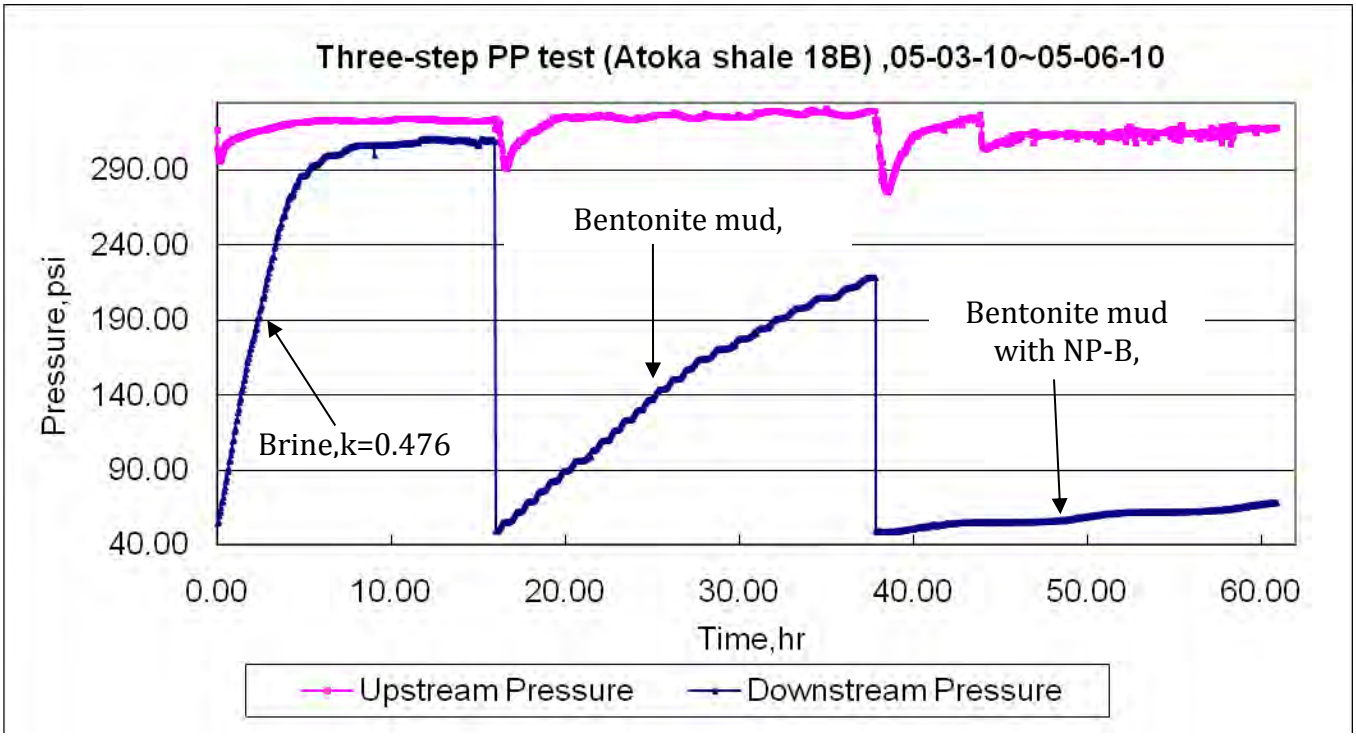

Figure 5.3: Continuous PP plot of Atoka shale 18B Contacted with Bentonite Mud Containing NP-B

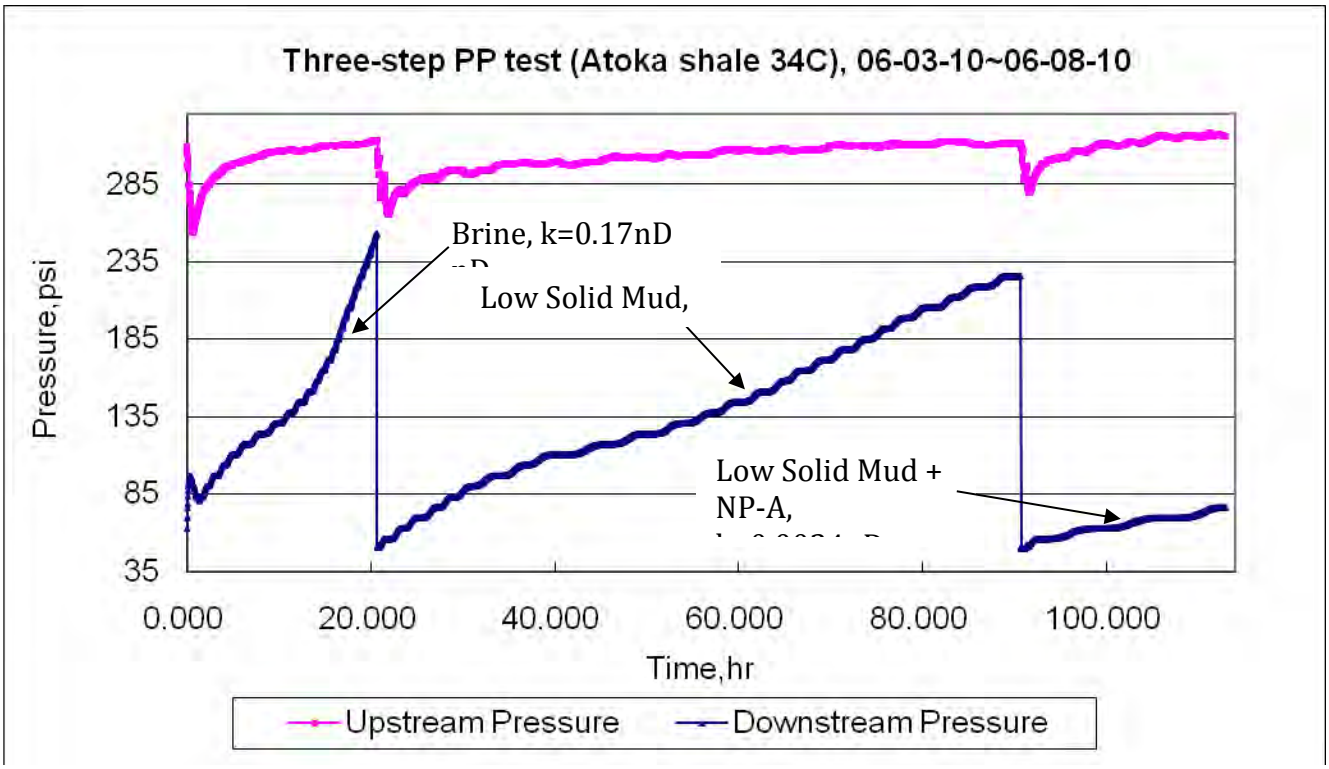

Figure 5.4: Continuous PP plot of Atoka shale 34C in LSM Containing NP-A

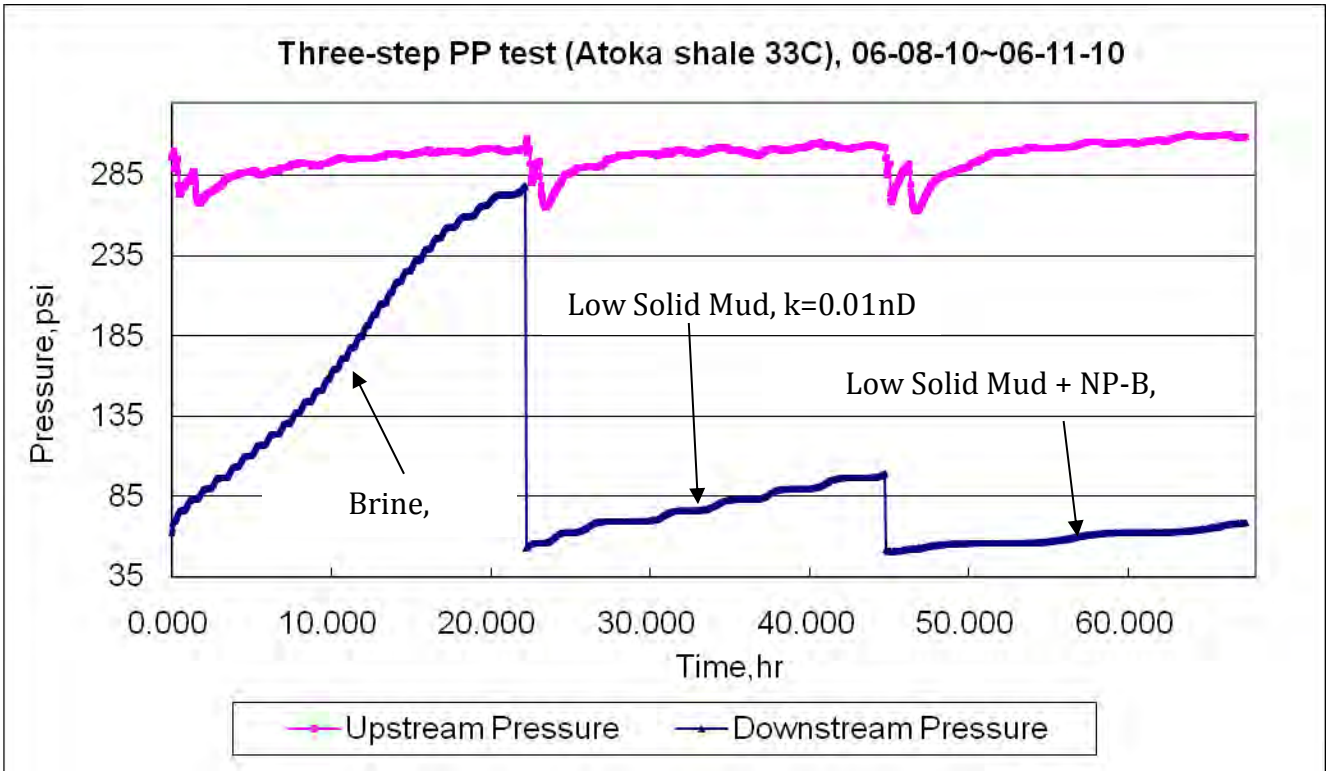

Figure 5.5: Continuous PP plot of Atoka shale 33C Contacted by LSM Containing NP-B

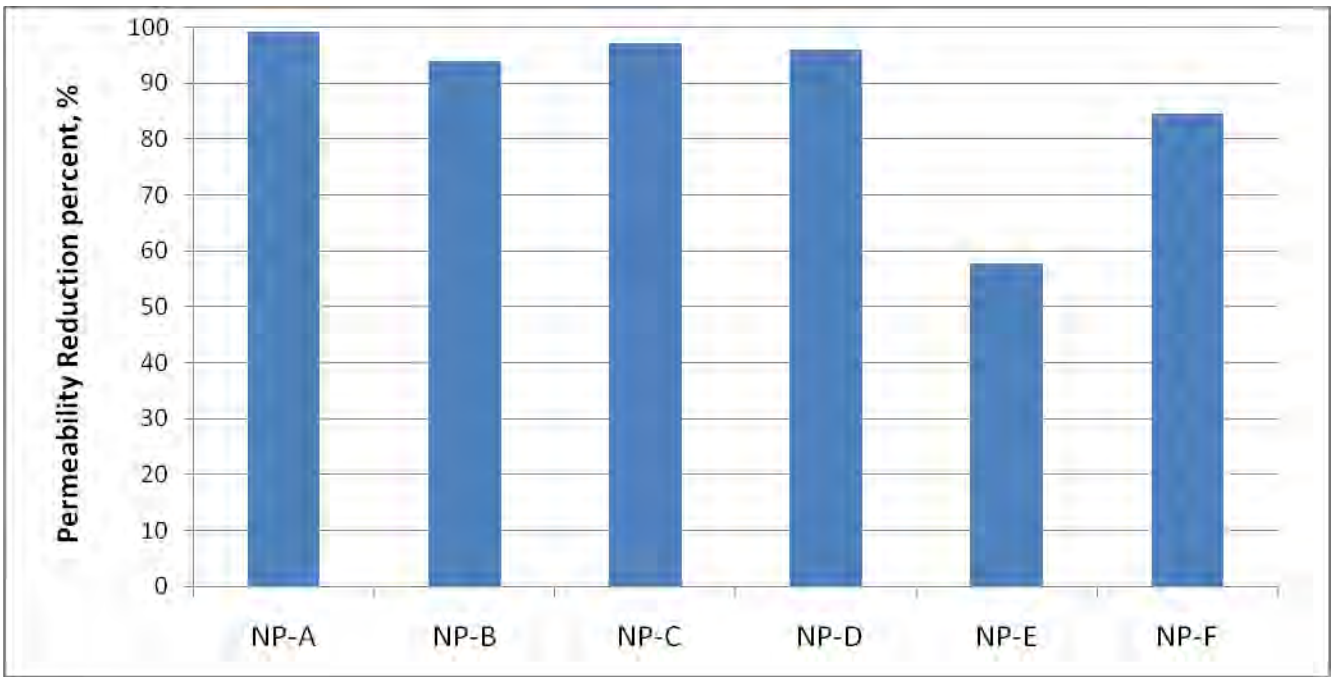

Figure 5.6: Permeability Reduction of Atoka shale with bentonite mud w/wo NPs

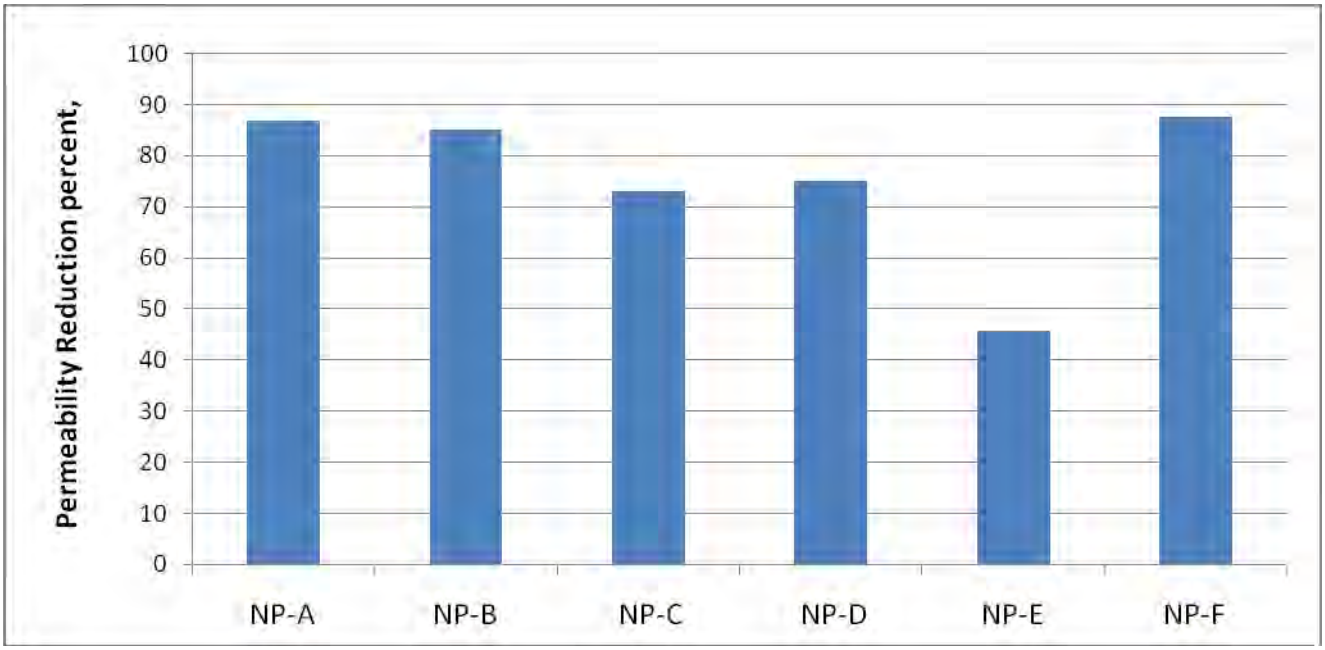

Figure 5.7: Permeability Reduction of Atoka shale with LSM w/wo NPs

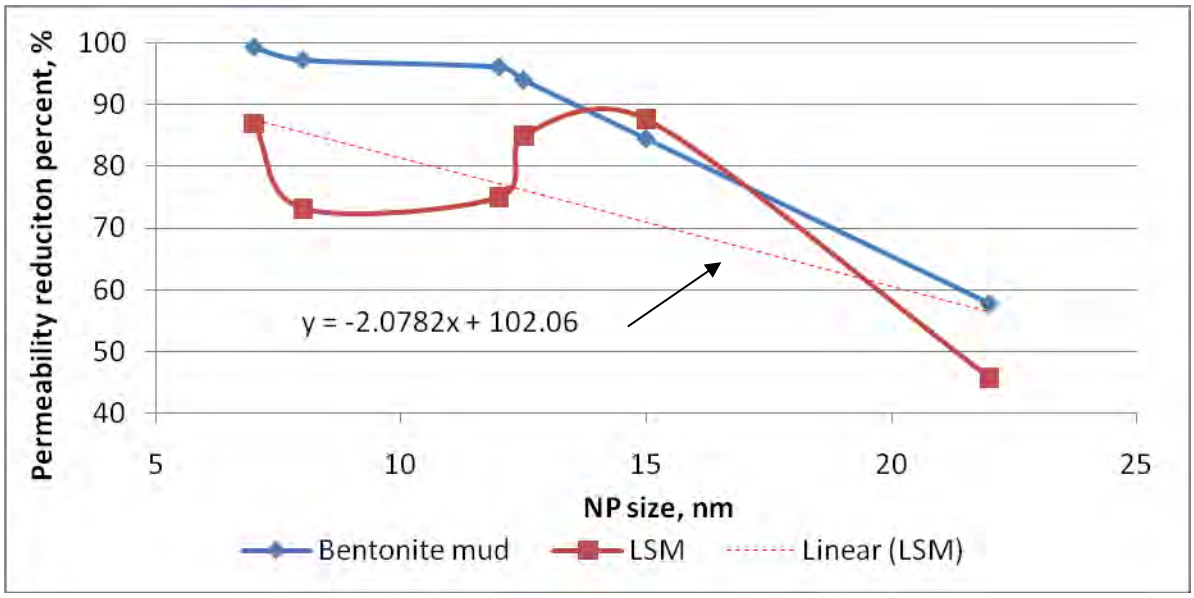

Figure 5.8: Effect of NP size on permeability reduction percent (Δk, %)

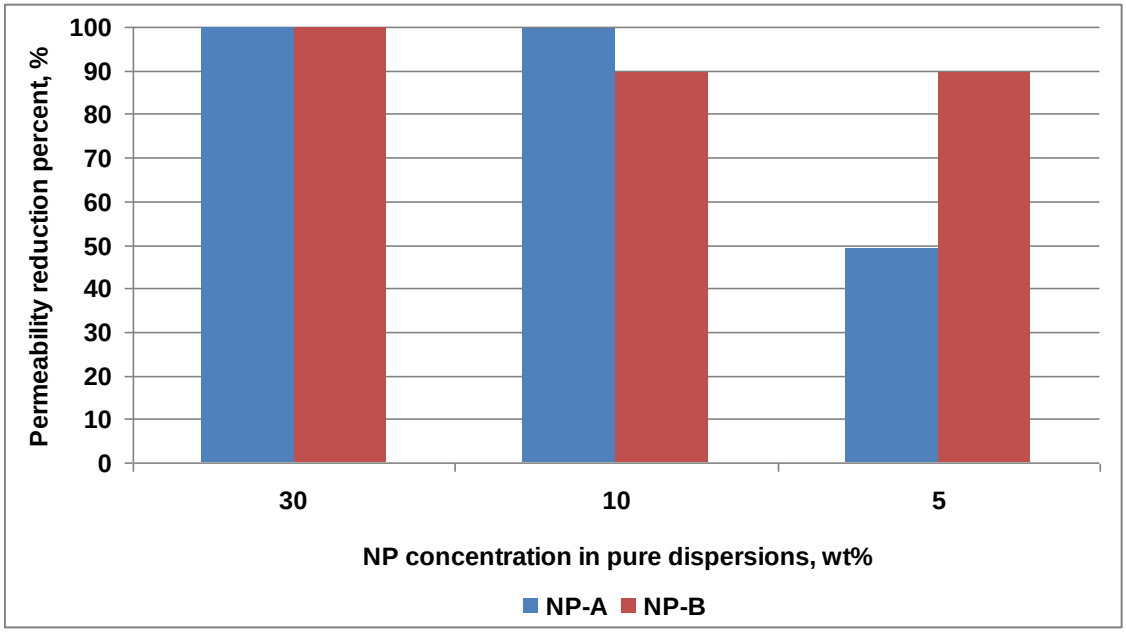

Figure 5.9: Effect of NP concentration in pure dispersions on permeability reduction percent

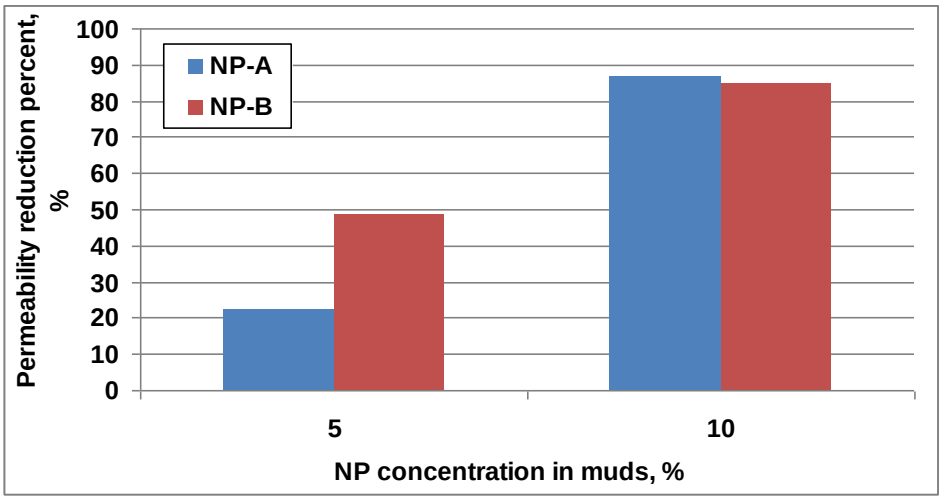

Figure 5.10: Effect of NP concentration in muds on permeability reduction percent

Chapter 6: Use of Nanoparticles in Field Muds

The nanoparticles selected based on tests reported in Chapters 4 and 5 were tested as additives to field muds provided by Newpark and MI Drilling Fluids. These tests are critical in that they show if the nanoparticles are compatible with the complex mixture of additives that are frequently present in field muds.

6.1 Field Mud Properties

Four different field muds were used to study the effect of NP's in contact with Atoka and GOM shales. Properties of each field mud before and after nanoparticle addition are presented in Tables 6.1 and 6.2. Muds were preserved from fermentation by adding 0.5 ppb X Cide 102 (Microbiocide) every week. CSN-4 type nanoparticles were used for these mixtures since it is stable in high temperature and it does not produce flocculation when mixed with muds. The properties of CSN-4 are listed in Chapter 5.1.

Table 6.1: Field muds properties.

Mud Properties	Newpark Mud A	Newpark Mud B	MISwaco Mud C	MISwaco Mud D
Density, lb/gal	12	11.6	9.3	9.8
PV @ 80 F, cP	18	20	28	11
YP @ 80 F, lb/100ft^2	4	11	36	9
Solids Content, % by Volume	19.5	18.5	18.5	11
Water Content, % by Volume	77	79	79	88
Other Content, % by Volume	3.5	2.5	2.5	1
MBT, ppb Bentonite eq.	42.5	40	3.5	26.25
pH	8.7	11.4	9.4	11.4
Chlorides, mg/L	1900	65000	28000	320
LignoSulfonate Concentration, lb/bbl	100			
Water activity	1	0 .93	0 .98	1

Table 6.2: Properties of the field muds modified with CSN-4.

Mud-NP Mixture Properties	CSN-4 Mud A+NP	CSN-4 Mud B+NP	CSN-4 Mud C+NP	CSN-4 Mud D+NP
PV @ 80 F, cP	8	10	19	6
YP @ 80 F, lb/100ft^2	1	5	19	2
Total solid vol %	22.5	21.5	21.2	15.5
NP wt %	10	10	10	10
NP vol %	8.3	7.8	6.9	7.1
pH	9	11	9	11

6.2 Field Muds in contact with Atoka shale

Test 6.1 was performed to observe the performance of Mud A. Table 6.3 gives the test conditions. As seen in Figure 6.1, the bottom pressure stabilized at 60 psi differential pressure in 25 hours. Using the transient method discussed in Chapter 4 the permeability of the sample was determined to be 0.044 nd. The pressure drop of 15 psi in the last 8 hours of this test is believed to be result of temporary temperature change in the laboratory.

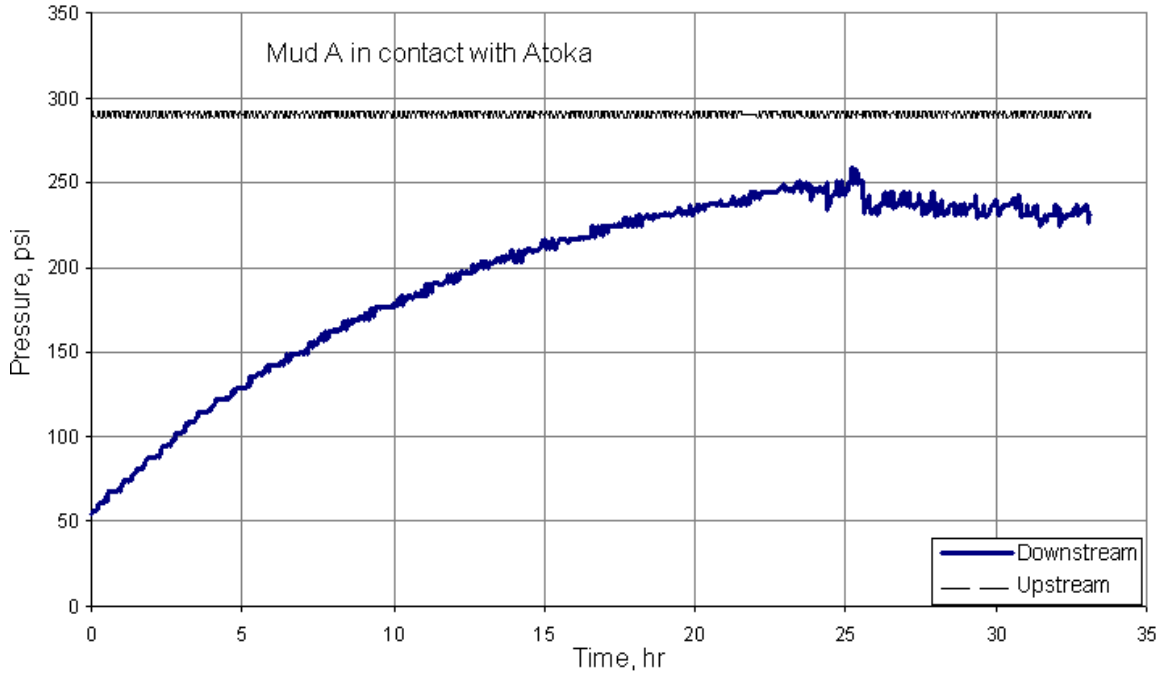

Figure 6.1: Results of Test 6.1 that was performed in contact with Atoka shale.

Table 6.3: Conditions for Test 6.1.

Test	6.1
Date	11/3/2008
Shale	Atoka
Top Fluid	Mud A
NP wt%	0
Bottom Fluid	Brine
Aw top	1
Aw Bottom	0.98
Aw shale	0.98
Top Pres. (Psi)	290
Bottom Pres. (Psi)	50
Result	Stabilized at 60 psi differential pressure in 25 hours with a permeability of 0.044 nd.

Test 6.2 was performed to observe the effect of the CSN-4 dispersion on the performance of Mud A. Mud A, which was modified with 10 wt% CSN-4, was flowed across the Atoka shale sample. Table 6.4 shows the test conditions and Table 6.5 shows the mud composition. As shown in Figure 6.2 the bottom pressure stabilized at 170 psi differential pressure in 35 hours. As shown in Figure 6.3, adding CSN-4 dispersion to the Field Mud A reduced the fluid penetration by 72 % in 36 hours. Using the transient method discussed in Chapter 4 the permeability of the sample was determined to be 0.0038 nd.

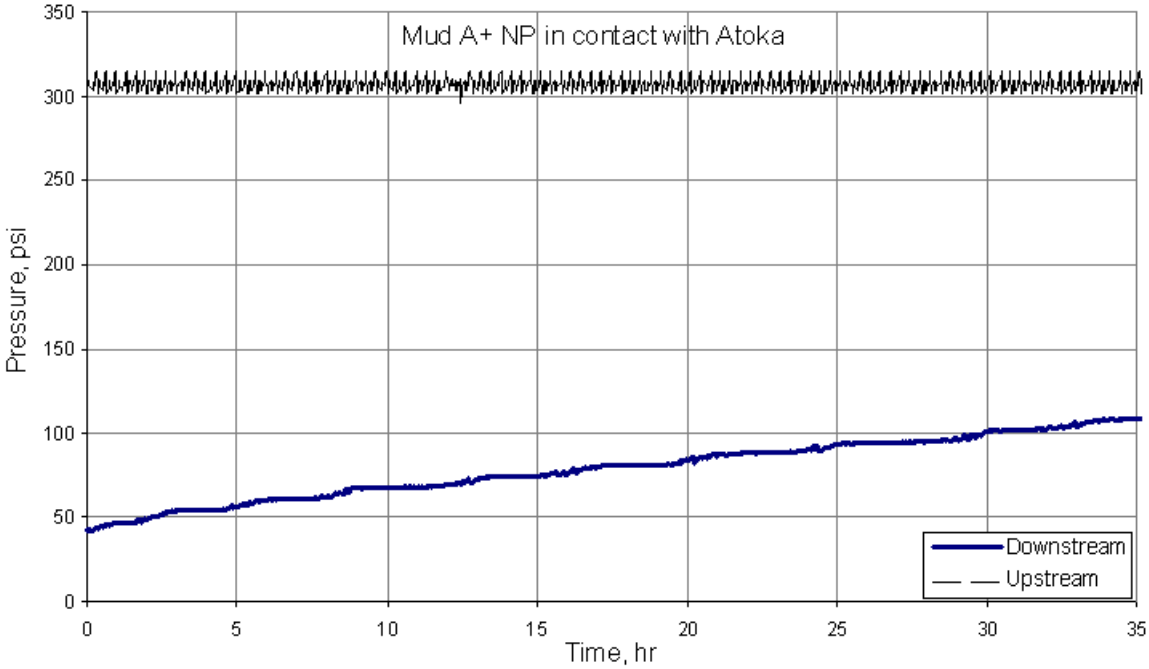

Figure 6.2: Results of Test 6.2 that was performed in contact with Atoka shale.

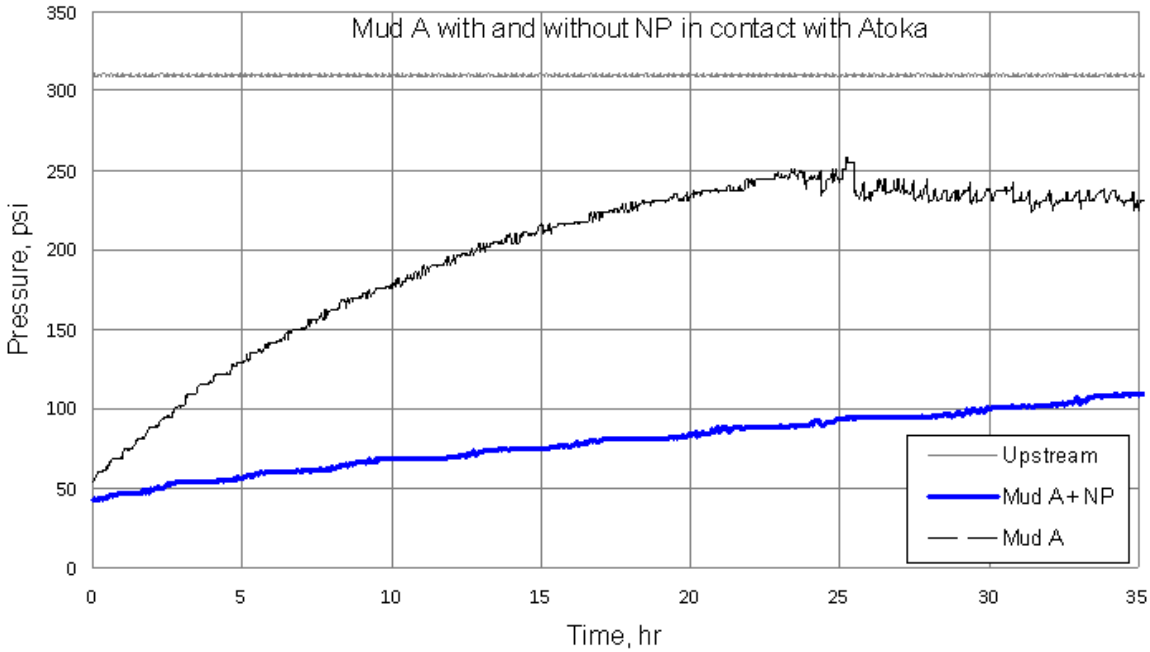

Figure 6.3: Comparison of Mud A with and without NP in contact with Atoka shale.

Table 6.4: Conditions for Test 6.2

Test	6.2
Date	11/18/2008
Shale	Atoka
NP type	CSN-4
Top Fluid	Mud A +NP
NP wt%	10
NP Size (nm)	20
Bottom Fluid	Brine
Aw top	1
Aw Bottom	0.98
Aw shale	0.98
Top Pres. (Psi)	290
Bottom Pres. (Psi)	50
Result	Maintained 170 psi differential pressure for 35 hours with a permeability of 0.0038 nd.

Table 6.5: Composition in Test 6.2

Mud A+ NP	Volume, cc	Mass, gr
Mud solid	17.33	56.44
mud water	71.56	71.56
mud total	88.89	128.00
NP solid	10.13	16.80
NP sol. water	23.20	23.20
NP sol. total	33.33	40.00
Total Solid %	22.5%	43.6%
NP %	8.3%	10.0%

Test 6.5 was performed to observe the response of Mud B in contact with Atoka shale. Table 6.6 shows the test conditions. As seen in Figure 6.4, the bottom pressure stabilized at 180 psi differential pressure in 30 hours. Using the transient method discussed in Chapter 4 the permeability of the sample was determined to be 0.0047 nd.

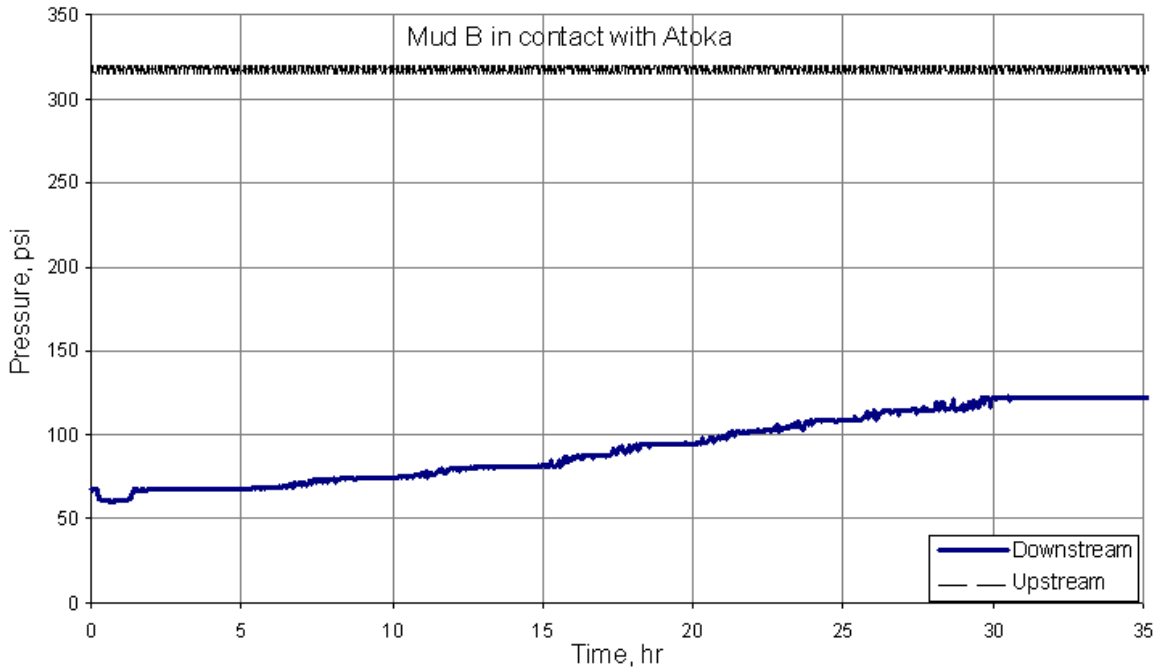

Figure 6.4: Results of Test 6.3 that was performed in contact with Atoka shale.

Table 6.6: Conditions for Test 6.3.

Test	6.3
Date	12/1/2008
Shale	Atoka
Top Fluid	Mud B
NP wt%	0
Bottom Fluid	Brine
Aw top	0.93
Aw Bottom	0.98
Aw shale	0.98
Top Pres. (Psi)	330
Bottom Pres. (Psi)	70
Result	Stabilized at 200 psi differential pressure in 30 hours with a permeability of 0.0047 nd.

Test 6.4 was performed to observe the effect of the CSN-4 dispersion on the response of Mud B in contact with Atoka shale. Table 6.7 shows the test conditions and Table 6.8 shows the mud composition. Mud B, which was modified with 10 wt% CSN-4, was flowed across the Atoka shale sample. As seen in Figure 6.5, the bottom pressure stabilized at 210 psi differential pressure in 20 hours. As shown in Figure 6.6, adding CSN-4 dispersion to the Field Mud B reduced the fluid penetration by 16 % in 36 hours. Using the transient method discussed in Chapter 4 the permeability of the sample was determined to be 0.0058 nd.

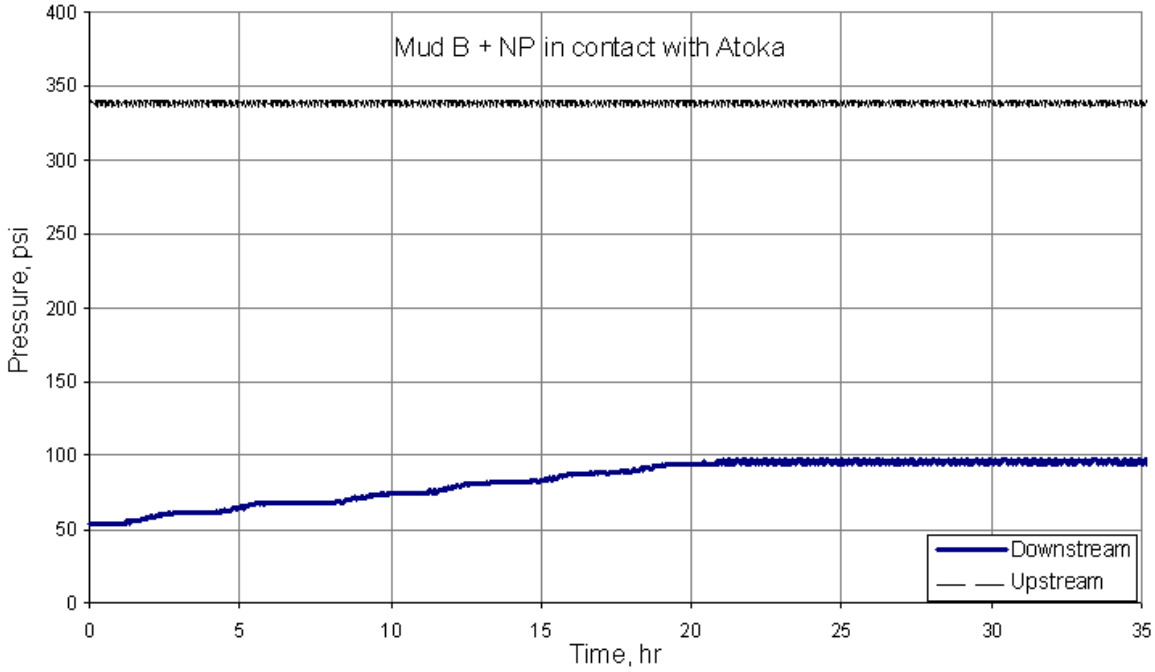

Figure 6.5: Results of Test 6.4 that was performed in contact with Atoka shale.

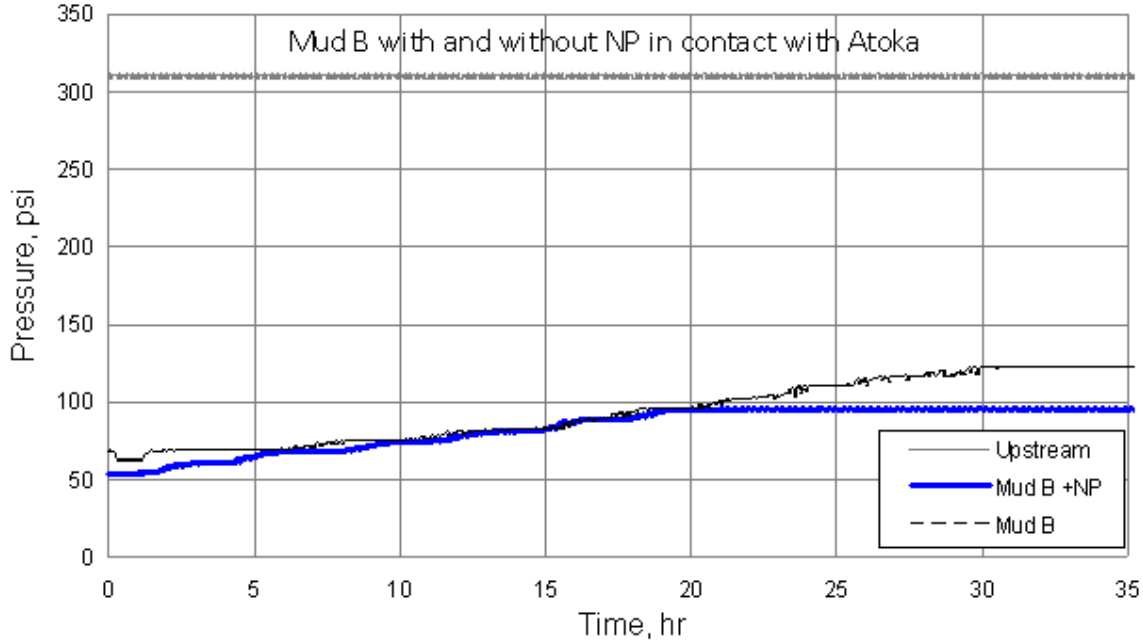

Figure 6.6: Comparison of Mud B with and without NP in contact with Atoka shale.

Table 6.7: Conditions for Test 6.4.

Test	6.4
Date	11/29/2008
Shale	Atoka
NP type	CSN-4
Top Fluid	Mud B +NP
NP wt%	10
NP Size (nm)	20
Bottom Fluid	Brine
Aw top	0.93
Aw Bottom	0.98
Aw shale	0.98
Top Pres. (Psi)	340
Bottom Pres. (Psi)	50
Result	Stabilized at 240 psi differential pressure in 20 hours with a permeability of 0.0058 nd.

Table 6.8: Mud composition in Test 6.4.

Mud B+ CSN-4	Volume, cc	Mass, gr
Mud solid	17.94	48.97
mud water	79.03	79.03
mud total	96.97	128.00
NP solid	10.13	16.80
NP sol. water	23.20	23.20
NP sol. total	33.33	40.00
Total Solid %	21.5%	39.1%
NP %	7.8%	10.0%

Test 6.5 was performed to observe the response of Mud C in contact with Atoka shale. Table 6.9 shows the test conditions. As seen in Figure 6.7, the bottom pressure stabilized at 70 psi differential pressure in 32 hours. Using the transient method discussed in Chapter 4 the permeability of the sample was determined to be 0.028 nd.

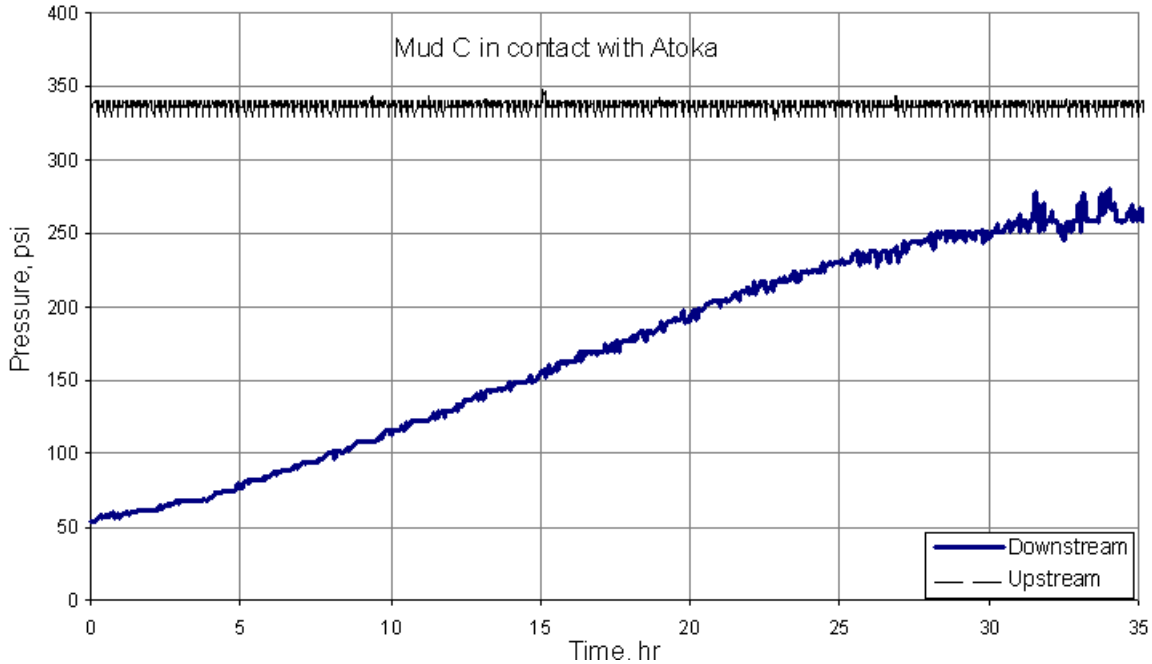

Figure 6.7: Results of Test 6.5 that was performed in contact with Atoka shale.

Table 6.9: Conditions for Test 6.5.

Test	6.5
Date	12/1/2008
Shale	Atoka
Top Fluid	Mud C
NP wt%	0
Bottom Fluid	Brine
Aw top	0.98
Aw Bottom	0.98
Aw shale	0.98
Top Pres. (Psi)	340
Bottom Pres. (Psi)	50
Result	Stabilized at 80 psi differential pressure in 30 hours with a permeability of 0.028 nd.

Test 6.6 was performed to observe the effect of NP's on the response of Mud C in contact with Atoka shale. Table 6.10 and Table 6.11 show the test conditions. As seen in Figure 6.8, the bottom pressure stabilized at 120 psi differential pressure in 40 hours. As shown in Figure 6.9, adding CSN-4 dispersion to the Field Mud C reduced the fluid penetration by 38 % in 36 hours. Using the transient method discussed in Chapter 4 the permeability of the sample was determined to be 0.0114 nd.

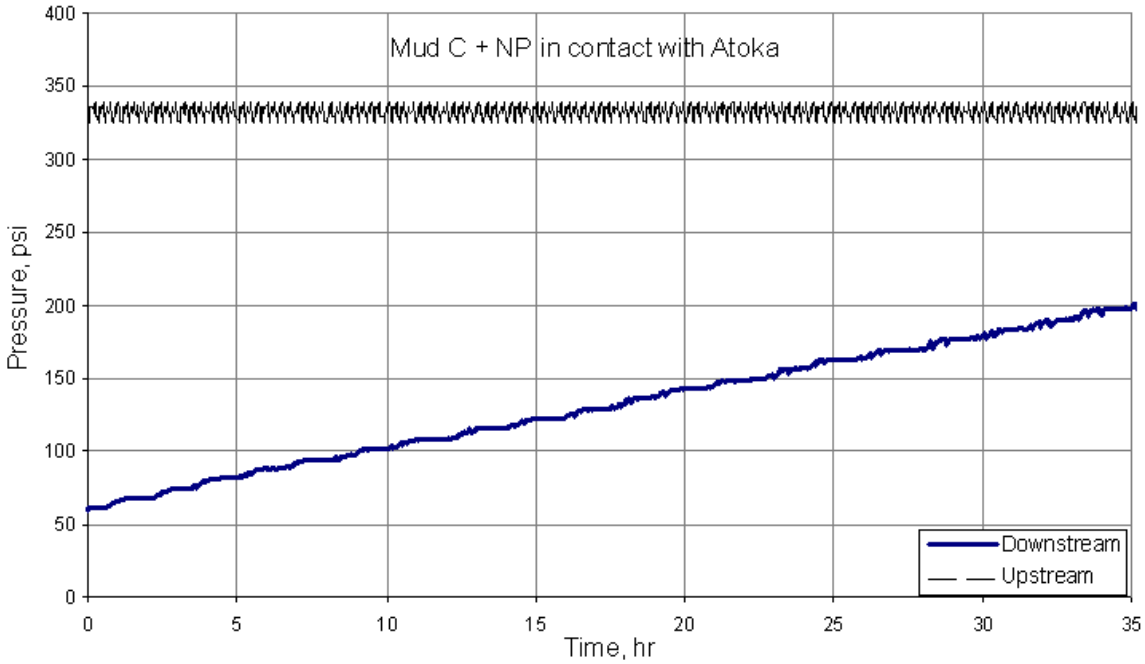

Figure 6.8: Results of Test 6.6 that was performed in contact with Atoka shale.

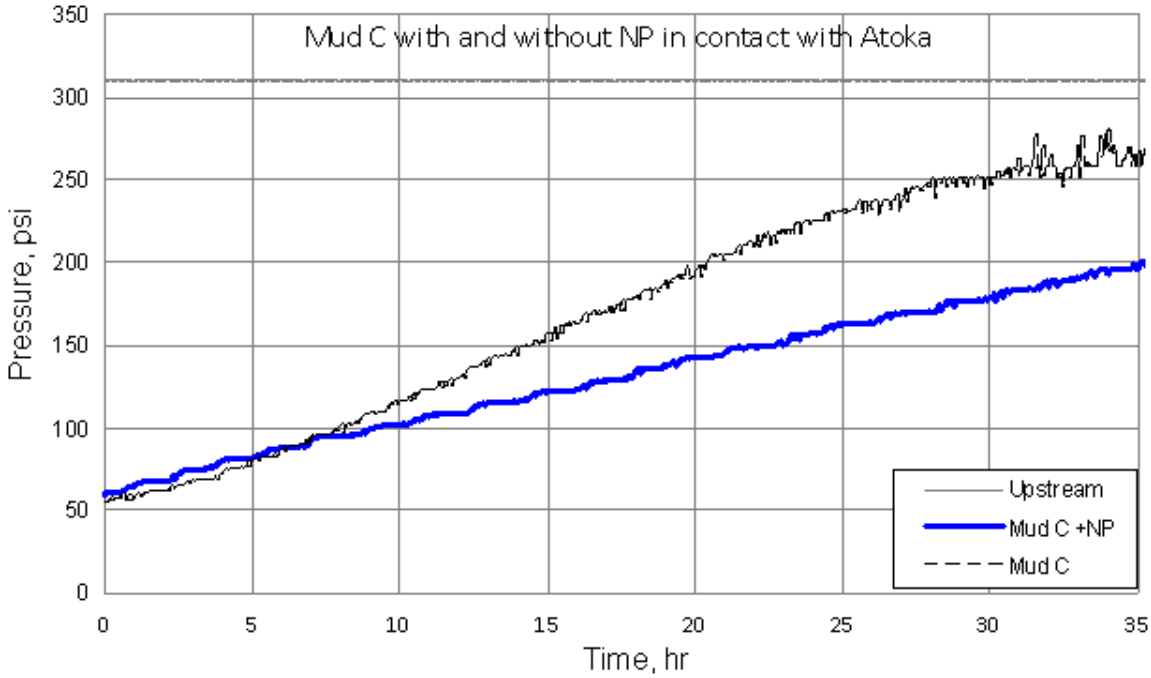

Figure 6.11: Comparison of Mud C with and without NP in contact with Atoka shale.

Table 6.10: Conditions for Test 6.6

Test	6.6
Date	12/15/2008
Shale	Atoka
NP type	CSN-4
Top Fluid	Mud C+ NP
NP wt%	10
NP Size (nm)	20
Bottom Fluid	Brine
Aw top	0.98
Aw Bottom	0.98
Aw shale	0.98
Top Pres. (Psi)	335
Bottom Pres. (Psi)	55
Result	Stabilized at 120 psi differential pressure in 40 hours with a permeability of 0.0114 nd.

Table 6.11: Mud composition in Test 6.6

Mud C+ CSN-4	Volume, cc	Mass, gr
Mud solid	21.14	34.86
mud water	93.14	93.14
mud total	114.29	128.00
NP solid	10.13	16.80
NP sol. water	23.20	23.20
NP sol. total	33.33	40.00
Total Solid %	21.2%	30.7%
NP %	6.9%	10.0%

Test 6.7 was performed to observe the response of Mud D in contact with Atoka shale. Table 6.12 shows the test conditions. As seen in Figure 6.10, the bottom pressure stabilized at 150 psi differential pressure in 40 hours. Using the transient method discussed in Chapter 4 the permeability of the sample was determined to be 0.0056 nd.

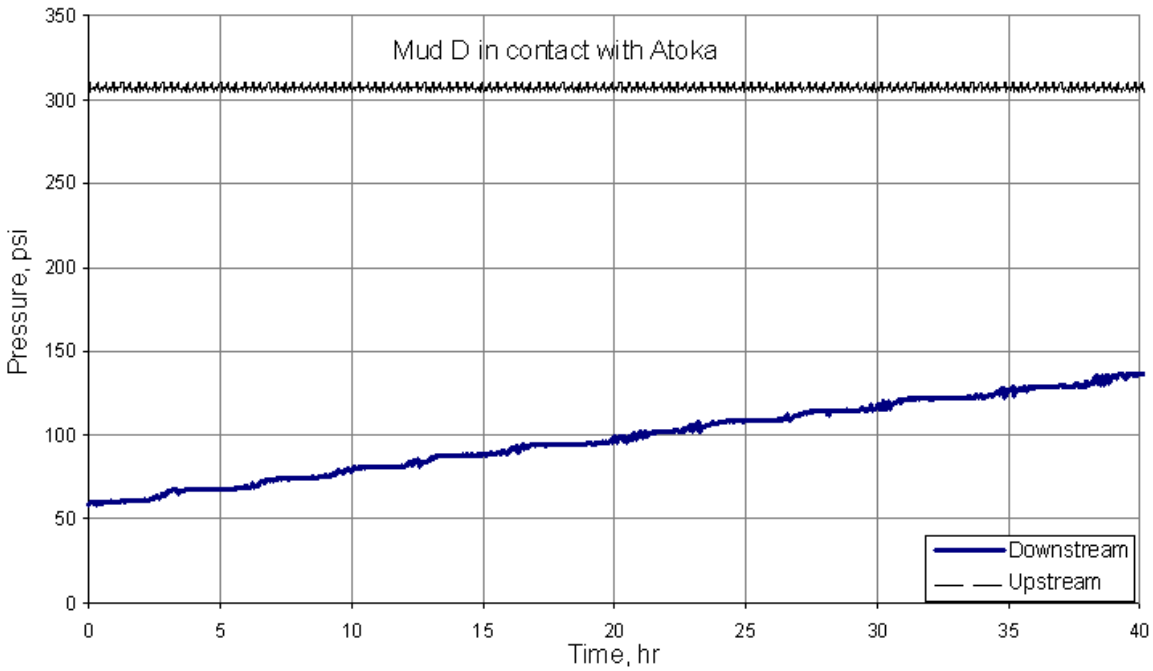

Figure 6.10: Results of Test 6.7 that was performed in contact with Atoka shale.

Table 6.12: Conditions for Test 6.7.

Test	6.7
Date	12/18/2008
Shale	Atoka
Top Fluid	Mud D
NP wt%	0
Bottom Fluid	Brine
Aw top	1
Aw Bottom	0.98
Aw shale	0.98
Top Pres. (Psi)	305
Bottom Pres. (Psi)	55
Result	Stabilized at 150 psi differential pressure in 40 hours with a permeability of 0.0056nd.

Test 6.8 was performed to observe the effect of NP's on the response of Mud D in contact with Atoka shale. Table 6.13 shows the test conditions and Table 6.14 shows the mud composition. As seen in Figure 6.11, the bottom pressure stabilized at 200 psi differential pressure in 30 hours. As shown in Figure 6.12, adding CSN-4 dispersion to the Field Mud D reduced the fluid penetration by 25 % in 36 hours. Using the transient method discussed in Chapter 4 the permeability of the sample was determined to be 0.004 nd.

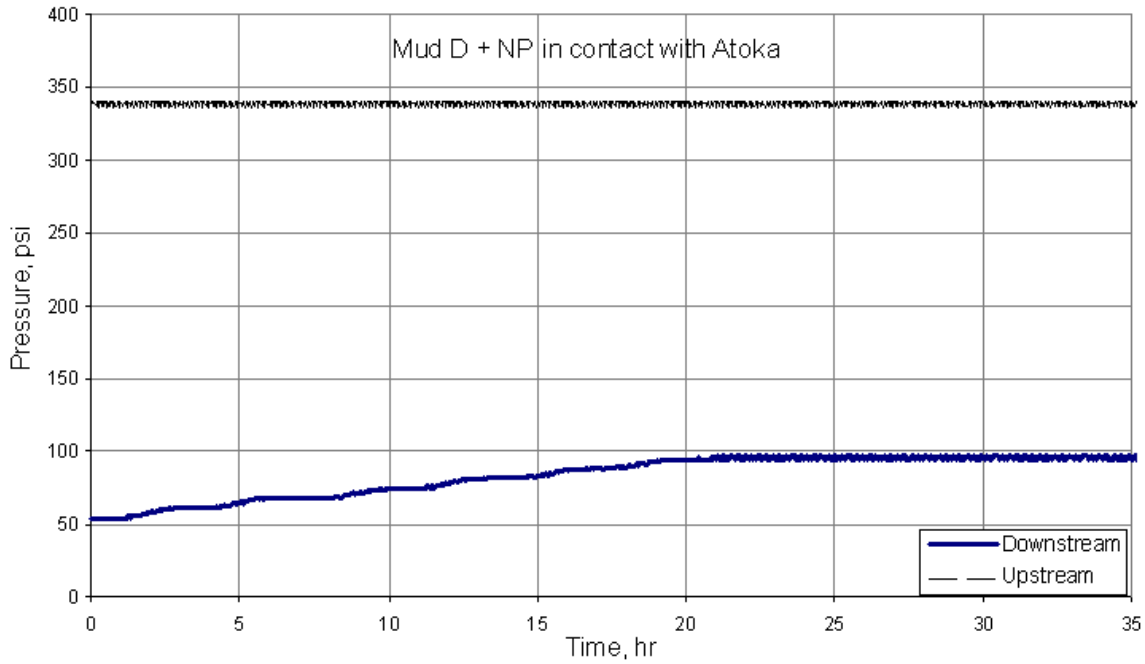

Figure 6.11: Results of Test 6.8 that was performed in contact with Atoka shale.

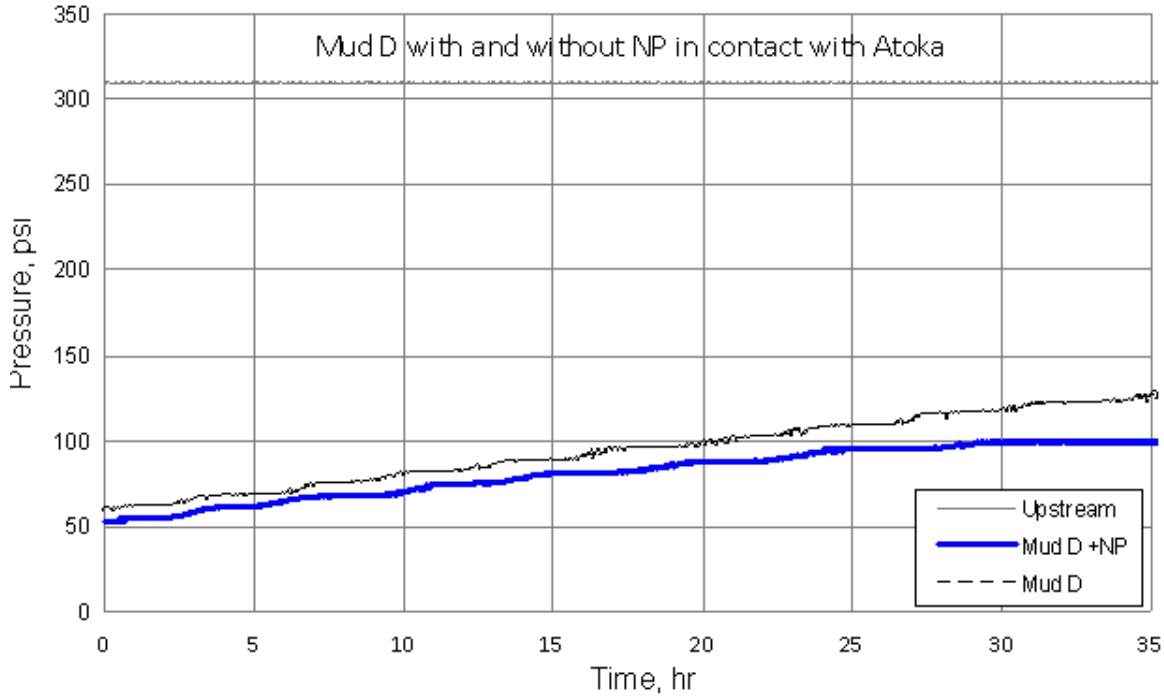

Figure 6.12: Comparison of Mud D with and without NP in contact with Atoka shale.

Table 6.13: Conditions for Test 6.8.

Test	6.8
Date	12/19/2008
Shale	Atoka
NP type	CSN-4
Top Fluid	Mud D+ NP
NP wt%	10
NP Size (nm)	20
Bottom Fluid	Brine
Aw top	1
Aw Bottom	0.98
Aw shale	0.98
Top Pres. (Psi)	300
Bottom Pres. (Psi)	50
Result	Stabilized at 200 psi differential pressure in 30 hours with a permeability of 0.0056 nd.

Table 6.14: Mud composition in Test 6.8.

Mud D+ CSN-4	Volume, cc	Mass, gr
Mud solid	12.03	30.63
mud water	97.37	97.37
mud total	109.40	128.00
NP solid	10.13	16.80
NP sol. water	23.20	23.20
NP sol. total	33.33	40.00
Total Solid %	15.5%	28.2%
NP %	7.1%	10.0%

Permeability calculations for each field mud test are done to observe the effect of nanoparticles. As seen in Figure 6.13 and Table 6.15, nanoparticle additions to field muds reduced the permeability of Atoka shale by factor of 11 for Field Mud A, 2.45 for Field Mud C and 1.4 for Field Mud D.

Table 6.15: Permeability values obtained with and without nanoparticles for Atoka

Test	Rock	Fluid	Permeability (nd)
4	Atoka	Brine	0.41
24	Atoka	Mud A	0.044
25	Atoka	Mud A Modified	0.0038
27	Atoka	Mud B	0.0047
28	Atoka	Mud B Modified	0.0058
29	Atoka	Mud C	0.028
32	Atoka	Mud C Modified	0.0114
33	Atoka	Mud D	0.0056
34	Atoka	Mud D Modified	0.004

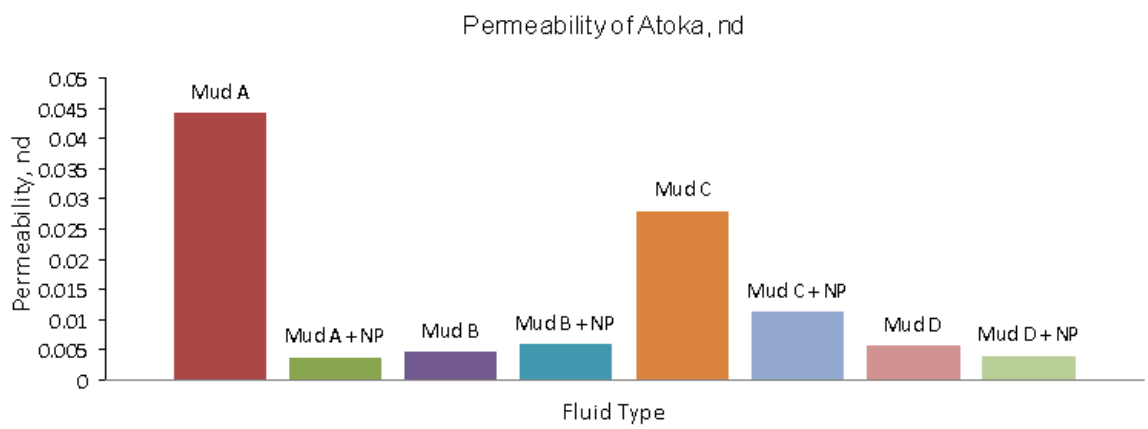

Figure 6.13: Permeability chart of Atoka shale

6.3 Field Muds in contact with GOM shale

Test 6.9 was performed to observe the response of Mud A in contact with GOM shale. Table 6.16 shows the test conditions. As seen in Figure 6.14, the bottom pressure stabilized at 70 psi differential pressure in 20 hours. Using the transient method discussed in Chapter 4 the permeability of the sample was determined to be 0.038 nd.

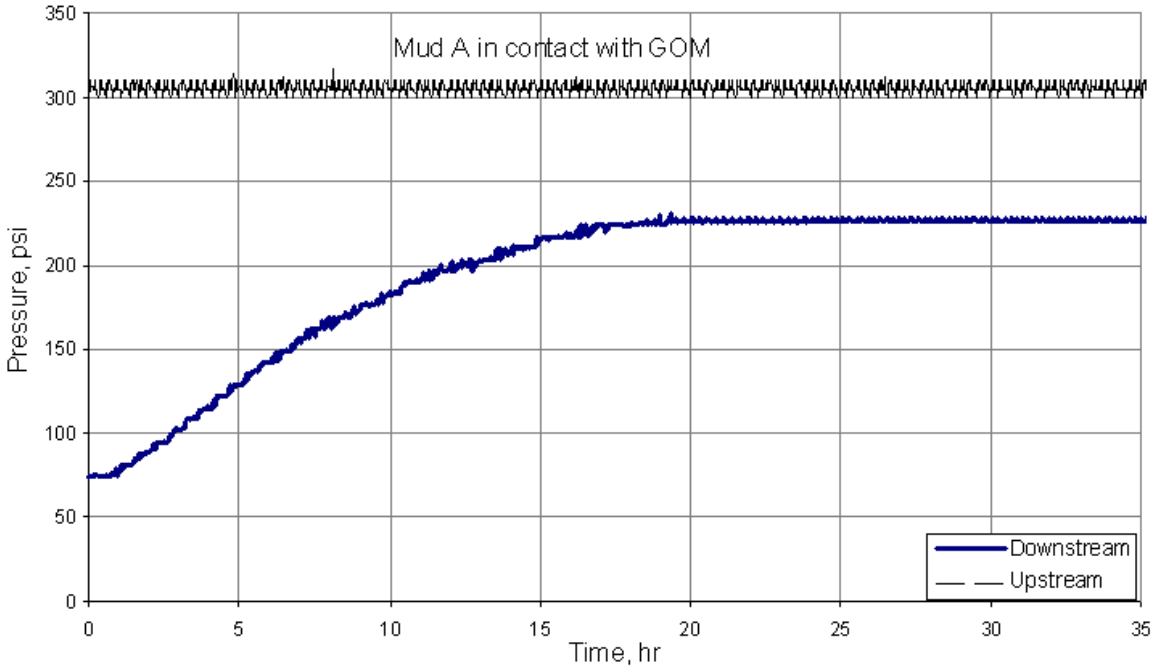

Figure 6.14: Results of Test 6.9 that was performed in contact with GOM shale.

Table 6.16: Conditions for Test 6.9.

Test	6.9
Date	12/12/2008
Shale	GOM
Top Fluid	Mud A
NP wt%	0
Bottom Fluid	Brine
Aw top	1
Aw Bottom	0.98
Aw shale	0.98
Top Pres. (Psi)	300
Bottom Pres. (Psi)	70
Result	Stabilized at 70 psi differential pressure in 20 hours with a permeability of 0.038 nd.

Test 6.10 was performed to observe the effect of NP's on the response of Field Mud A in contact with GOM shale. Table 6.17 shows the test conditions and Table 6.18 shows the mud composition. As seen in Figure 6.15, the bottom pressure stabilized at 70 psi differential pressure in 20 hours. As shown in Figure 6.16, adding CSN-4 dispersion to the Field Mud A reduced the fluid penetration by 27 % in 36 hours. Using the transient method discussed in Chapter 4 the permeability of the sample was determined to be 0.014 nd.

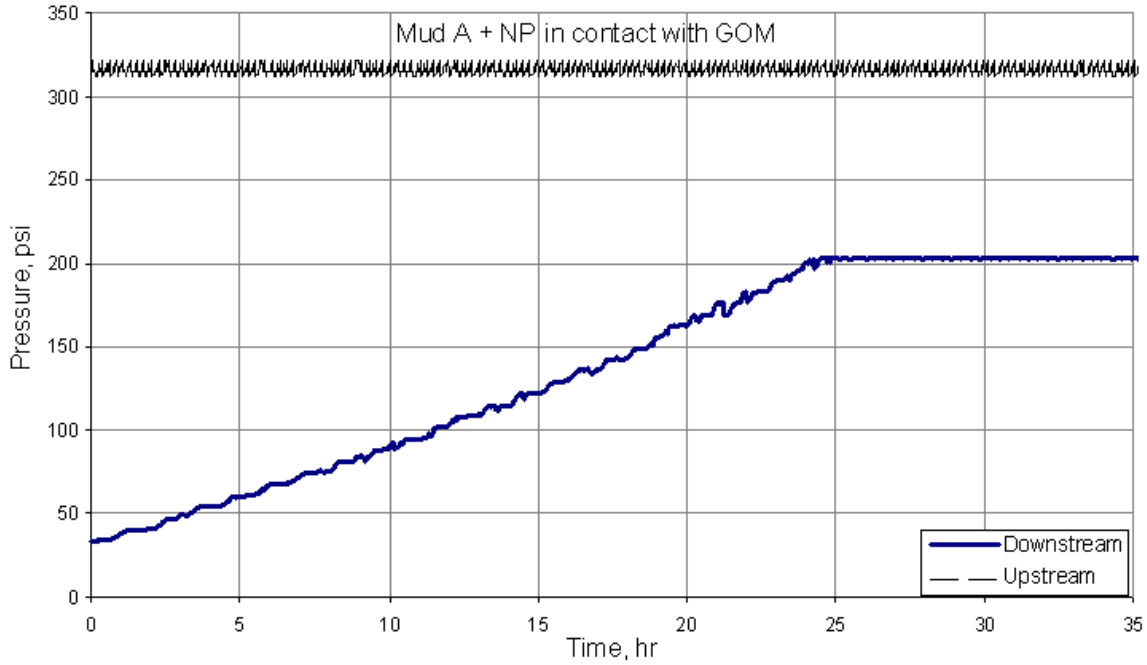

Figure 6.15: Results of Test 6.10 that was performed in contact with GOM shale.

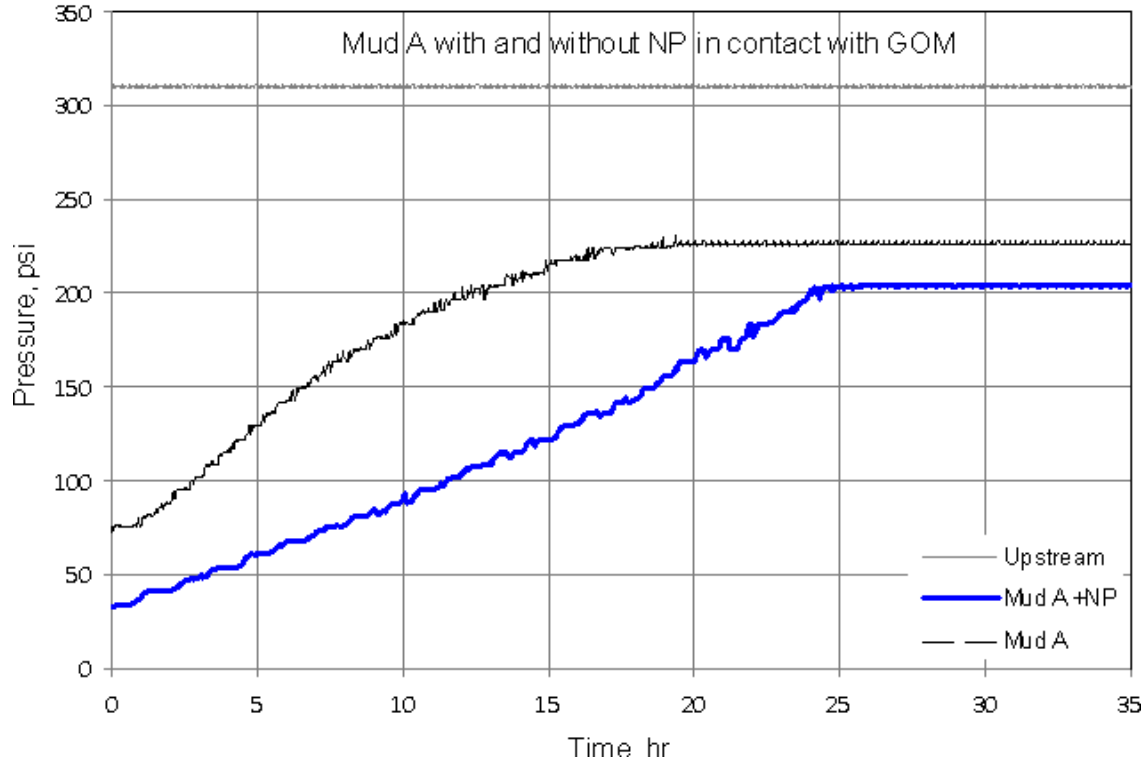

Figure 6.16: Comparison of Mud A with and without NP in contact with GOM shale.

Table 6.17: Conditions for Test 6.10.

Test	6.10
Date	12/14/2008
Shale	GOM
NP type	CSN-4
Top Fluid	Mud A + NP
NP wt%	10
NP Size (nm)	20
Bottom Fluid	Brine
Aw top	1
Aw Bottom	0.98
Aw shale	0.98
Top Pres. (Psi)	315
Bottom Pres. (Psi)	40
Result	Stabilized at 140 psi differential pressure in 24 hours with a permeability of 0.014 D.

Table 6.18: Mud compostion in Test 6.10

Mud A+ CSN-4	Volume, cc	Mass, gr
Mud solid	17.33	56.44
mud water	71.56	71.56
mud total	88.89	128.00
NP solid	10.13	16.80
NP sol. water	23.20	23.20
NP sol. total	33.33	40.00
Total Solid %	22.5%	43.6%
NP %	8.3%	10.0%

Test 6.11 was performed to observe the response of Mud B in contact with GOM shale. Table 6.19 shows the test conditions. As seen in Figure 6.17, the bottom pressure stabilized at 120 psi differential pressure in 11 hours. Using the transient method discussed in Chapter 4 the permeability of the sample was determined to be 0.0404 nd.

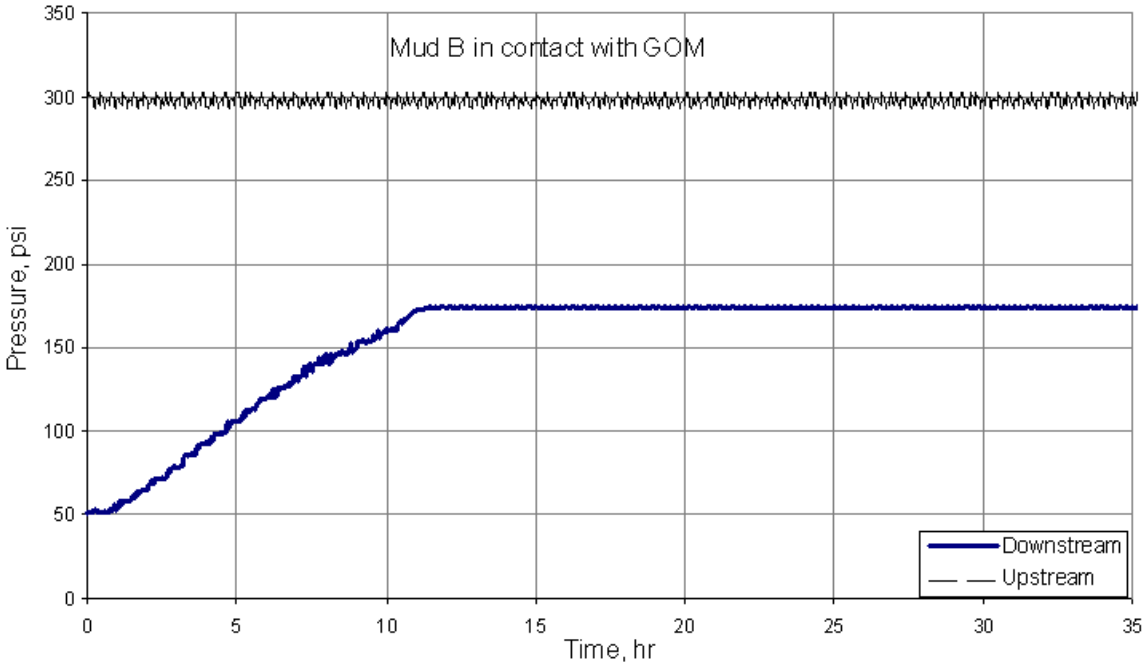

Figure 6.17: Results of Test 6.11 that was performed in contact with GOM shale.

Table 6.19: Conditions for Test 6.11.

Test	6.11
Date	12/20/2008
Shale	GOM
Top Fluid	Mud B
NP wt%	0
Bottom Fluid	Brine
Aw top	0.93
Aw Bottom	0.98
Aw shale	0.98
Top Pres. (Psi)	300
Bottom Pres. (Psi)	50
Result	Stabilized at 120 psi differential pressure in 11 hours with a permeability of 0.0404 nd.

Test 6.12 was performed to observe the effect of NP's on the response of Mud B in contact with GOM shale. Table 6.20 shows the test conditions and Table 6.21 shows the mud composition. As seen in Figure 6.18, the bottom pressure stabilized at 150 psi differential pressure in 10 hours. As shown in Figure 6.19, adding CSN-4 dispersion to the Field Mud B reduced the fluid penetration by 25 % in 36 hours. Using the transient method discussed in Chapter 4 the permeability of the sample was determined to be 0.0408 nd.

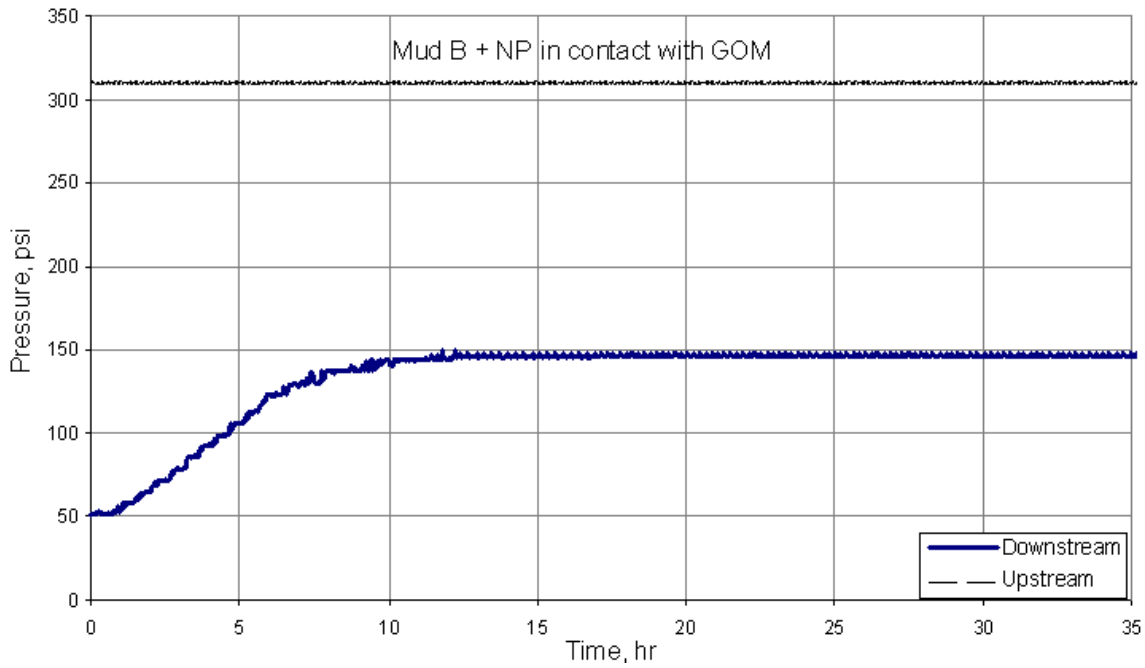

Figure 6.18: Results of Test 6.12 that was performed in contact with GOM shale.

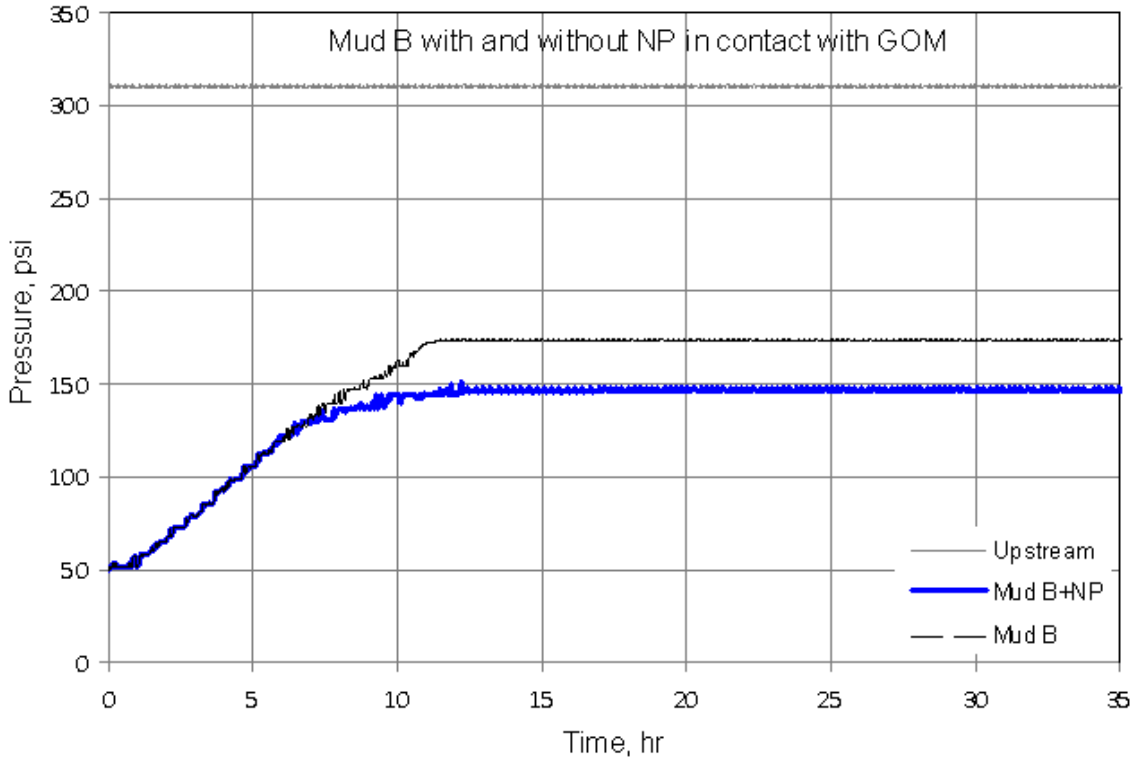

Figure 6.19: Comparison of Mud B with and without NP in contact with GOM shale.

Table 6.20: Conditions for Test 6.12.

Test	6.12
Date	12/22/2008
Shale	GOM
NP type	CSN-4
Top Fluid	Mud B+ NP
NP wt%	10
NP Size (nm)	20
Bottom Fluid	Brine
Aw top	0.93
Aw Bottom	0.98
Aw shale	0.98
Top Pres. (Psi)	310
Bottom Pres. (Psi)	50
Result	Stabilized at 160 psi differential pressure in 10 hours with a permeability of 0.0408 nd.

Table 6.21: Mud composition in Test 6.12.

Mud B+ CSN-4	Volume, cc	Weight, gr
Mud solid	17.94	48.97
mud water	79.03	79.03
mud total	96.97	128.00
NP solid	10.13	16.80
NP sol. water	23.20	23.20
NP sol. total	33.33	40.00
Total Solid %	21.5%	39.1%
NP %	7.8%	10.0%

Test 6.15 was performed to observe the response of Mud C in contact with GOM shale. Table 6.22 shows the test conditions. As seen in Figure 6.20, the bottom pressure stabilized at 100 psi differential pressure in 27 hours. Using the transient method discussed in Chapter 4 the permeability of the sample was determined to be 0.0203 nd.

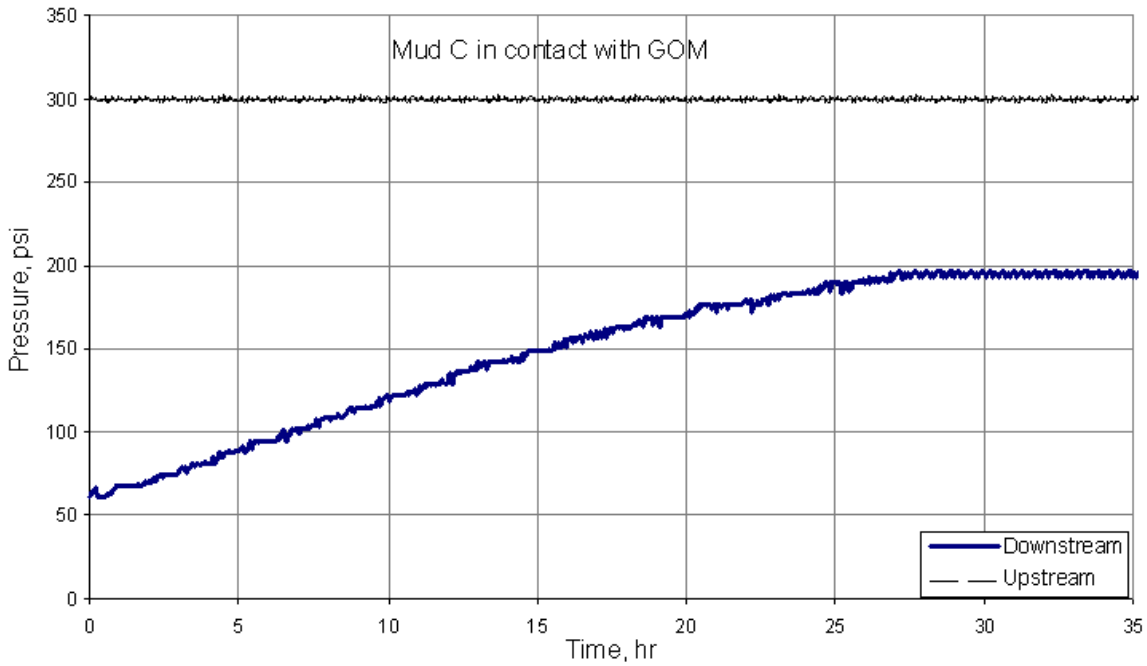

Figure 6.20: Results of Test 6.13 that was performed in contact with GOM shale.

Table 6.22: Conditions for Test 6.13.

Test	6.13
Date	12/25/2008
Shale	GOM
Top Fluid	Mud C
NP wt%	0
Bottom Fluid	Brine
Aw top	0.98
Aw Bottom	0.98
Aw shale	0.98
Top Pres. (Psi)	300
Bottom Pres. (Psi)	50
Result	Stabilized at 100 psi differential pressure in 27 hours with a permeability of 0.0203 nd.

Test 6.14 was performed to observe the effect of NP's on the response of Mud C in contact with GOM shale. Table 6.23 shows the test conditions and Table 6.24 shows the mud composition. As seen in Figure 6.21, the bottom pressure stabilized at 120 psi differential pressure in 35 hours. As shown in Figure 6.22, adding CSN-4 dispersion to the Field Mud C reduced the fluid penetration by 20 % in 36 hours. Using the transient method discussed in Chapter 4 the permeability of the sample was determined to be 0.0126 nd.

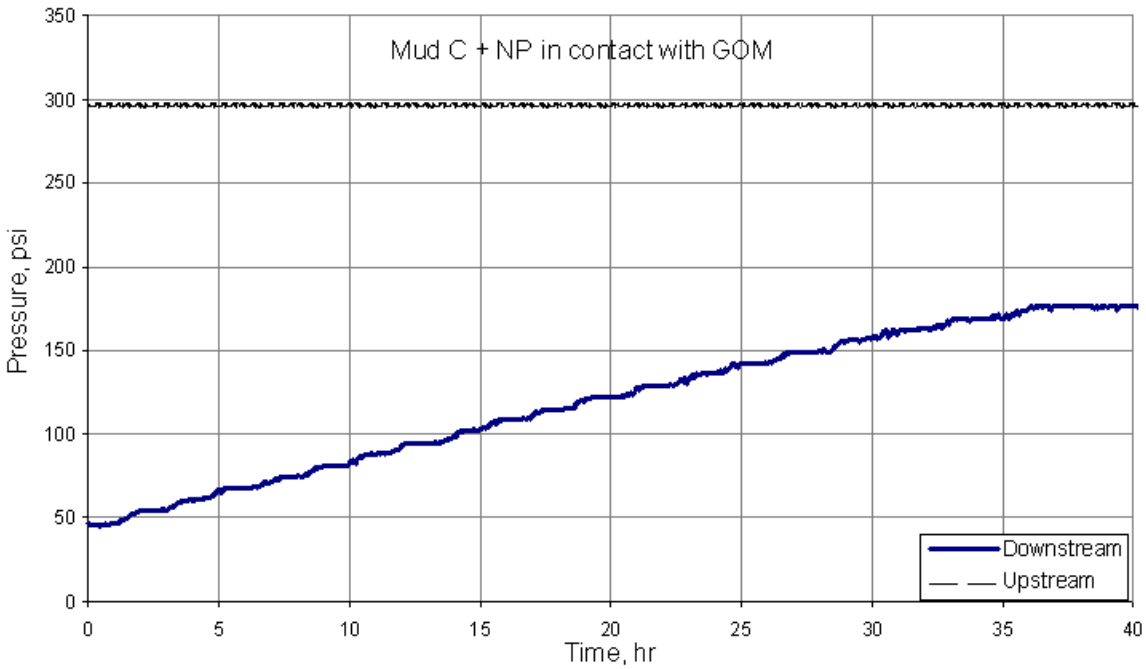

Figure 6.21: Results of Test 6.14 that was performed in contact with GOM shale.

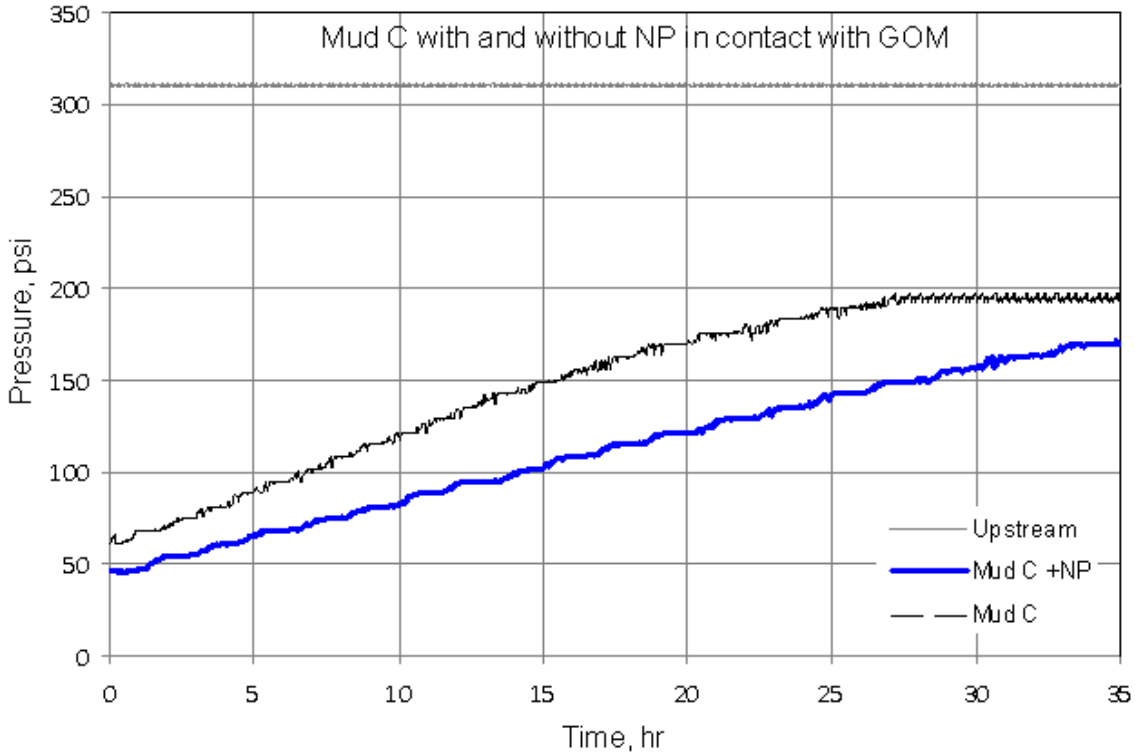

Figure 6.22: Comparison of Mud C with and without NP in contact with GOM shale.

Table 6.23: Conditions for Test 6.14.

Test	6.14
Date	12/25/2008
Shale	GOM
NP type	CSN-4
Top Fluid	Mud C + NP
NP wt%	10
NP Size (nm)	20
Bottom Fluid	Brine
Aw top	0.98
Aw Bottom	0.98
Aw shale	0.98
Top Pres. (Psi)	295
Bottom Pres. (Psi)	50
Result	Stabilized at 120 psi differential pressure in 36 hours with a permeability of 0.0126 nd.

Table 6.24: Mud composition in Test 6.14

Mud C+ CSN-4	Volume, cc	Mass, gr
Mud solid	21.14	34.86
mud water	93.14	93.14
mud total	114.29	128.00
NP solid	10.13	16.80
NP sol. water	23.20	23.20
NP sol. total	33.33	40.00
Total Solid %	21.2%	30.7%
NP %	6.9%	10.0%

Test 6.15 was performed to observe the response of Mud D in contact with GOM shale. Table 6.25 shows the test conditions. As seen in Figure 6.23, bottom pressure kept the differential pressure at 150 psi for 35 hours. Using the transient method discussed in Chapter 4 the permeability of the sample was determined to be 0.0109 nd.

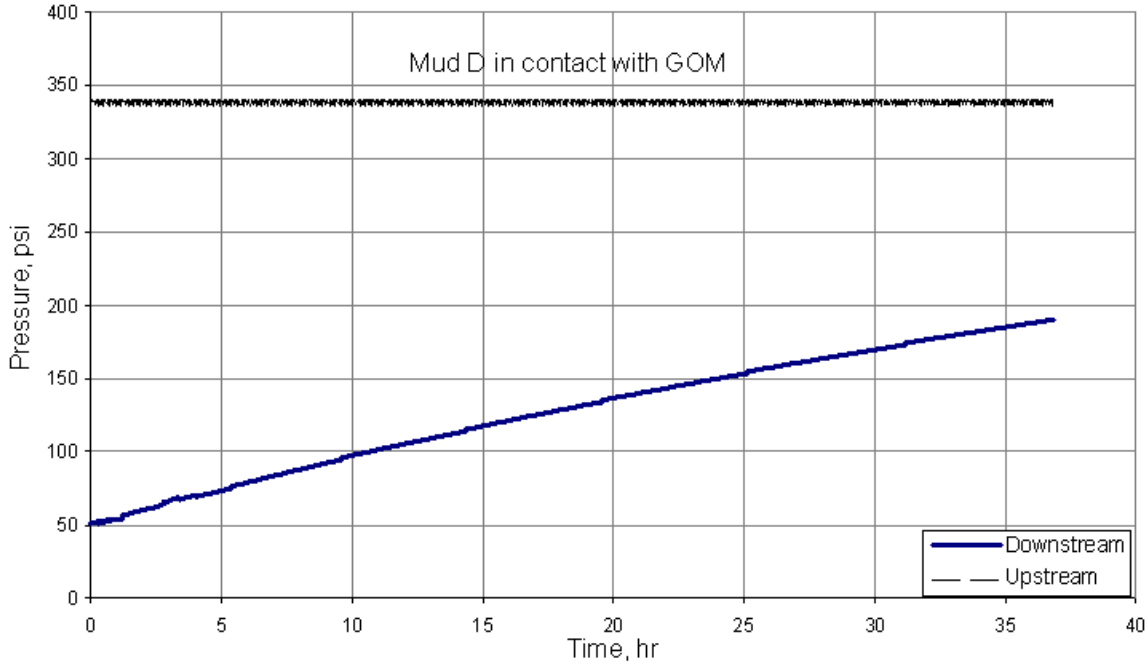

Figure 6.23: Results of Test 6.15 that was performed in contact with GOM shale.

Table 6.25: Conditions for Test 6.15.

Test	6.15
Date	12/27/2008
Shale	GOM
Top Fluid	Mud D
NP wt%	0
Bottom Fluid	Brine
Aw top	1
Aw Bottom	0.98
Aw shale	0.98
Top Pres. (Psi)	340
Bottom Pres. (Psi)	50
Result	Kept the differential pressure at 140 psi for 36 hours with a permeability of 0.0109 nd.

Test 6.18 was performed to observe the effect of NP's on the response of Mud D in contact with GOM shale. Table 6.26 shows the test conditions and Table 6.27 shows the mud composition used for the test. As seen in Figure 6.24, the bottom pressure stabilized at 170 psi differential pressure in 36 hours. As shown in Figure 6.25, adding CSN-4 dispersion to the Field Mud D reduced the fluid penetration by 17 % in 36 hours. Using the transient method discussed in Chapter 4 the permeability of the sample was determined to be 0.007 nd.

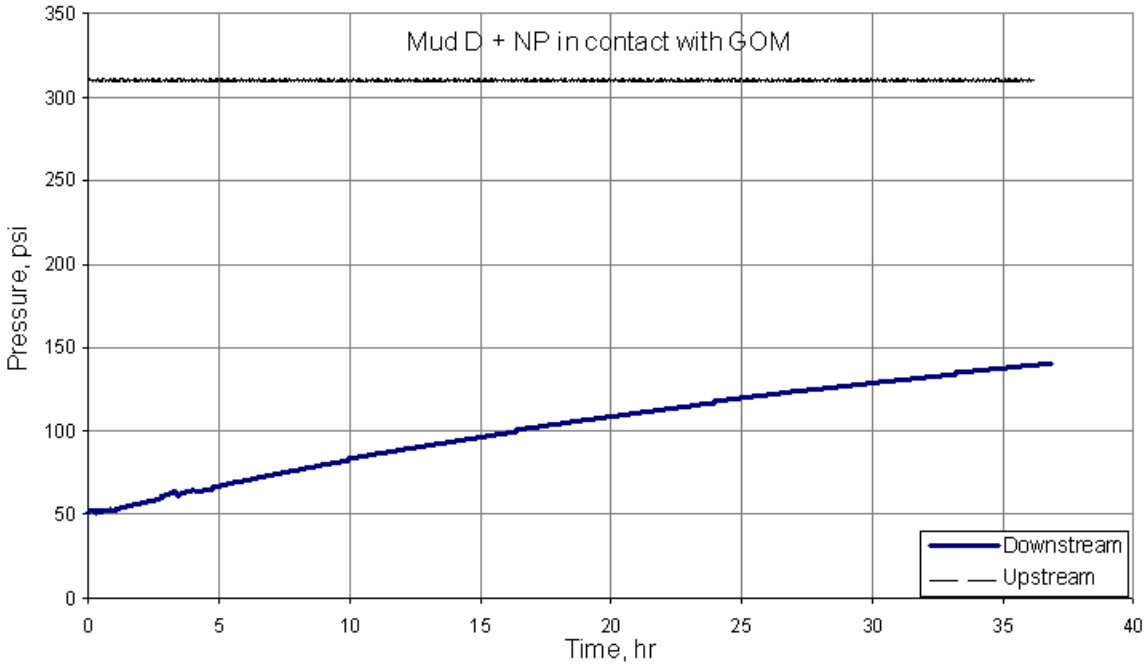

Figure 6.24: Results of Test 6.16 that was performed in contact with GOM shale.

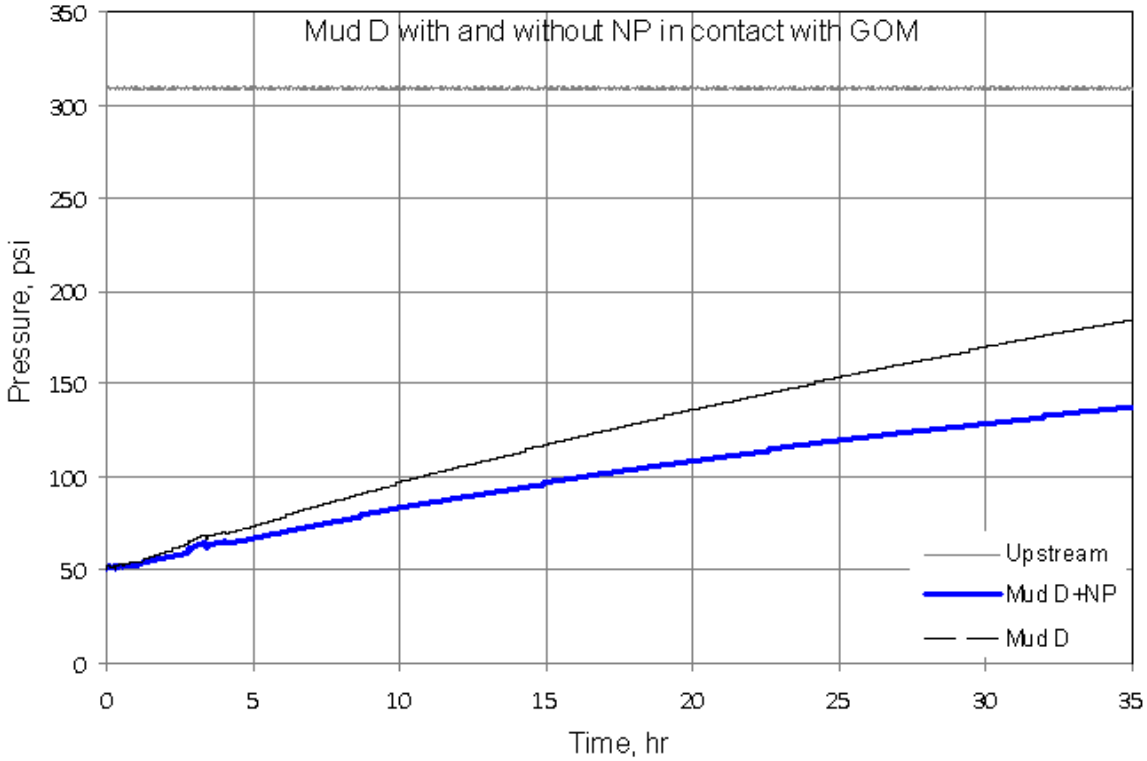

Figure 6.25: Comparison of Mud D with and without NP in contact with GOM shale.

Table 6.26: Conditions for Test 6.16.

Test	6.16
Date	12/29/2008
Shale	GOM
NP type	CSN-4
Top Fluid	Mud D + NP
NP wt%	10
NP Size (nm)	20
Bottom Fluid	Brine
Aw top	1
Aw Bottom	0.98
Aw shale	0.98
Top Pres. (Psi)	310
Bottom Pres. (Psi)	50
Result	Stabilized at 170 psi differential pressure in 36 hours with a permeability of 0.0070 nd.

Table 6.27: Composition in Test 6.16.

Mud D+ CSN-4	Volume, cc	Mass, gr
Mud solid	12.03	30.63
mud water	97.37	97.37
mud total	109.40	128.00
NP solid	10.13	16.80
NP sol. water	23.20	23.20
NP sol. total	33.33	40.00
Total Solid %	15.5%	28.2%
NP %	7.1%	10.0%

Test 6.17 was performed to observe the response brine in contact with GOM shale. Table 6.28 shows the test conditions. As seen in Figure 6.26, the bottom pressure built up to the top pressure in 5 hours. Using the transient method discussed in Chapter 4 the permeability of the sample was determined to be 0.6510 nd.

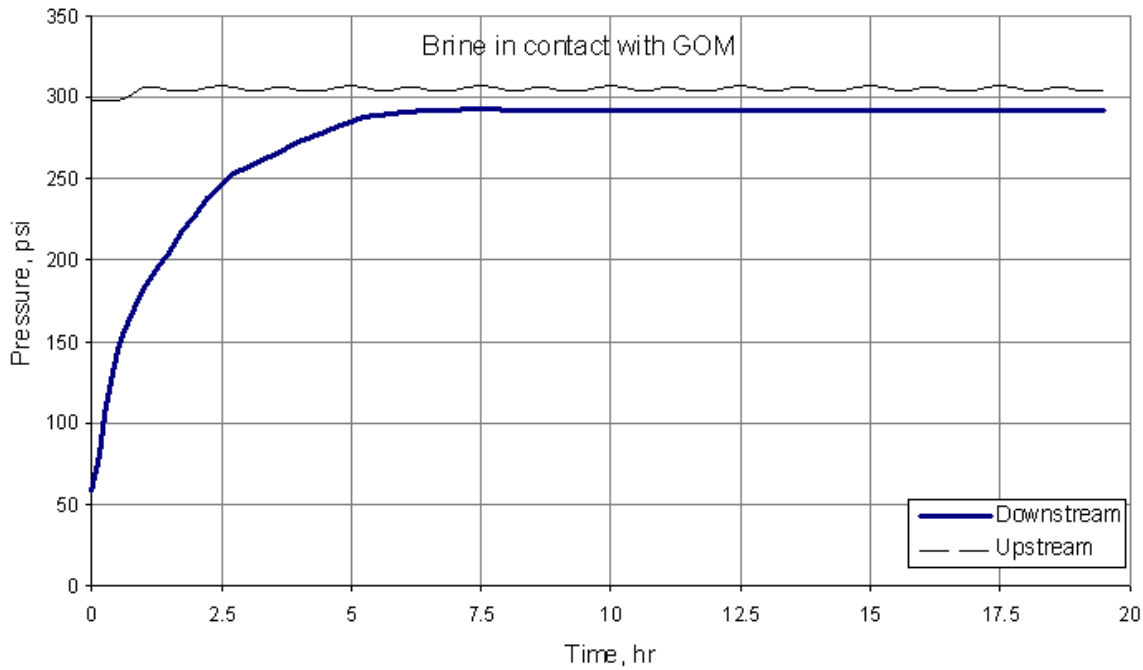

Figure 6.26: Results of Test 6.17 that was performed in contact with GOM shale.

Table 6.28: Conditions for Test 6.17

Test	6.17
Date	02/20/2009
Shale	GOM
Top Fluid	Brine
NP wt%	0
Bottom Fluid	Brine
Aw top	0.98
Aw Bottom	0.98
Aw shale	0.98
Top Pres. (Psi)	300
Bottom Pres. (Psi)	50
Result	Built up to the top pressure in 5 hours with a permeability of 0.6510 nd.

Permeability calculations for each field mud test were done to observe the effect of nanoparticles. As seen in Figure 6.27 and Table 6.29, Nanoparticle additions to the field muds reduced the permeability of GOM shale by factor of 2.76 for Field Mud A, 1.61 for Field Mud C and 1.55 for Field Mud D.

Table 6.29: Permeability values obtained with and without nanoparticles for GOM shale

Test	Rock	Fluid	Permeability (nd)
41	GOM	Brine	0.6510
30	GOM	Mud A	0.0380
31	GOM	Mud A Modified	0.0140
35	GOM	Mud B	0.0404
36	GOM	Mud B Modified	0.0408
37	GOM	Mud C	0.0203
38	GOM	Mud C Modified	0.0126
39	GOM	Mud D	0.0109
40	GOM	Mud D Modified	0.0070

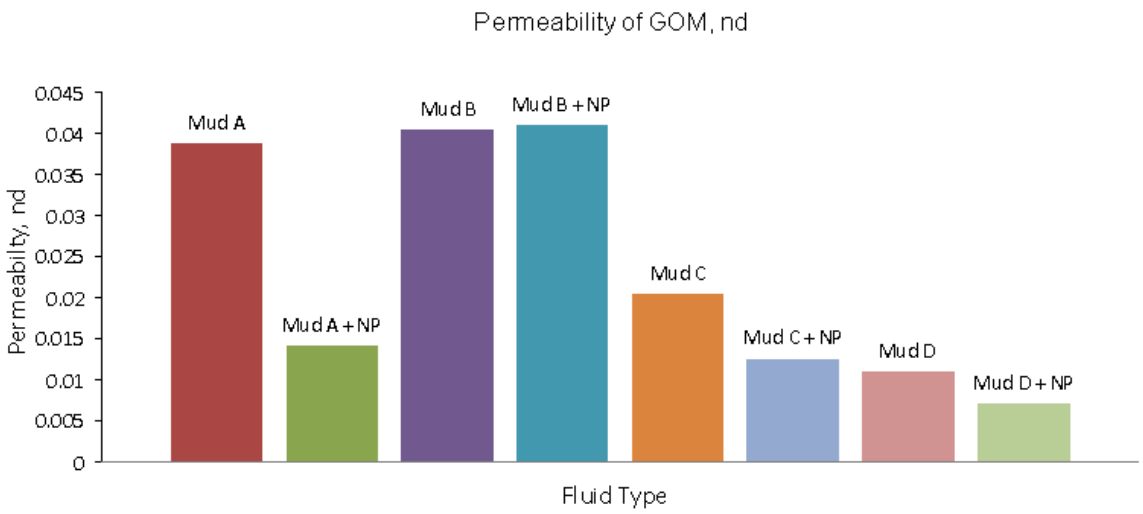

Figure 6.27: Permeability chart of GOM shale.

6.4 Conclusions

In this study, it was shown that:

1. The use of nanoparticles reduced the fluid penetration into the Atoka shale up to 98 % compared to sea water.
2. The addition of nanoparticles to field muds reduced the fluid penetration into the Atoka shale by 16 to 72 %.
3. The addition of nanoparticle to field muds reduced the fluid penetration into the GOM shale by 17 to 27 %.
4. A water - nanoparticle dispersion can reduce the permeability of Atoka shale to less than 0.001 nd.
6. The minimum nanoparticle concentration needed to satisfactorily reduce the permeability and fluid invasion is 10 wt %, it was much better than 5 wt%.

7. By increasing the salt concentration of the mud the effectiveness of nanoparticle additions to the mud is reduced.
8. The best shale sealing performance for the Atoka shale is obtained with 20 nm size compared to 5 nm nanoparticles.
9. Some nanoparticle dispersions are not stable for condition of high salt concentration and temperature conditions.

Chapter 7: High Performance Nanoparticle Water-based Drilling Fluids for Organic Rich Shales

Introduction

Drilling through a clay rich shale layer often results in borehole instability problems. It has been estimated that shale formations make up more than 75% of all drilled formations; they account for more than 90% of all expenses associated with wellbore instability problems. Among the various factors that produce instability problems, our study will focus on the pressure loss to shale by water invasion. Shale invaded by water raises a host of problems, including hole collapse and wellbore weakening. This is because the clay minerals inside the shale interact with water in the drilling fluid. To prevent water from contacting the shale, oil-based muds (OBMs) are traditionally preferred. OBMs have good wellbore stability and lubricity properties since they do not interact with shales. OBMs are also preferred for their capillary sealing of the shale surface. OBMs, however, are expensive and are subject to environmental constraints. Because of this, water-based muds (WBMs) are often preferred.

To use WBMs in shale reservoirs, several issues need to be resolved. For one thing, WBMs can interact more easily than OBMs with the shale pore fluid. This interaction can potentially lead to loss of pore pressure support. To reduce the pressure loss, internal or external mud filter cakes must form. Shales have extremely low permeability and small pore throat size, so normal drilling fluids fail to form such impermeable internal or external mud cakes and thus fail to stop fluid invasion. The industry uses several guidelines to choose the particle size and distribution of bridging materials that can form effective internal and external mud cakes and minimize formation damage. Suri and Sharma (2004) showed that to form bridges, the particle size should be less than the pore throat size. As shown earlier in our lab, Al-Bazali et al. (2006) and Oleas et al. (2008), a variety of shales have an average pore throat size ranging from 10 to 30 nanometers. Comparatively, bentonite and barite, two commonly used drilling fluid additives, have much larger particle diameters, in the range of 0.1 to 100 microns. This particle size is too large to penetrate the shale pores or form a filter cake that will significantly impede the flow of water into the shale. To plug shale pores particle sizes need to be less than 30nm.

In past chapters in this report subsequently published recent studies, Sensoy et al. (2009) and Cai et al. (2012) showed that nano- particles (particle diameters in the nanometer range) can plug several types of shale, preventing water from flowing into the shale formation. They demonstrated that nanoparticles performed well at plugging the pore throats of Atoka and Gulf of Mexico (GOM) shales, significantly reducing the permeability of the shale and minimizing fluid invasion. Despite their positive results, their results are limited since they tested only shale samples which do not contain organic material such as bitumen, oil and gas.

In this chapter, we test Texas gas shale samples which contain organic material, and our testing fluids are 4% NaCl brine, base mud, and a water-based mud containing nano-particles (Nano mud). To determine the proper size of nanoparticles to be used in the mud, we investigated the pore throat size of Texas gas shale with dual beam SEM/FIB machine. The original surface of the shale is too rough, so it is impossible to observe in-situ shale structure and its pore throats. After we mill the surface with an ion beam, we can see the in-situ structure and its pore throat size, and the pore throat is measured to be in the 20-30nm size range (Figure 1). If

nanoparticles perfectly plug these pore throats, the shale effectively acts as if it is impermeable to brine, minimizing shale swelling and other osmotic phenomena.

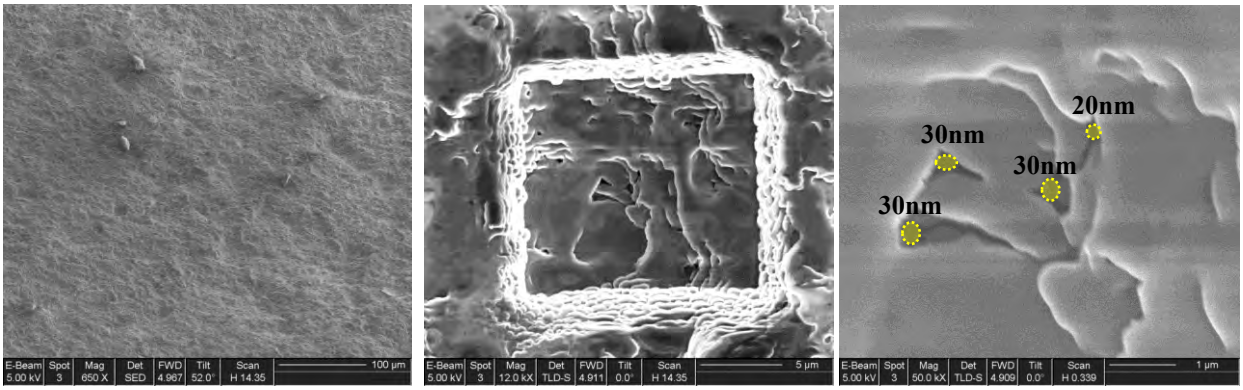

Figure 7.1: SEM image of Texas gas shale: (a) original surface, (b) ion-milled surface with dual beam SEM/FIB, and (c) pore throat size of shale

7.1 The Properties of water-base mud

Our water base mud was obtained from M-I Swaco, and its properties are given in the paper by Ji et al (2012). The nanoparticle concentration and rheology data of each of the Nano-muds are listed in Table 7.1.

Table 7.1: Mud properties (Ji et al., 2012)

Contents	Unit	Base Mud	10ppb Nano Mud	30ppb Nano Mud
Nanoparticle solution	%	0	3%	10%
Density	lb/gal	11.99	11.86	11.95
10-sec gel strength	$lb/100ft^2$	7	6	5
10-min gel strength	$lb/100ft^2$	10	8	7
Plastic viscosity	cP	19	28	28
Yield point	$lb/100ft^2$	36	18	12
pH		9.65	8.7	9

7.2 Permeability measurement results

We tested three Texas gas shale samples with brine, base mud, and nano-muds. The test results and conditions are listed in Table 7.2. The first sample was tested with brine and base mud. With 4% sodium chloride brine, the permeability is 22,624nD which is on the 10μD range. After that, we tested the same sample with the base mud, and the permeability is reduced to 22nD. To see the durability of this permeability reduction, we ran one more test with brine again.

The permeability remained unchanged at 28nD. A second shale sample was tested with brine and 30ppb nano-mud. The permeability with brine was measured to be 15,097nD which is on the 10μD range (similar to the first sample). However, the permeability with 30ppb nano-mud is reduced to 0.28nD. This means that the nano-mud almost completely shut-off the pressure transmission through the sample.

The third sample was tested with brine and 10ppb nano-mud. In this test, we wanted to investigate what concentration of nanoparticle solution is needed to reduce the permeability. The permeability with brine was measured to be 15,097nD, and it was reduced to 0.28nD with the nano-mud. It means that 10ppb of nano-particles in the mud is enough to prevent water invasion into the shale. After the nano-mud test, we ran one more brine permeability test, and the permeability was found to increase to 5.55nD but it was still lower than the initial permeability.

Table 7.2: Permeability results for Texas Gas Shale

Sample	Testing Fluid	Permeability (nD)	Test condition	Test time
TGS#1	4% NaCl Brine	22,624	Upstream pressure: 300psi Downstream pressure: 50psi Pressure differential: 250psi	2 minutes
	Base Mud	22	Upstream pressure: 300psi Downstream pressure: 50psi Pressure differential: 250psi	15 hours
	4% NaCl Brine	28	Upstream pressure: 300psi Downstream pressure: 50psi Pressure differential: 250psi	18 hours
TGS#2	4% NaCl Brine	15,097	Upstream pressure: 300psi Downstream pressure: 50psi Pressure differential: 250psi	3 minutes
	30ppb Nano-Mud	0.28	Upstream pressure: 300psi Downstream pressure: 50psi Pressure differential: 250psi	35 hours
TGS#3	4% NaCl Brine	19,810	Upstream pressure: 300psi Downstream pressure: 50psi Pressure differential: 250psi	2 minutes
	10ppb Nano-Mud	0.42	Upstream pressure: 300psi Downstream pressure: 50psi Pressure differential: 250psi	23 hours
	4% NaCl Brine	5.55	Upstream pressure: 300psi Downstream pressure: 50psi Pressure differential: 250psi	25 hours

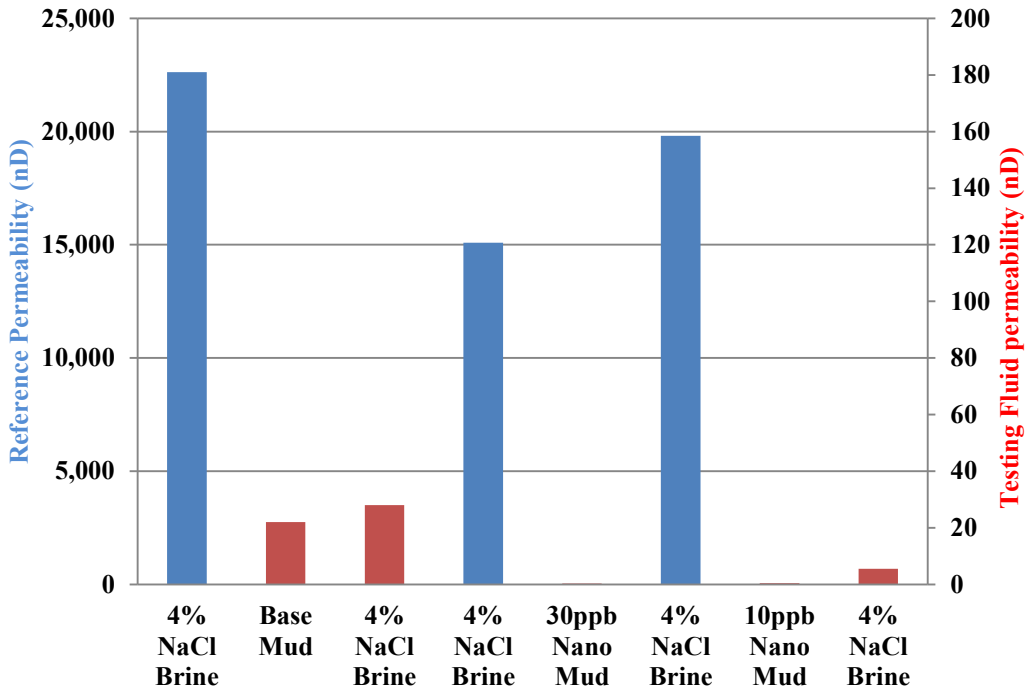

Figure 7.2: Permeability reduction result chart

Conclusions

Based on the above test results, the following conclusions are drawn.

- With properly designed water-based muds containing nanoparticles, water invasion into shales is reduced by orders of magnitude.
- The physical plugging by nanoparticles is durable, since the brine test after the nano-mud test still shows very low permeability compared with the original brine permeability.
- Base mud which does not contain nanoparticles also reduces the permeability of shales, but the permeability reduction is less than with the nano-mud.
- The addition of nano-particles to a water-based mud has the potential to significantly reduce water invasion into a shale and thereby reduce wellbore instability problems.
- It may be possible to drill shale wells (vertical and horizontal) with water-based muds which have lower costs and a smaller environmental footprint.

References

Abrams, A. 1977. Mud Design to Minimize Rock Impairment due to Particle Invasion. *Journal of Petroleum Technology* 29(5): 586-592.

Al-Bazali, T.M., Zhang, J., Chenevert, M.E., and Sharma, M.M. 2006. Factors Controlling the Membrane Efficiency of Shales When Interacting with Water-Based and Oil-Based Muds,

SPE 100735 presented at the International Oil & Gas Conference and Exhibition in Beijing, China, December 5 – 7.

Cai, J., Chenevert, M.E., Sharma, M.M., and Friedheim, J. 2012. Decreasing Water Invasion Into Atoka Shale Using Nonmodified Silica Nanoparticles, SPE Drilling & Compl **27** (1): 103-112. SPE-146979-PA, http://dx.doi.org/10.2118/146979-PA.

Ji, L., Guo Q., Friedheim, J., Zhang, R., Chenevert, M., and Sharma M. 2012. Laboratory Evaluation and Analysis of Physical Shale Inhibition of an Innovative Water-Based Drilling Fluid with Nanoparticles for Drilling Unconventional Shales, SPE-158895 presented at SPE Asia Pacific Oil and Gas Conference and Exhibition in Perth, Australia, 22-24 October. http://dx.doi.org/10.2118/158895-MS

Manohar, L. 1999. Shale Stability: Drilling Fluid Interaction and Shale Strength, SPE 54356 SPE Asia Pacific Oil and Gas Conference and Exhibition in Jakarta, Indonesia, April 20 – 22.

Oleas, A., Osuji, C., Chenevert, M., and Sharma, M. 2008. Entrance Pressure of Oil Based Mud Into Shale: Effect of Shale Water Activity and Mud Properties, paper SPE 116364 presented at SPE Annual Technical Conference and Exhibition in Denver, Colorado, September 21 – 24.

Sensoy, T., Chenevert, M.E., and Sharma M. M. 2009. Minimizing Water Invasion in Shales Using Nanoparticles, paper SPE 124429 presented at SPE Annual Technical Conference and Exhibition in New Orleans, Louisiana, October 4 – 7. DOI: 10.2118/124429-MS.

Simpson, J.P. 1979. A New Approach to Oil-Base Muds for Lower-Cost Drilling. J. Pet Tech 31 (5): 643–650. SPE-7500-PA. doi: 10.2118/7500-PA.

Steiger, R.P. and Leung, P. K. 1992. Quantitative Determination of the Mechanical Properties of Shales. SPE Drilling Engineering, 7(3): 181-185. SPE 18024-PA. DOI: 10.2118/18024-PA.

Suri, A., Sharma, M.M. 2004. Strategies for Sizing Particles in Drilling and Completion Fluid, SPE Journal, 9 (01): 13 – 23.

Chapter 8: A New Standardized Protocol for Evaluating the Interaction of Drilling and Fracturing Fluids with Hydrocarbon Bearing Shales

Introduction

The two major concerns during drilling and completion of wellbores in unconventional reservoirs are: wellbore instability and proppant embedment. Both of these issues are controlled by the interaction of water-based fluids with the organic-rich shale. Understanding the interaction of water-based fluids with organic-rich shales is the first step towards developing screening tests for their compatibility with the shale. In this chapter, we present a systematic approach to investigate the interaction of water-based drilling and fracturing fluids with organic-rich shales.

We performed a series of measurements to determine shale mineralogy, native water activity, swelling parallel and perpendicular to bedding planes, Brinell hardness, P-wave and S-wave velocities. Changes in hardness and acoustic wave velocities were measured before and after shale samples came into contact with water-based fluids. Shale swelling was determined in two directions simultaneously with our unique 2-D strain indicators. The dynamic Young's modulus and Poisson's ratio were calculated based on the wave velocities. It is shown that these measurements can be used to screen drilling and completion fluids that may interact unfavorably with the shale.

The shale mineralogy was obtained using XRD. The shale native water activity was determined with controlled humidity environments. Multi-scale durometers were used to measure the shale hardness. Anisotropic swelling was observed for all shale samples characterized. The results showed a good correlation with the mineralogy, hardness and wave velocities of the shale. In general, the water adsorption was greater with fresh water than with 4% NaCl and 2% KCl. Changes in hardness, P-wave and S-wave velocities, dynamic Young's modulus and Poisson's ratio after shale's contact with water-based fluids can be used as indicators for wellbore stability and fracture conductivity impairment in these shales.

The measurement techniques and procedures presented in this chapter can be used as standard screening tests to evaluate the interaction between organic-rich shales and water-based drilling and fracturing fluids. If this testing protocol shows incompatibility of the fluids with the shale, additional fracture conductivity tests should be conducted. The screening protocol presented here minimizes the number of fracture conductivity measurements (that are hard to perform) that need to be conducted to check for shale-fluid compatibility.

8.1 Introduction

Recent technological advances in horizontal drilling and hydraulic fracturing have propelled shale gas and oil productions to record highs. These technologies are able to increase the area of contact with shale reservoirs by several orders of magnitude, making production from these previously inaccessible formations more economic.

Both drilling and hydraulic fracturing require the use of a large amount of fluids, especially water. The water consumption in drilling a horizontal well in shale formations is

typically between 500,000 and one million gallons, while 2 to 4 million gallons of water is usually pumped to fracture a horizontal well (Ground Water Protection Council and ALL Consulting, 2009). The presence of clay minerals can often result in shales being very reactive with water-based fluids (Sharma, 2004). Moisture can be adsorbed by the clay within the shale and weaken the bonding between clay layers. Consequently, shales can swell and soften after coming into contact with water-based fluids. This weakening of shale strength can lead to a variety of associated problems in drilling and completion practices. The water sensitivity of a shale can cause wellbore instability problems such as wellbore collapse. These instability issues have cost the industry significant rig time. Although such problems can be mitigated by using oil-based or synthetic-based fluids, there can be additional costs and environmental concerns. Likewise, proppant embedment in fractures can result in the closure of hydraulically created fractures, thus reducing fracture conductivity, which in turn will negatively impact productivity. The selection of suitable drilling and fracturing fluids is, therefore, critical in successfully developing shale reservoirs.

To screen fracturing fluids, conducting fracture conductivity experiments is the most direct way to test for fluid compatibility since these experiments directly measure the fracture permeability reduction when shales are in contact with water-based fluids. However, such experiments take a lot of time to run and are difficult to perform. A more systematic protocol to evaluate changes in shale mechanical properties when in contact with water-based fluids can simplify the experimental procedure and yet provide useful information regarding changes in fracture conductivity. A lot of the past experience from characterizing non-organic bearing shales can be valuable for studying the interaction of organic-rich shales with water-based fluids. Chenevert and Amandullah (2001) demonstrated a shale's inability to regain its original hydration state when that is altered. They suggested an oil immersion method to process and preserve the North Sea shale. Shale mineral composition was determined using X-ray diffraction (XRD) (Breeden and Shipman, 2004). Saturated salt solutions were used to create controlled humidity environments for shale native water activity measurements (Chenevert, 1970). Zhang et al. (2006) evaluated the changes in shale compressive strength and acoustic wave velocities after they were exposed to water-based fluids containing different salts. A combined gravimetric-swelling test was used to measure the water and ion uptake when shale was exposed to water-based fluids (Zhang et al, 2004). Tutuncu and Mese (2011) employed a load/displacement relationship to quantify shale Brinell hardness. Collectively, the shale petrophysical and mechanical properties determined with these testing procedures can provide very useful information for screening fracturing and drilling fluids for shale reservoirs.

In this chapter, we present a screening procedure to study the interaction of organic-rich shale with drilling and fracturing fluids. Use of this procedure allows many fluids to be tested rapidly without the need to conduct fracture conductivity experiments with a large number of fluids. The techniques and procedures in this protocol can be used to screen and evaluate the compatibility of shale with any water-based fluid.

8.2 Experimental Procedures

The experimental set-up, procedures and shale sample handling and preparation protocols have been outlined in Chapter 2. One of the most important aspects of core analysis with shales

is the careful preservation of shale samples. Data from unpreserved shales are not representative of original shale properties in the subsurface. This is because when shales are exposed to the air, their mechanical and flow properties change irreversibly. Water will enter or leave shale samples, depending on their hydration state relative to the humidity of the surrounding atmosphere. It is imperative that preserved samples be used for all shale characterization work. Therefore, it is critical to handle and preserve shale samples with great care both in the field and in the laboratory so that data measured using these samples will be valid. The impact of shale preservation on petrophysical properties will be described in Chapter 9.

The measurements that we perform to test the compatibility of drilling and fracturing fluids with shales include mineralogy, native water activity, swelling parallel and perpendicular to bedding planes, Brinell hardness, P-wave and S-wave velocities. The changes in mechanical properties of shales upon contact with water-based fluids will provide useful information regarding the selection of compatible fluids for drilling and fracturing.

8.3 Results and Discussion

The mineralogy and native water activities of Texas Gas Shale (TGS), Eagle Ford Shale (WGS), Barnett Shale and Gulf of Mexico Shale (GOM) were presented in Chapter 2. Changes in mechanical properties will be the focus of this section.

8.3.1 Shale Swelling

Figure 8.1 shows the swelling behavior of TGS perpendicular and parallel to bedding planes with fresh water, 4% NaCl and 2% KCl. Anisotropic swelling was observed with all three fluids. TGS expanded perpendicular to bedding planes and shrank parallel to bedding planes after 24 hours of immersion. In fact, this anisotropic swelling behavior was observed for all other organic-rich shales that we tested. In the direction perpendicular to bedding planes, we can see that fresh water caused the most expansion, followed by 4% NaCl and 2% KCl solutions. This is consistent with the weight change observed with these three fluids shown in Figure 8.2. It is clear that TGS is only slightly water sensitive. As expected, fresh water resulted in the most weight gain, followed by 4% NaCl and 2% KCl solutions. The greater weight gain with 4% NaCl than with 2% KCl was due to the hydrated radius of sodium (7.9 Å) being larger than that of potassium (5.32 Å). As a result, a greater amount of water entered TGS after it was exposed to 4% NaCl solution.

The earlier expansion parallel to bedding planes with 2% KCl might be due to the concentration difference of K^+ ions in the native shale and in the bulk solution. The concentration difference resulted in the sudden influx of K^+ ions into the shale when it was brought into contact with 2% KCl solution.

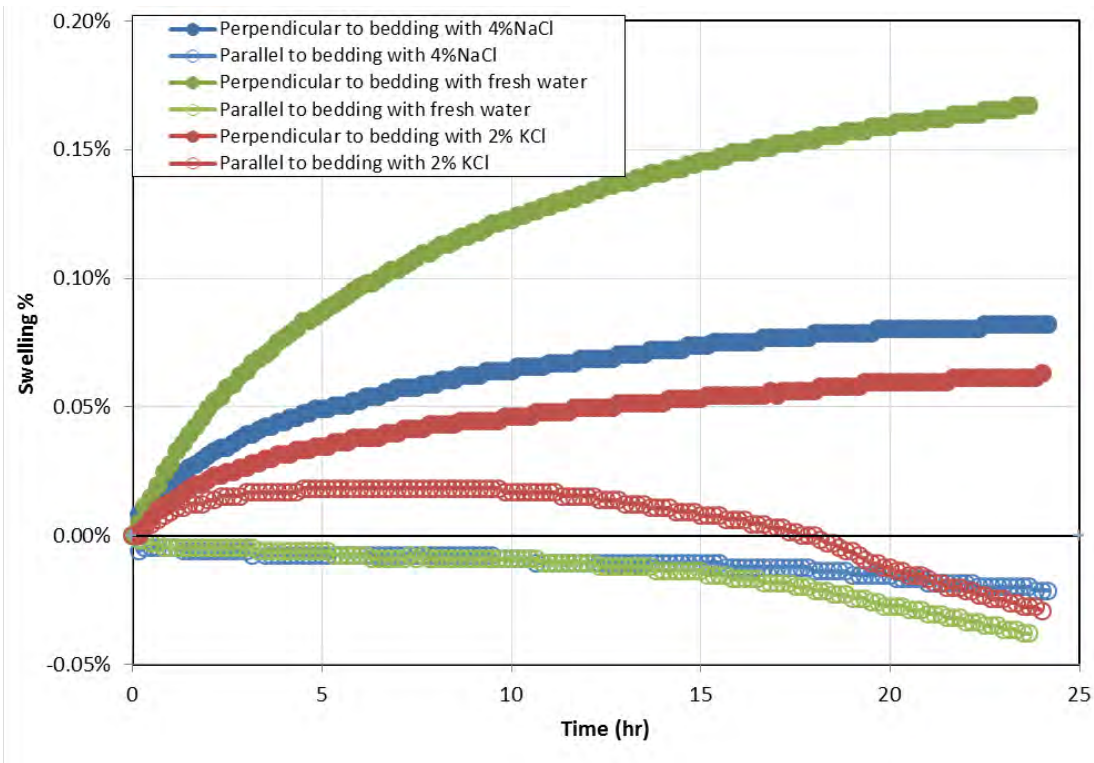

Figure 8.1: Swelling of TGS after exposed to fresh water, 4% NaCl and 2% KCl for 24 hours.

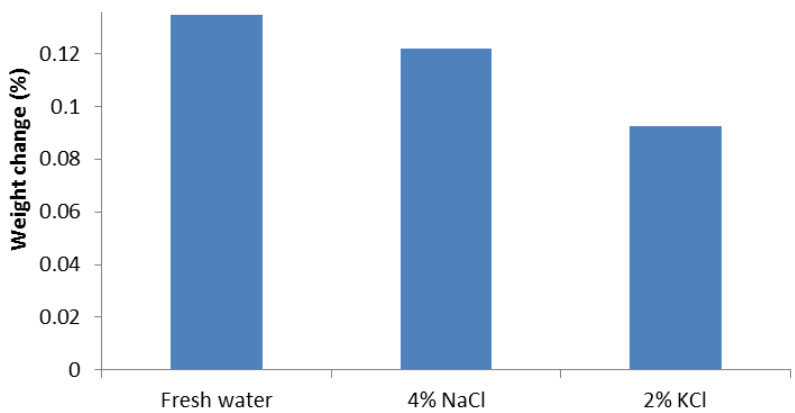

Figure 8.2: Weight change of TGS after exposed to fresh water, 4% NaCl and 2% KCl for 24 hours.

Figure 8.3 shows the swelling behavior of WGS perpendicular and parallel to bedding planes with these water-based fluids. Similar to the swelling behavior of TGS shown in Fig 8.1, WGS also exhibited anisotropic swelling. It expanded perpendicular to bedding planes while shrinking parallel to bedding planes. The degree of expansion perpendicular to bedding planes for both shales is consistent with the weight change after exposure to these fluids shown in Fig 8.4. The early expansion of WGS parallel to bedding planes with 4% NaCl and 2% KCl might be due to the difference in ionic concentration, which resulted in the influx of Na^+ and K^+ during the first 5 hours of the swelling test.

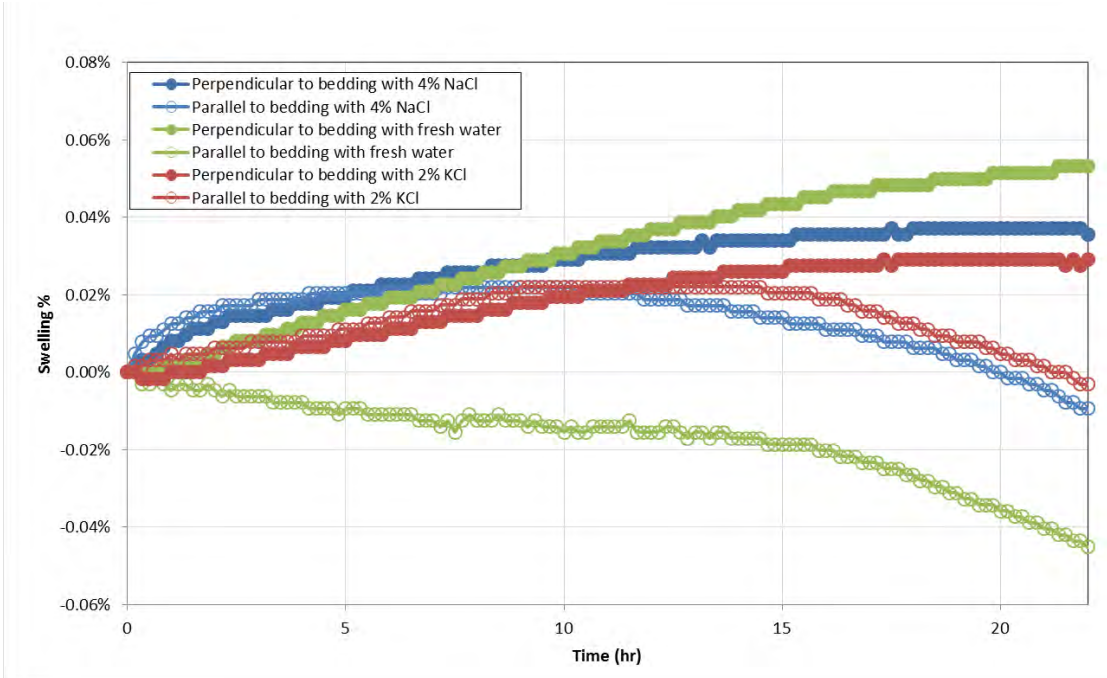

Figure 8.3: Swelling of WGS after exposed to fresh water, 4% NaCl and 2% KCl for 24 hours.

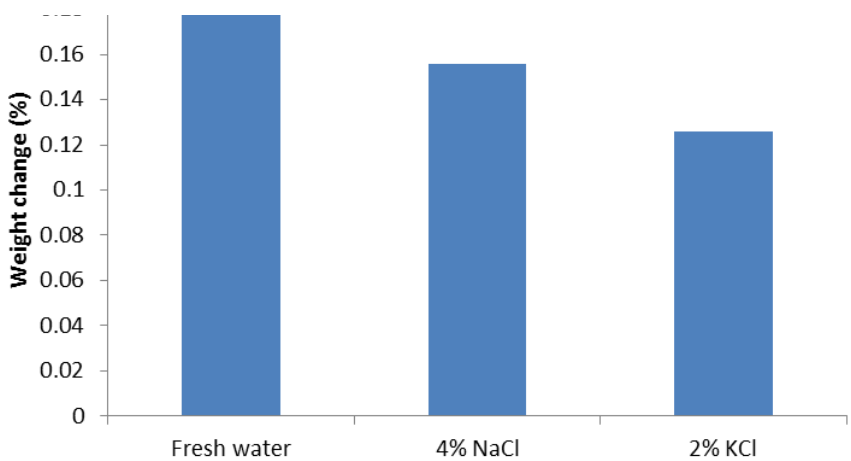

Figure 8.4: Weight change of WGS after exposed to fresh water, 4% NaCl and 2% KCl for 24 hours.

We can see from Figure 8.2 and Figure 8.4 that WGS had a greater weight gain with the three fluids than TGS. This can be due to the fact that WGS contains more clay than TGS (The clay content of WGS is 26% and that of TGS is 19%). Clay is the main mineral that contributes to the water uptake for shales. One other possible reason is because the WGS has a lower native water activity than TGS. Water tends to go into the shale with a lower native water activity.

Figure 8.5 shows the swelling behavior of Barnett shale exposed to fresh water and 4% seawater. The sea salt contains mostly NaCl. We can also see that the degree of expansion perpendicular to bedding was greater with fresh water in the first three hours of the test. After that, the degree of expansion was greater with 4% seawater, which reached the same degree of

expansion at approximately the14th hour. The higher salt concentration can explain the initial higher degree of expansion in the axial direction with 4% seawater. However, due to the existence of multiple cracks in the Barnett shale samples, definitive conclusions cannot be reached to describe the degree of expansion in the direction perpendicular to bedding and the degree of shrinkage in the direction parallel to bedding. Again, the weight change of the Barnett shale after exposed to fresh water and 4% seawater shown in Figure 8.6 is consistent with the swelling behavior in Figure 8.5. Fresh water resulted in more swelling than the 4% sea water for the Barnett shale.

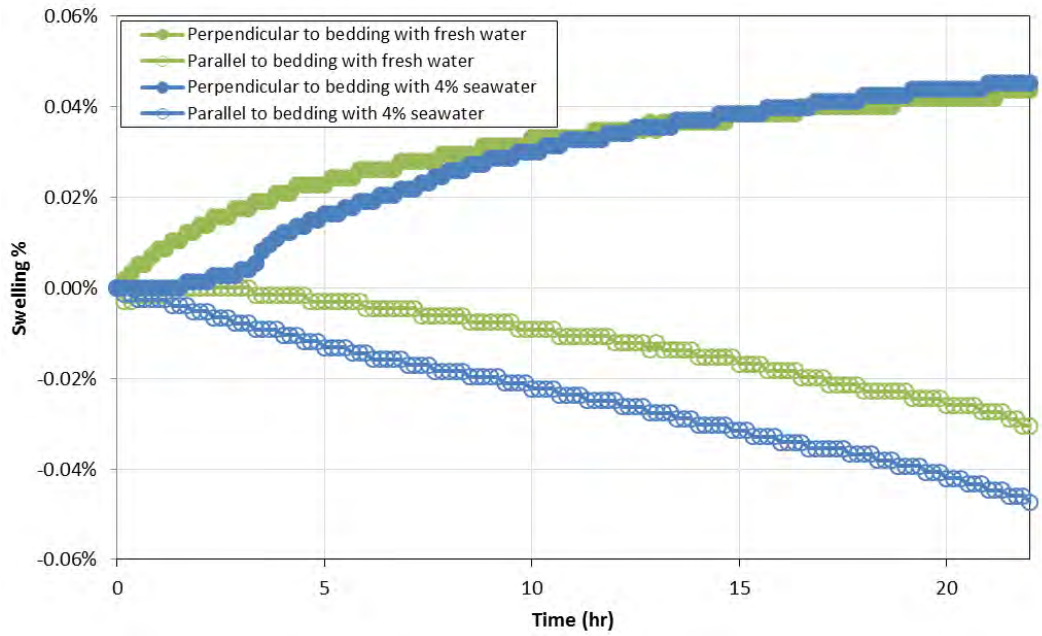

Figure 8.5: Swelling of Barnett shale after exposed to fresh water and 4% seawater for 24 hours.

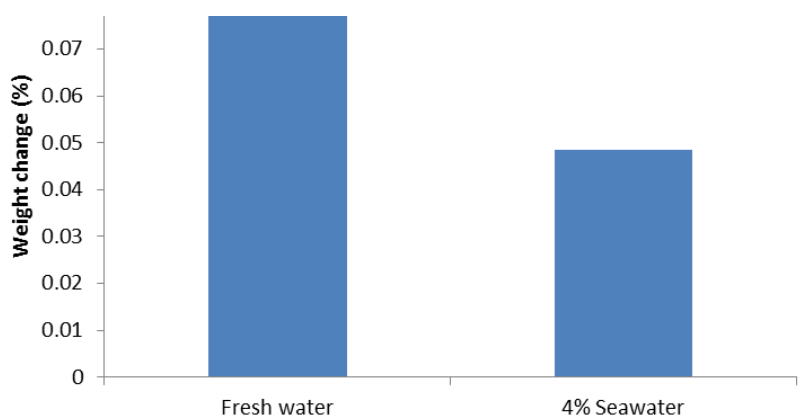

Figure 8.6 : Weight change of Barnett shale after exposed to fresh water and 4% seawater for 24 hours.

Attempts were made to measure the swelling behavior of the Gulf of Mexico shale (GOM). However, the sample disintegrated upon contact with water-based fluids and no swelling data was obtained.

8.3.2 Brinell hardness

Figure 8.7 – 8.9 show the change in Brinell hardness after TGS and WGS samples were exposed to fresh water, 4% NaCl and 2% KCl and after Barnett shale was exposed to fresh water and 4% seawater for 24 hours. HBS 10/3000 means that the hardness is measured with a 10 mm diameter steel ball using a 3000 kg force. The hardness was obtained from the durometer reading. In general, there was a small decrease in hardness after shales were immersed in these fluids. The small increase in Brinell hardness parallel to bedding after TGS was immersed in fresh water was within experimental error. Similar to the weight change, we can conclude from the change in Brinell hardness that TGS, WGS and the Barnett shale were only slightly water sensitive.

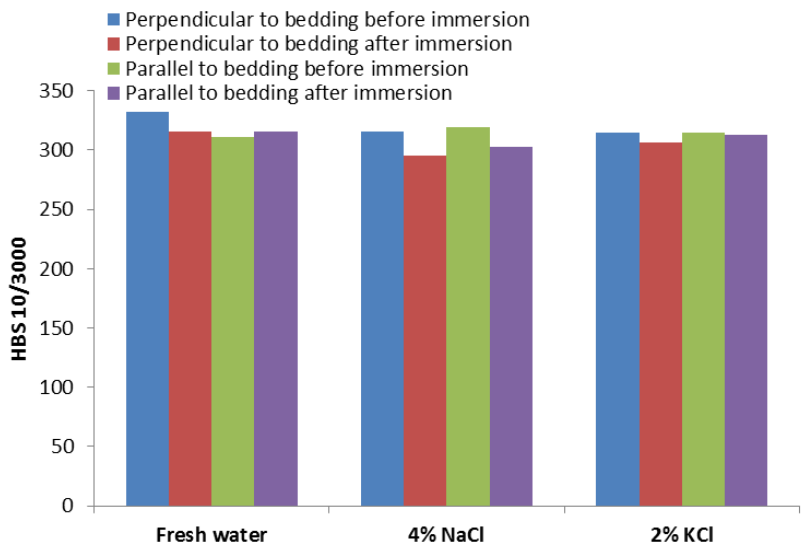

Figure 8.7: Brinell hardness of TGS after exposed to fresh water, 4% NaCl and 2% KCl for 24 hours.

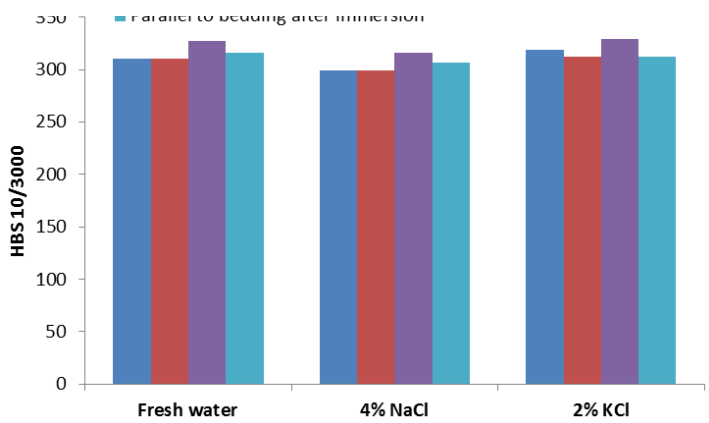

Figure 8.8: Brinell hardness of WGS after exposed to fresh water, 4% NaCl and 2% KCl for 24 hours.

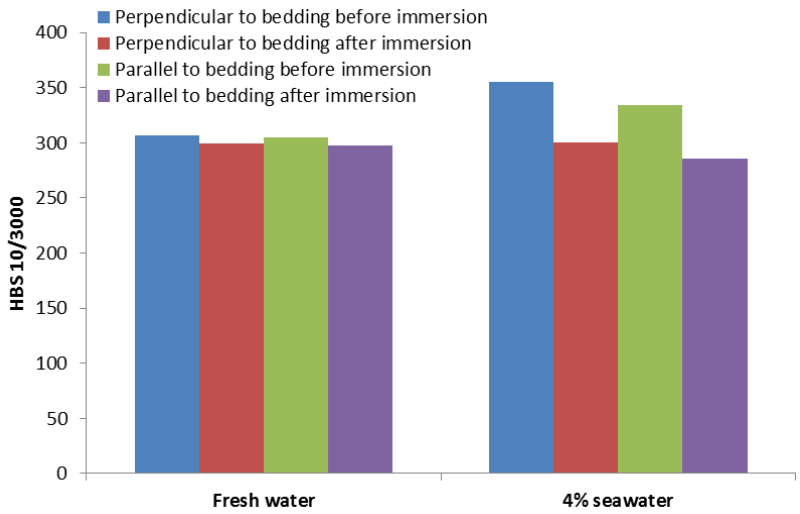

Figure 8.9: Brinell hardness of Barnett shale after exposed to fresh water and 4% seawater for 24 hours.

8.3.3 Acoustic wave velocity

Figure 8.10 – 8.12 show the change in acoustic wave velocities after TGS and WGS samples were exposed to fresh water, 4% NaCl and 2% KCl and after Barnett shale was exposed to fresh water and 4% seawater for 24 hours. In general, the wave velocities decreased after shale was in contact with these fluids. Some of the increase observed was within the experimental error. Again, the change in wave velocities indicates that these shales were only slightly water sensitive. The higher wave velocity parallel to bedding planes than that perpendicular to bedding planes is probably due to the preferential layering of minerals that results in less dispersion parallel to the bedding planes.

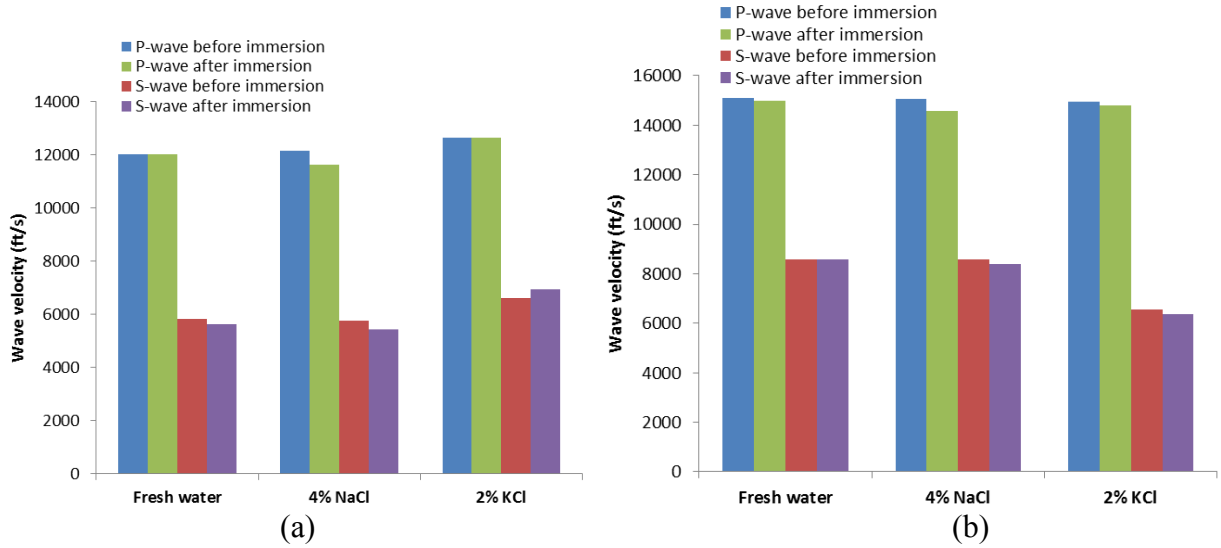

Figure 8.10: Wave velocity of TGS before and after immersed in fresh water, 4% NaCl and 2% KCl for 24 hours perpendicular (a) and parallel to bedding planes (b).

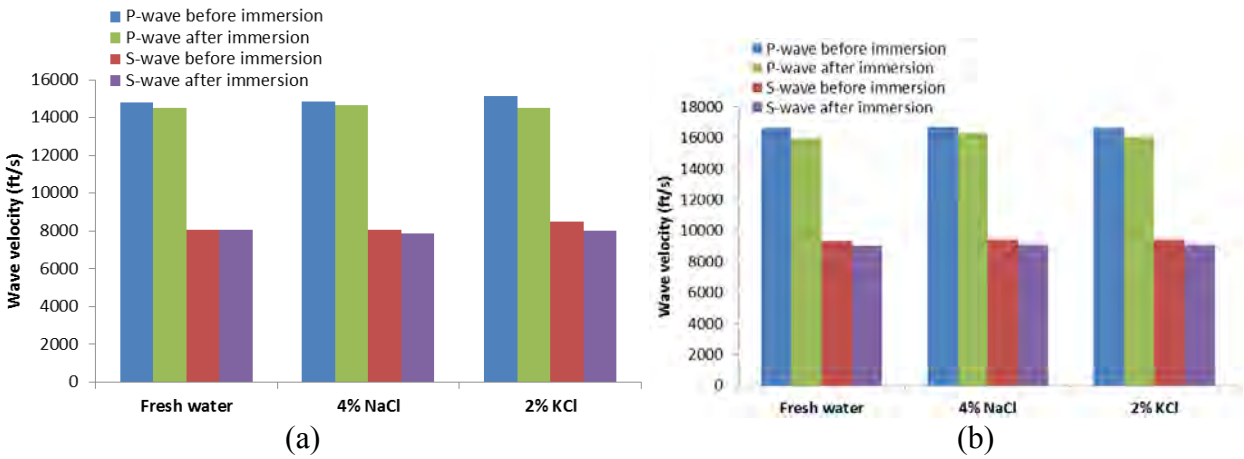

Figure 8.11: Wave velocity of WGS before and after immersed in fresh water, 4% NaCl and 2% KCl for 24 hours perpendicular (a) and parallel to bedding planes (b).

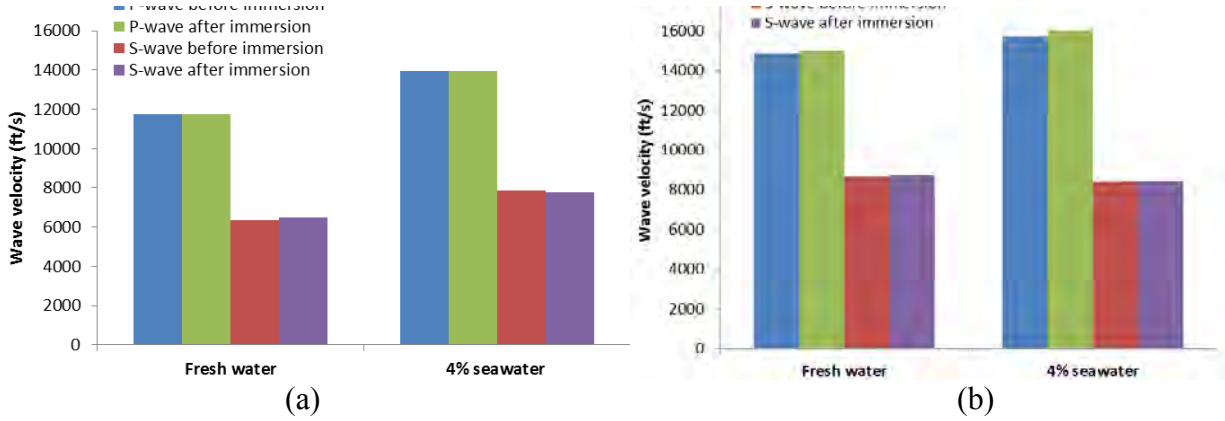

Figure 8.12: Wave velocity of Barnett shale before and after immersed in fresh water and 4% seawater for 24 hours perpendicular (a) and parallel to bedding planes (b).

The dynamic Young's modulus and Poisson's ratio perpendicular to the bedding planes were calculated using Eq. (2-1) and Eq. (2-2). Figure 8.13 – 8.15 show that in general, Young's modulus decreased and Poisson's ratio increased after TGS, WGS and the Barnett shale were exposed to these fluids for 24 hours. Some anomalies were again resulted from the experimental random error in the wave velocity measurement. Similarly, the elastic moduli suggest that there shales were only slightly sensitive to water-based fluids.

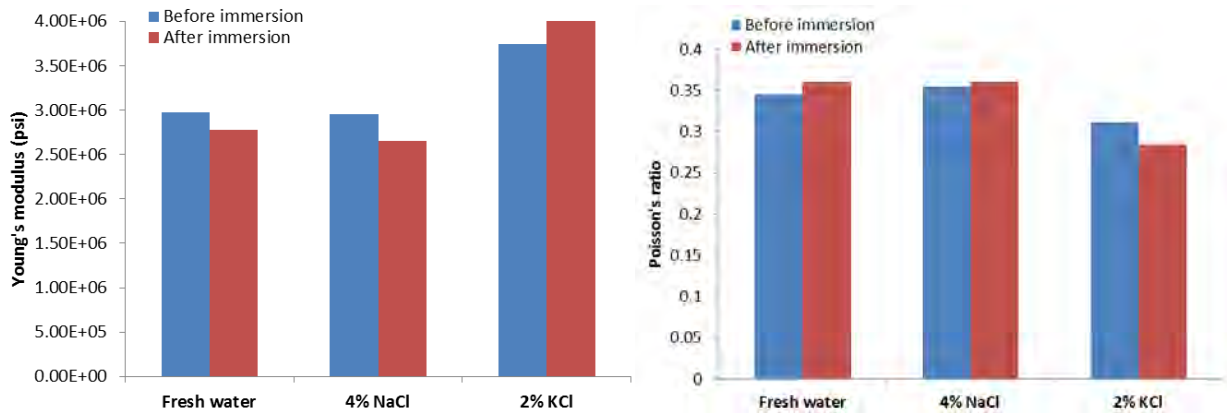

Figure 8.13: Young's modulus (a) and Poisson's ratio (b) of TGS before and after immersed in fresh water, 4% NaCl and 2% KCl for 24 hours.

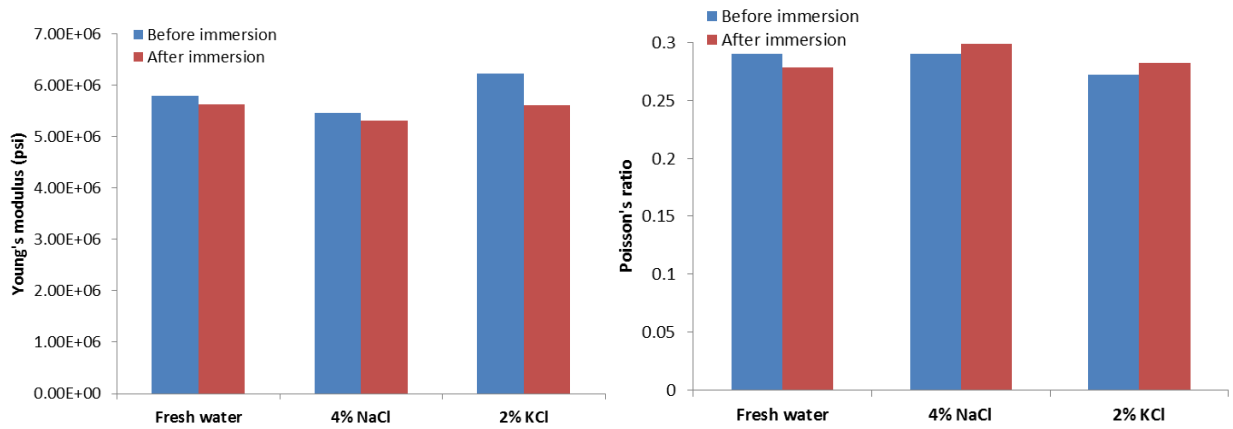

Figure 8.14: Young's modulus (a) and Poisson's ratio (b) of WGS before and after immersed in fresh water, 4% NaCl and 2% KCl for 24 hours.

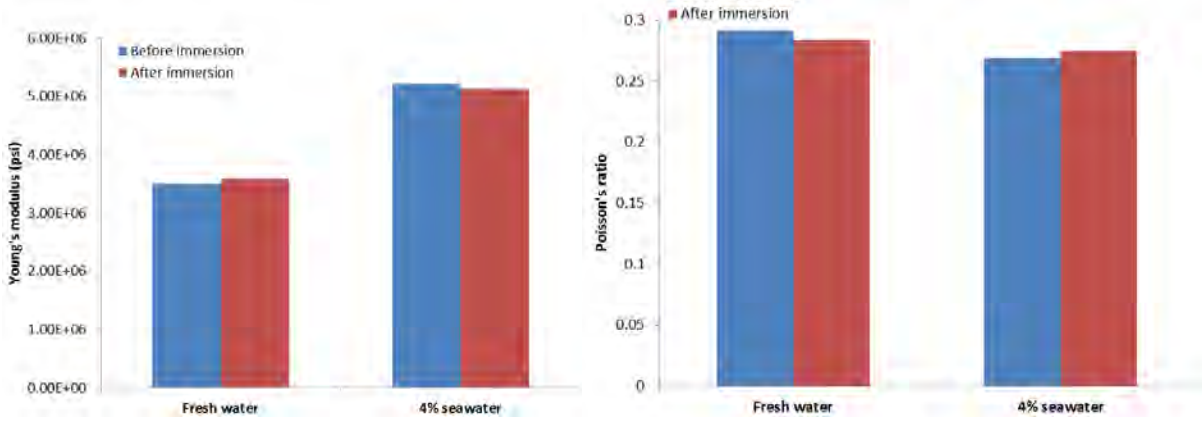

Figure. 8.15: Young's modulus (a) and Poisson's ratio (b) of the Barnett shale before and after immersed in fresh water and 4% seawater for 24 hours.

In this chapter, we present a new laboratory protocol to study the interaction of organic-rich shale with water-based drilling and fracturing fluids. The compatibility of these fluids is evaluated through relatively simple screening tests that include determining native shale

properties and examining changes in shale mechanical properties after exposure to water-based fluids.

From the change in weight, hardness, acoustic wave velocities and elastic modulus after shale's exposure to water-based fluids, we concluded that TGS, WGS and the Barnett shale were only slightly water-sensitive. Fresh water resulted in the most swelling and weight gain. KCl is more effective in inhibiting shale swelling than NaCl because of its smaller hydrated radius. From the weight change, it is evident that WGS shale was slightly more sensitive to water-based fluids than TGS. This could be due to the lower original water activity of the WGS and the greater clay content that WGS has. This protocol can be used as a screening procedure for testing a large number of drilling and fracturing fluids to study the impact these fluids will have on organic-rich shales in terms of wellbore stability and proppant embedment problems.

8.3 References

Breeden, D., Shipman, J. 2004. Shale Analysis for Mud Engineers. AADE-04-DF-HO-30 presented at the AADE 2004 Drilling Fluids Conference in Houston, Texas, April 6 – 7.

Brinell. J.A. 1990. Way of Determining the Hardness of Bodies and Some Applications of the Same. *Teknisk Tidskrift*, **5**: 69 – 87.

Chenevert, M.E. 1970. Shale Alteration by Water Adsorption. *J. Petrol. Tech*., 1141 – 1148, Sept.

Chenevert, M.E. and M. Amanullah. 2001. Shale Preservation and Testing Techniques for Borehole-Stability Studies. *SPE Drill & Compl.* **16 (3)**: 146 – 149. SPE-73191-PA.

Ground Water Protection Council and ALL Consulting. 2009. Modern Shale Gas Development in the United States: A Primer, prepared for the U.S. Department of Energy, Office of Fossil Energy, and the National Energy Technology Laboratory.

Sharma, M.M. 2004. Near Wellbore Problems. PGE 383 notes, the University of Texas at Austin.

Tutuncu, A.N., Mese, A.I. 2011. Relationship between Permeability, Acoustic, Mechanical and Strength Anisotropies in Unconventional Reservoirs and Seal Shales. ARMA 11-532 presented at the 45th US Rock Mechanics/Geomechanics Symposium held in San Francisco, CA, June 26 – 29.

Winston, P.W., Bates, D.H. 1960. Saturated Solutions for the Control of Humidity in Biological Research. *Ecology.* **41***:* 232 – 237.

Zhang, J., Al-Bazali, T., Chenevert, M.E., Sharma, M.M. 2004. A New Gravimetri-Swelling Test for Evaluating Water and Ion Uptake in Shales. SPE 89831 presented at the SPE Annual Technical Conference and Exhibition held in Houston, Texas, USA, 26 – 29 September.

Zhang, J., Al-Bazali, T.M., Chenevert, M.E., Sharma, M.M., Clark, D.E., Benaissa, S., Ong, S. 2006. Compressive Strength and Acoustic Properties Changes in Shale with Exposure to Water-Based Fluids. ARMA/USRMS 06-900 paper presented at Golden Rocks 2006, the 41st U.S. Symposium on Rock Mechanics (USRMS): "50 Years of Rock Mechanics – Landmarks and Future Challenges.", held in Golden, Colorado, June 17 – 21.

Chapter 9: The Impact of Shale Preservation on Shale Petrophysical Properties

9.1 Introduction

In recent years, shale gas production has played an important role in hydrocarbon exploration in the US. Due to horizontal drilling and hydraulic fracturing, shale plays will receive more interest from companies and governments. The development of gas-shale reservoirs is highly dependent on petrophysical parameters that indicate gas content (Shebl et al. 2013). The procedures for measuring the petrophysical properties of shale vary substantially from one lab to another (Passey et al. 2010; Civan et al. 2012; Kumar et al. 2012). Quite often, shale permeability and mechanical property data measurements are obtained from shales that are not preserved, as these samples are easier to obtain (Kumar et al. 2012). Sometimes reconstituted and compacted samples are made from drilled chips (Chenevert et al. 1989; Passey et al. 2010).

Shale is very sensitive to water, so the properties of a shale will be changed if it is poorly preserved (Weaver et al. 2012). We performed a series of experiments that determine the following petrophysical properties of hydrocarbon bearing shales: mineralogy, native shale water activity, original fluid content, Brinell hardness change under swelling, sonic velocities change under swelling, and fluid permeability. As an example of organic rich shale, we choose an Eagle Ford shale, which is from the most active shale play in the US (Tian et al. 2013).

Large and consistent differences are observed in the shale's measured properties if the shale is not properly preserved. In this paper, after comparing the measurement results between well preserved and dried out shale samples to highlight the significance of high quality preservation work, we present a methodology that we hope will become an industry standard for preserving and preparing shales for petrophysical measurements.

9.2 Lab Evaluation of Eagle Ford Shale

9.2.1 Original Fluid Content and Physical Properties of Eagle Ford Shale

The GRI method of shale sample analysis was used to measure the original fluid contents and the physical properties of Eagle Ford shale. The shale sample was crushed into small particles from 0.5 to 0.85 mm in diameter in order to efficiently remove the pore liquid by distillation-extraction. The sequence tests provided core saturations, density, and porosity information (Table 9.1 and Table 9.2). To show the changes of density and porosity with preservation, physical properties were measured when shale was both well preserved and when it was dried out. There was not much difference in density results. Bulk density and grain density were slightly increased. However, the porosity was increased as much as 2.7 times when the sample was dried.

Table 9.1: Original fluid contents of Eagle Ford shale

Fluid Saturation	Water Saturation	Oil Saturation	Gas Saturation	Totals
% of Pore Volume	42.1	20.5	37.4	100

Table 9.2: Physical properties of Eagle Ford shale

As received (Preserved)			Vacuum Dried at 212°F		
Bulk Density	Grain Density	Gas Filled Porosity	Bulk Density	Grain Density	Helium Porosity
2.55 gm/cc	2.60 gm/cc	1.8% of BV	2.53 gm/cc	2.65 gm/cc	4.9% of BV

9.2.2 Swelling Effect on Eagle Ford Shale

Because we knew our shale had a moderate clay content, we expected that the shale would display a sensitivity to water. To see how swelling affects the characteristics of the shale, the following tests were done before and after the swelling of the sample that has been immersed into a 4wt% NaCl sea water solution: a hardness test, a weight change measurement, and a wave velocity measurement.

9.3 Sample Preparation

For this test, shale specimens were prepared by cutting them into a 1 inch cubes (Figure 1). There are some clear advantages in using samples that do not require coring. Often preserved shales are difficult to core as the rotation of the coring bit shears the sample apart and core recovery can be poor (particularly in high clay content samples). Rectangular samples are much easier to prepare as they can be cut with a straight precision saw cut. Rectangular or cubic samples also allow us to make measurements parallel and perpendicular to the bedding planes simultaneously and on the same sample. Since preserved shale samples are difficult to obtain it is important to minimize shale sample requirements.

For samples that had been stored in mineral oil, they were washed with hexane. To see the effect of preservation, we needed to have dried-out samples to compare with well-preserved samples. We put several samples into a lab oven and kept them at 200°F for two days to extract the fluid from the sample. They were then cooled at room temperature. Even though this baking process did not extract all the fluid from inside the sample, it was enough to simulate the condition of a poorly preserved shale sample. All of the following tests were performed with preserved and dried-out samples for comparison.

Finally, it is important to state the importance of proper coring and core preservation procedures in the field. All cores taken must be preserved and stored in wax or plastic with minimum exposure to the atmosphere. These procedures are well established in the industry and will be used if a specific request is made to the service provider. If the core needs to be slabbed, the larger portion should be stored under mineral oil to preserve its water content.

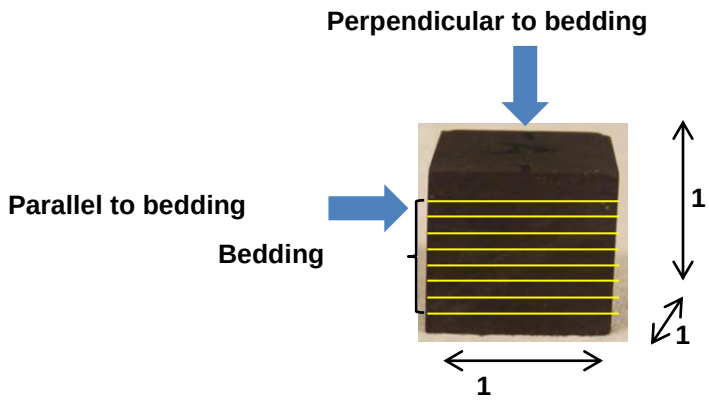

Figure 9.1: Sample dimension for swelling test

9.3.1 Weight Change Measurement

The weight of the shale samples were measured before and after immersion into the sea water during the swelling tests. As shown in Figure 9.2, the weight change of the dried-out sample is about four times larger than the change of the preserved sample, meaning the dried-out sample absorbed much more liquid than the preserved sample.

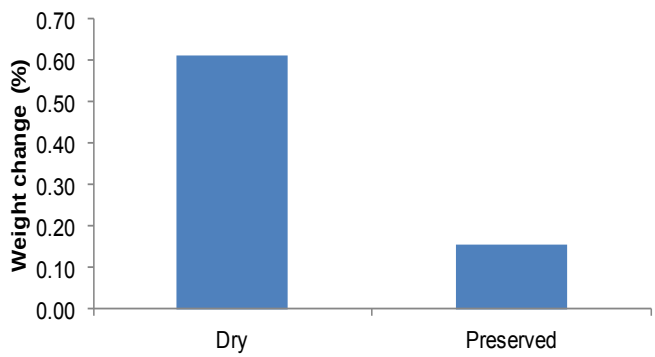

Figure 9.2: Weight change of the dry sample and the preserved sample before and after the swelling with 4wt% NaCl sea water.

9.3.2 Brinell Hardness Test

The resistance of the rock to indentation has a direct correlation to rock tensile strength. The Brinell hardness test is performed by applying a measured load to an indenter that is in contact with the sample. MS-1 multi-scale durometers by Rex Gauge were used to measure the Brinell hardness of the shale samples. The durometer is equipped with an adaptor and various scales that are designed for different hardness ranges. We used the type D scale to measure our sample shale's hardness. The type D scale is the hardest scale and is designed for hard rubber and plastics.

For the purpose of investigating the fluid sensitivity of shales, the Brinell hardness was measured before and after the shales come into contact with the 4wt% NaCl sea water, in both directions, parallel and perpendicular to bedding. Table 9.3 and Figure 9.3 show the change in

Brinell hardness after the Eagle Ford shales were exposed to the sea water. HBS (H from hardness, B from Brinell and S from the steel indenter) 10/3000 represents the hardness. The hardness is measured with a steel ball with a 10 mm diameter that puts 3000 kg force on the sample. The Brinell hardness was read from the reading of the durometer.

The dried-out sample showed more changes in both directions. The hardness of the preserved sample did not change in the perpendicular direction, but it showed a 3% decrease in the parallel direction. The dry sample, however, showed a 5% decrease in the perpendicular direction and a 6% decrease in the parallel direction. This relatively small chance in the hardness is directly related to the high calcite content of the Eagle Ford shale. Shales with higher clay content do show larger changes in hardness after exposure to water based fluids.

Table 9.3: Brinell hardness change before and after swelling

Condition	Perpendicular to bedding planes			Parallel to bedding planes		
	Before swelling	After swelling	Δ Hardness	Before swelling	After swelling	Δ Hardness
Dry	332.63	316.00	-5%	336.33	316.00	-6%
Preserved	299.25	299.25	0%	316.00	306.83	-3%

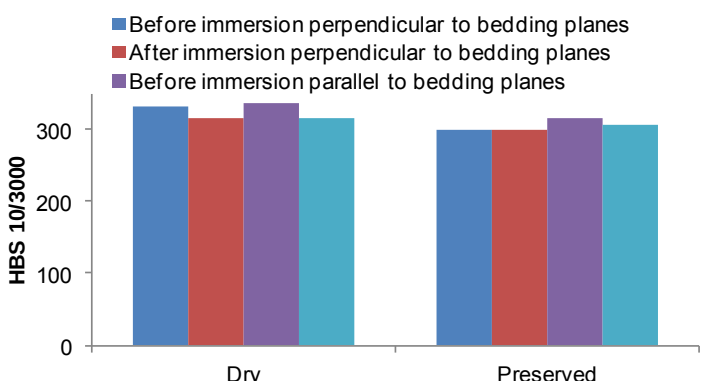

Figure 9.3: Brinell hardness of shale before and after immersion in 4wt% NaCl for 24 hours

9.3.3 Wave Velocity Measurement

The wave velocity measurements are very helpful for determining dynamic elastic rock properties. P-wave transit time data are useful in identifying lithology, porosity, and pore fluids (Bumb et al. 1988). Wave velocities were measured with a pulse transmission set-up, and they were measured both perpendicular and parallel to the bedding planes. They were also measured before and after immersion. Table 9.4 and Figure 9.4 show the changes in acoustic wave velocities after the Eagle Ford shales were immersed in the 4wt% NaCl sea water for 24 hours.

Table 9.4: P and S wave velocity

Condition	Perpendicular to bedding planes				Parallel to bedding planes			
	Before swelling		After swelling		Before swelling		After swelling	
	P-wave	S-wave	P-wave	S-wave	P-wave	S-wave	P-wave	S-wave
Dry	12016	7584	12076	6647	16090	8715	15672	8620
Preserved	14839	8064	14655	7852	16686	9390	16241	9084

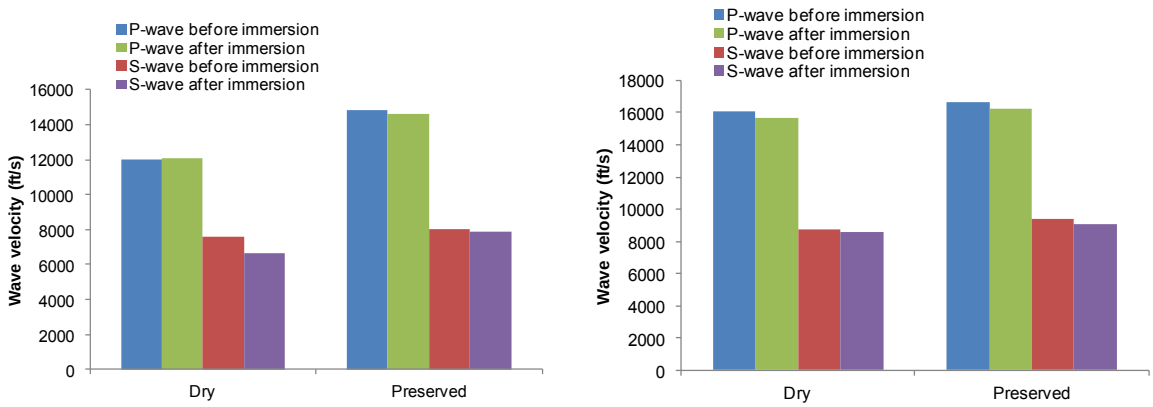

(a) (b)

Figure 9.4: Wave velocity result (a) perpendicular to bedding planes and (b) parallel to bedding planes

From the data on wave velocities, we can calculate the dynamic Young's modulus and Poisson's ratios. Both measures are important factors for predicting the in-situ shale stresses. The p and s wave velocities are related to the elastic modulus as follows:

$$E = \frac{v_s^2 \rho \left[3\left(\frac{v_p}{v_s}\right)^2 - 4\right]}{\left[\left(\frac{v_p}{v_s}\right)^2 - 1\right]} \quad , \quad \nu = \frac{1}{2}\frac{\left[\left(\frac{v_p}{v_s}\right)^2 - 2\right]}{\left[\left(\frac{v_p}{v_s}\right)^2 - 1\right]}$$

Where, E is Young's modulus, ν is Poisson's ratio, ρ is density of the shale, v_p is the p-wave velocity and v_s is the s-wave velocity.

Table 9.5 and Figure 9.5 show the calculated Young's modulus and Poisson's ratio from the wave velocity results. Both results showed that dry samples' ratios are significantly different than the ratios of the preserved samples. For Young's modulus, the preserved sample changed by only 3%, but the dry sample changed by 15%, making it five times larger than the value of the preserved sample. Moreover, there is a large difference between the results of the Poisson's ratios of the samples. The ratio of the dry sample increased 67%, and it is twenty-two times larger than the value of the preserved sample.

Table 9.5: Young's modulus and Poisson's ratio result

Condition	Young's Modulus (psi)			Poisson's ratio		
	Before swelling	After swelling	Change (%)	Before swelling	After swelling	Change (%)
Dry	4.47E+06	3.81E+06	-15	0.1688772	0.2827015	67
Preserved	5.46E+06	5.30E+06	-3	0.2904989	0.2986787	3

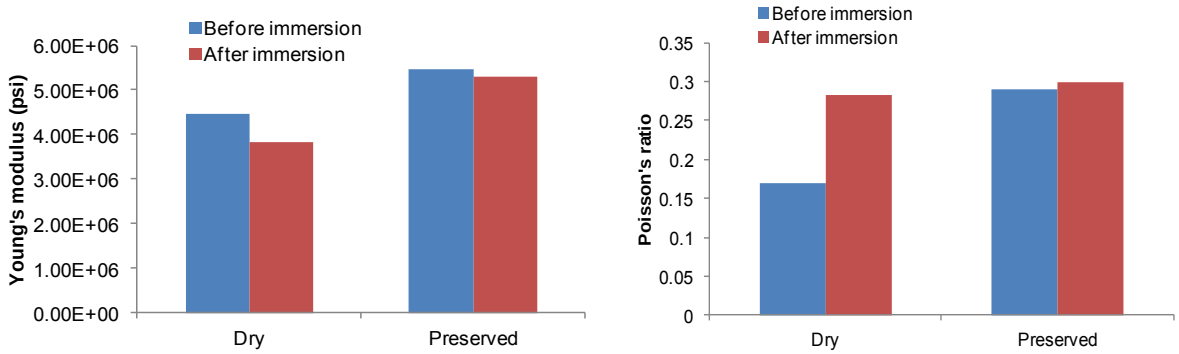

(a) (b)

Figure 9.5: (a) Young's modulus change and (b) Poisson's ratio change of dry and preserved samples under swelling

9.4 Permeability Measurements

9.4.1 Pressure Penetration Technique (PPT)

A pressure penetration technique (PPT) was used to measure the permeability of shale samples in contact with the 4wt% NaCl sea water and also with nitrogen gas.

9.4.2 Sea water Permeability Measurement

The permeability of the shale to sea water (4wt%NaCl) was measured with both preserved and dried-out samples. Figure 9.6 and Figure 9.7 show the pressure buildup graphs of two tests performed. The top line is the upstream pressure, and the bottom line is the downstream pressure. We used the early time portion of the downstream pressure to calculate the sea water permeability. The sea water permeability of the preserved sample is 183nD under 170psi effective stress, and it is three times larger than the permeability of the dry sample which is 68nD under 80psi effective stress. We believe that the dried out or desiccated sample has clays that have shrunk in volume thereby decreasing the pore space open to sea water flow and the permeability.

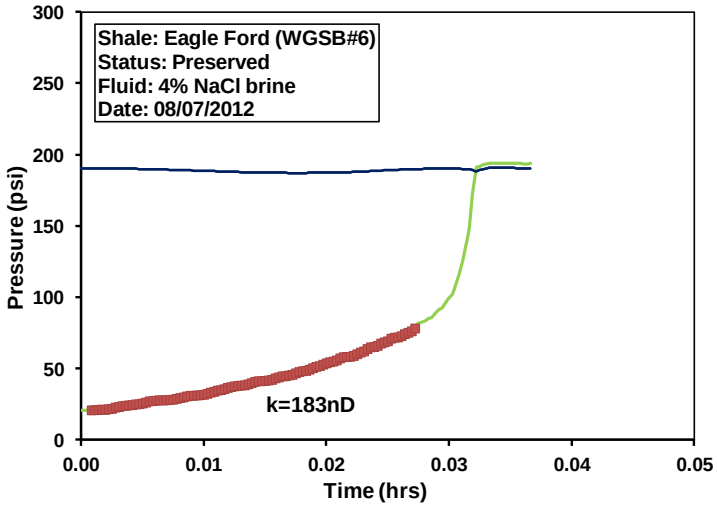

Figure 9.6: Sea water permeability results of preserved sample from pressure penetration tests

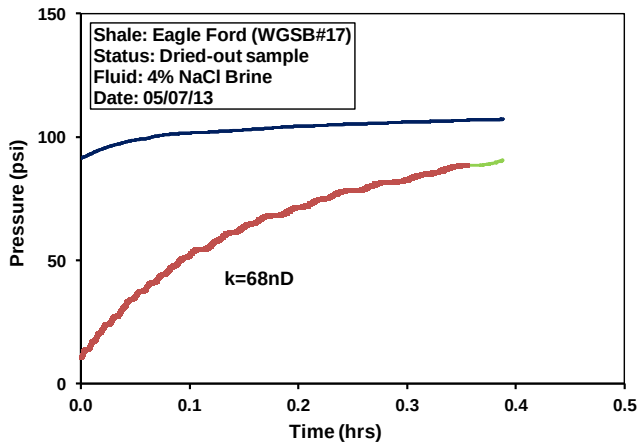

Figure 9.7: Sea water permeability results of dried-out sample from pressure penetration tests

9.4.3 Nitrogen Permeability Measurement

Shale permeability was measured using nitrogen with a dried-out sample using the PPT cell and also the GRI method. Figure 8 shows the pressure buildup graph of the PPT test. The nitrogen permeability of the dried sample is 52nD. At the GRI method, we use cylinder type sample which is 3.8cm in diameter with a length of 4cm. We found the nitrogen permeability to be 22µD using the GRI method, which is 400 times larger than our PPT test result. There can be many reasons for the differences in the two results. Perhaps the most likely is the introduction of cracks in the sample, the removal of water can result in additional small cracks that make the smaller sample size more susceptible to fluid movement. The PPT test used the preserved core itself without modifying its original structure, while the GRI method used the crushed shale sample. The GRI method reflects the matrix permeability as modified by the presence of cracks in the sample while the PPT method measures the matrix permeability. Sample preparation in the GRI method will be a key to reproducibility. The PPT method is less susceptible to variations due to sample preparation.

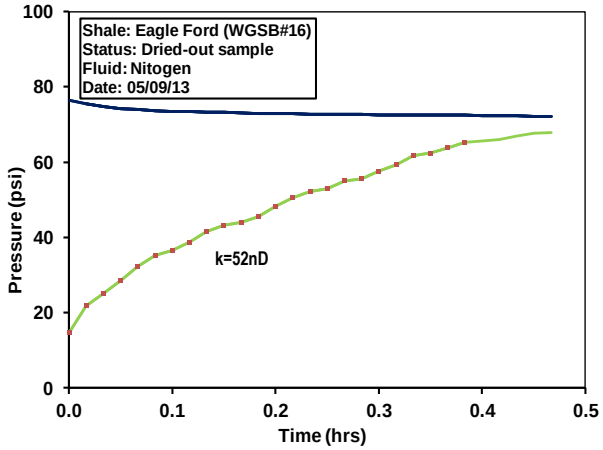

Figure 9.8: Nitogen permeability results of dried-out sample from pressure penetration tests

9.4 Conclusions

Table 9.6 shows a summary of the test results presented in this Chapter. They clearly show the differences between the results of preserved samples and results of un-preserved or desiccated samples. These results indicate that measurements such as weight change, hardness, wave velocity and permeability need a carefully prescribed sample preparation protocol using preserved samples to yield reliable and reproducible results.

To preserve the core sample in the original state, the humidity of the chamber in which the samples are stored must be controlled. Strippable plastic (wax) coating must be used in the field for sealing the core when it is taken in the field. The coating is done by dipping at wax bath, and special formulated wax for core encapsulation is used (Baker Hughes Incorporated. 2010). It prevents water from exiting the core. After the core has arrived at the lab, its original water activity should be measured. Then, samples can be kept in the proper desiccators, as discussed previously in this paper. After removing the core from its stored state, it should be immersed in oil so as to preserve the shale and maintain its saturation condition. Most shale cores and samples can be kept in a sealed steel can immersed in oil, and this does not affect their original water activities and it maintains the saturation condition.

Table 9.6: Summary of test results

Properties		Preserved sample	Dried-out sample	Difference
Weight Change		0.61%	0.16%	4 times
Hardness	**perpendicular to bedding**	0%	-5%	5 times
	parallel to bedding	-3%	-6%	2 times
Young's modulus		-3%	-15%	5 times
Poisson's ratio		3%	67%	22 times
Sea water permeability		183nD	68nD	3 times

9.5 References

Baker Hughes Incorporated. 2010. Wax Encapsulation Core Preservation Services, http://www.bakerhughes.com/news-and-media/resources/brochures/wax-encapsulation-product-overview (accessed 17 June 2013)

Bumb, A.C. and McKee, C.R. 1988. Gas-Well Testing in the Presence of Desorption for Coalbed Methane and Devonian Shale. *SPE Form Eval* **3** (1): 179-185. SPE-15227-PA. http://dx.doi.org/10.2118/15227-PA

Civan, F., Rai, C.S., and Sondergeld, C.H. 2012. Determining Shale Permeability to Gas by Simultaneous Analysis of Various Pressure Tests. *SPE J.* **17** (3): 717-726. SPE-144253-PA. http://dx.doi.org/10.2118/144253-PA

Chenevert, M.E. and Osisanya, S.O. 1989. Shale/Mud Inhibition Defined with Rig-site Methods. *SPE Drilling Eng* **4** (3): 261-268. SPE-16054-PA. http://dx.doi.org/10.2118/16054-PA

Cai, J., Chenevert, M.E., Sharma, M.M., and Friedheim, J., 2012. Decreasing Water Invasion Into Atoka Shale Using Nonmodified Silica Nanoparticles. SPE Drilling & Compl 27 (1): 103-112. SPE-146979-PA, http://dx.doi.org/10.2118/146979-PA

Chenevert, M.E. and Amanullah, M., 2001. Shale Preservation and Testing Techniques for Borehole-Stability Studies. *SPE Drilling & Compl* **16** (3): 146-149. SPE-73191-PA. http://dx.doi.org/10.2118/73191-PA

Ji, L., Guo Q., Friedheim, J., Zhang, R., Chenevert, M., and Sharma M., 2012., Laboratory Evaluation and Analysis of Physical Shale Inhibition of an Innovative Water-Based Drilling Fluid with Nanoparticles for Drilling Unconventional Shales, SPE-158895-MS presented at SPE Asia Pacific Oil and Gas Conference and Exhibition in Perth, Australia, 22-24 October. http://dx.doi.org/10.2118/158895-MS

Kumar, V., Sondergeld, C.H.,and Rai, C.S. 2012. Nano to Macro Mechanical Characterization of Shale, SPE-159804-MS presented at SPE Annual Technical Conference and Exhibition in San Antonio, Texas, USA, 8-10 October. http://dx.doi.org/10.2118/10.2118/159804-MS

Passey, Q.R., Bohacs, K.M., Esch, W.L., Klimentidis, R., and Sinha, S., 2010. From Oil-Prone Source Rock to Gas-Producing Shale Reservoir - Geologic and Petrophysical Characterization of Unconventional Shale Gas Reservoirs, SPE-131350-MS presented at International Oil and Gas Conference and Exhibition in Beijing, China, 8-10 June. http://dx.doi.org/2118/131350-MS

Sharma, M.M., Zhang, R., Chenevert, M.E., Ji, L., Guo, Q., and Friedheim, J., 2012. A New Family of Nanoparticle Based Drilling Fluids, SPE-160045-MS presented at SPE Annual Technical Conference and Exhibition in San Antonio, Texas, USA, 8-10 October. http://dx.doi.org/10.2118/160045-MS

Shebl, M.A., Nyaaba, C., and Yalavarthi, R., 2013. Role of Detailed Reservoir Characterization and Lateral Placement on Well Performance in the Marcellus Shale Gas Reservoir, IPTC-16718-MS presented at the 6th International Petroleum Technology Conference, Beijing, China, 26 – 28 March. http://dx.doi.org/10.2523/16718-MS

Tian, Y., Ayers, W.B., and McCain Jr., W.D., 2013. The Eagle Ford Shale Play, South Texas: Regional Variations in fluid Types, Hydrocarbon Production and Reservoir Properties, IPTC-16808-MS presented at the 6th International Petroleum Technology Conference, Beijing, China, 26 – 28 March. http://dx.doi.org/10.2523/16808-MS

Weaver, J.D., Nguyen, P.D., and Loghry, R.A. 2011. Stabilizing Fracture Faces in Water-Sensitive Shale Formations, SPE-149218-MS presented at SPE Eastern Regional Meeting, Columbus, Ohio, USA, 17–19 August. http://dx.doi.org/10.2118/149218-MS

Winston, P.W. and Bates, D.H., 1960. Saturated Solutions for the Control of Humidity in Biological Research, *Ecology* **41** (1): 232-237 http://dx.doi.org/10.2307/1931961

Zhou, J., Jung, C. M., Chenevert, M. E., and Sharma, M. M., 2013. Petrophysical Characterization of Organic-Rich Shales: A New Standardized Protocol, ARMA-13-546 is prepared for presentation at the 47th US Rock Mechanics / Geomechanics Symposium held in San Francisco, CA, USA, 23-26 June.

Chapter 10: Using Nanoparticle Stabilized Foams to Achieve Wellbore Stability in Shales

10.1 Summary

In this chapter we investigate the use of nanoparticle stabilized foams for the reduction in permeability of the shale. The increased stability of the foam due to the addition of NP's decreases the amount of liquid contacting the shale surface by adding resistance to the breaking of the bubbles in the foam. Similarly to the surfactant used as the foaming agent, the NP's enhance the exclusion of water contacting the shale surface by forming stable bubbles in the foam. The bubbles cannot enter the pore throats due to the higher entrance pressure of nitrogen into the pores of the shale. Another possible mechanism for the reduction of permeability for NP enhanced foam is the plugging of pores by the NP's in the liquid phase of the foam. The liquid that does enter the pore throats contains NP's and has been shown to plug the pore throats of the shale. The physical blocking of the pore throats restricts the flow of water into the pores of the shale. Nanoparticle enhanced foams lower the permeability of both outcrop and reservoir shale formations. These tests clearly indicate that this technology is applicable to both drilling and fracturing fluids. The use of foams has the added advantage that that the volume of water used is reduced dramatically and the amount of nanoparticles used is reduced by an order of magnitude.

10.2 Introduction

Foams are very unique and complex fluids. To gain a better understanding of the nature of foams, a brief literature review has been undertaken. Researchers studying foam rheological properties have been in disagreement on the classification of foam. While most agree that foam behaves as a pseudoplastic or Bingham plastic fluid, there is disagreement about which model best predicts flow behavior. The dominating model is the Herschel-Buckley model, but there have also been studies showing foam rheology closely following a power law model. The flow performance differences between studies can likely be linked to the method of foam generation and stabilization (Saintpere et al., 1999). The very nature of foams, consisting of bubbles breaking and reforming, as well as gas fluid being compressed, restricts steady state flow from truly being reached.

The key defining parameter that classifies foam is its quality. Quality is the volume percentage of gas in the emulsion's total volume. It is represented by the following equation:

$$\Gamma = \frac{100V_g}{V_g + V_l}$$

Where, Γ is the foam quality (%), Vg is the volume of gas, Vl is the volume of liquid. Therefore, a higher percentage of gas drives the quality of the foam higher.

Even though there has been disagreement in the general model used to predict rheological properties, there have been some consistent characteristics viewed while studying foam's rheology. The apparent viscosity of foam has been shown to be dependent on five main foam properties (Caiweizel, 1987):

- Foam quality has a direct correlation. As quality increases, apparent viscosity has been shown to increase, even exponentially at high values of quality.
- As temperature increases, the apparent viscosity of the foam decreases.
- Apparent viscosity increases as bubble-size increases.
- As pressure increases, the apparent viscosity of the foam increases until a critical pressure has been reached, and then remains relatively constant.
- The addition of stabilizers, such as polymer or nanoparticles, increases the apparent viscosity of the foam.

Analogous to the dependency of apparent viscosity of foam on the previously mentioned five parameters, is the dependency of the yield point or yield stress of the foam.

Drilling with foam is often used when an underbalanced drilling technique is applied. Results from the field have shown distinct economic advantages when foam drilling has been correctly applied. Underbalanced drilling can result in higher drilling rates and minimize formation damage. Underbalanced drilling is advantageous when drilling through fractured layers, unconsolidated sands, tight formations, and low pressure reservoirs. When employed correctly to the previously noted situations, four main advantages can be realized (Negrao et al., 1997):

- Minimal damage to sensitive hydrocarbon formations
- Faster evaluation of cuttings at the rig floor for hydrocarbon determination
- Prevention of loss circulation into the formation
- Increased rates of penetration with the drill bit

Economic enhancement can only be obtained if the correct situations are present. There are some disadvantages to using this technique as well, like the need for extra equipment at the surface. For example, extra separation and pumping equipment are necessary so as to recover the foam. This can lead to logistical issues when space is limited, such as on offshore platforms or remote locations where getting equipment to the well site is difficult.

One of the more dangerous situations is the use of this technique on a high pressure well. Large, high pressure kicks can move up the annular space at very high rates, so using underbalanced foam drilling is not advisable.

The other application of this research is the use of foams for fracturing. Fracturing occurs when the pressure is increased past the pore and overburden pressures. One difficulty using foams is calculating the friction loss, wellhead pressure, and the resulting density and carrying capabilities during treatment (Caiwiezel et al., 1987). Simulators have been used, so far, to predict these parameters and have been shown to work within a range of error, but work still needs to be performed to create more robust and accurate simulators.

Despite this margin of error, foams still can be used with great success. Foams have high sand or proppant carrying capability, low fluid loss, low hydrostatic head, low-friction pressure drops, quick fluid recovery, low formation damage, and no reduction of fracture conductivity due to fluid ingredients, such as clays (Caiwiezel et al., 1987).

The addition of NP's to foam increases the stability of foam as well as bridges pore throats of shale. Surfactants are employed as the foaming agent and helps stabilize the foam along with the NP's. Research by Espinosa et al. (2009) have shown that stable supercritical

CO2 foams with de-ionized water have been produced with only 0.05% by weight and 4% by weight NP's as a foaming agent. NaCl brine with supercritical CO2 have been produced with an 0.5% by weight addition of NP's.

NP stabilized foams have been shown to be have definite advantages over a purely surfactant stabilized foam. When adding solid particles to foam, a "Pickering Emulsion" is formed. The solid particles act similarly to the surfactant molecules in that an interface exists between the solid and aqueous phase and an interface exists between the solid and non-aqueous phase. Micro-scale investigation is still an ongoing effort to explain the governing mechanism for increases of stability due to the addition of NP's in emulsions.

Foam has the distinct advantage that desorption of the NP's at the liquid phase of the foam does not cause the NP's at the gas liquid interface to also desorb, as is the case with surfactants. In addition, NP's can withstand high temperatures within the well; and, being silica, can be considered inert. Espinosa et al (2009) have also shown these NP stabilized foams can perform well in highly saline environments. There have been some drawbacks to this NP and mud research. The surface charges of the different NP's have shown to have large effects on the rheology of the water based muds. A thickening has been seen as well as either a drop or increase in pH has also been observed. These effects have been erratic and difficult to predict. A major drawback to this technique is the cost of adding NP's into the mud. 10% by weight incurs a high cost in purchasing the amount of NP's for field use.

Just like earlier cases, there are also drawbacks when using NP's to stabilize foam. A resistance to flow has been seen that is 2 to 18 times larger when NP's were added to the liquid phase than that of the foams without any stabilizers added (Espinosa et al 2009). This makes calculation of friction loss in the wellbore even more difficult, but can be possibly reconciled with further research on the rheology of these foams.

10.3 Development of Methodology

Developing the procedure for the experiments has been based both on past work and trial and error. Similar experiments have been run in earlier chapters using drilling WBM's to perform pressure penetration tests and show reduction of permeability generated from different additives including NP's. Techniques have been borrowed from those experiments (Sensoy et al 2009).

The base fluids used to generate our foam have been chosen to be nitrogen and water. Both of these fluids are readily available for field use. Also, they are safe for use especially at high pressures in a lab setting. The use of nitrogen as the gaseous phase in foam also removes the risk of flammable gases entering downhole environments. CO2 is not included because pH would need to be monitored for the production of carbonic acid. Therefore, both nitrogen and water are non-corrosive, non-flammable, and environmentally friendly fluids for both use down-hole as well as their transportation to the well-site.

The test cell used to perform the pressure penetration tests has a maximum pressure of ~400 psi before the o-rings begin to leak. It has been standard practice for both safety and equipment restrictions to run the tests at an upstream pressure of 300psi. This pressure restriction of the test cell also dictates the pressure at which foam can be made and tested. For all tests performed, the foam pressure has been restricted to 300psi for foam generation. At

higher pressures, higher quality foams can be produced, and it would be interesting to study the effects of NP's in such foam.

McLennan et al., (1997) as well as initial experimentation, has shown that 70% quality foam is the ideal mixture for 300psi. Quality is defined as the volumetric percent of gas in the foam, so 70% quality is identical to 70% gas in the foam. McLennan et al., (1997) have indicated that the range of quality foam for both fracturing and drilling is between 70% and 85%. Initial experimentation with the flow loop has indicated that very stable foam is produced at ~70% quality. Below 70% quality two-phase flow can be seen. Above 70% quality large pockets of gas develop reducing the homogeneity of the foam. For the pressure penetration tests, direct contact between the shale and water will rapidly increase the downstream pressure, and result in a higher representative permeability for the foam.

Espinosa et al. (2009) have described the advantages to using different NP's in their work with supercritical CO2 foam. Along with their recommendation, we have chosen to use surface modified NP's. The surfaces of these NP's have been coated with a polymer to reduce the effect of the surface charges that these NP's inherently develop. Sensoy et al. indicated that untreated NP's have a substantial effect on the pH and thickness of water-based muds in which they are injected. To avoid these effects, the surface treated NP's have been chosen due to their neutral pH and the decrease in their surface charges.

We have selected several key characteristics to measure through the generation of foam and the pressure penetration test. In order to measure the quantitative effects of the addition of NP's to the foam, we will measure viscosity, half-life, and permeability of the foam through a sample of shale.

The pressure penetration tests will measure the permeability to study the effects of differing concentrations of NP's in the foam. The concentrations to be measured are 5%, 2%, and 1%.

Tests measuring the permeability of two different shale cores have been run using the aforementioned NP concentrations. The tests performed use samples from two types of shale cores; an Atoka shale and a typical Eagle Ford shale. Atoka shale is known as a reservoir rock and a good simulation for the effects while drilling. The Eagle Ford shale is a reservoir rock and suggests the possible use of NP's in foam for both drilling and fracturing.

Lastly, the Foam Decay Time will be measured using a graduated cylinder filled with 100 mL of foam. A stopwatch will be used to measure the amount of time for the two phases to completely separate. Foam at a rig site needs to be broken down because the pits are not large enough to handle the increase in volume occurring when the gas expands upon exiting of the wellbore.

10.4 Experimental Setup

The following is a flow diagram of both the foam flow loop and pressure penetration set up.

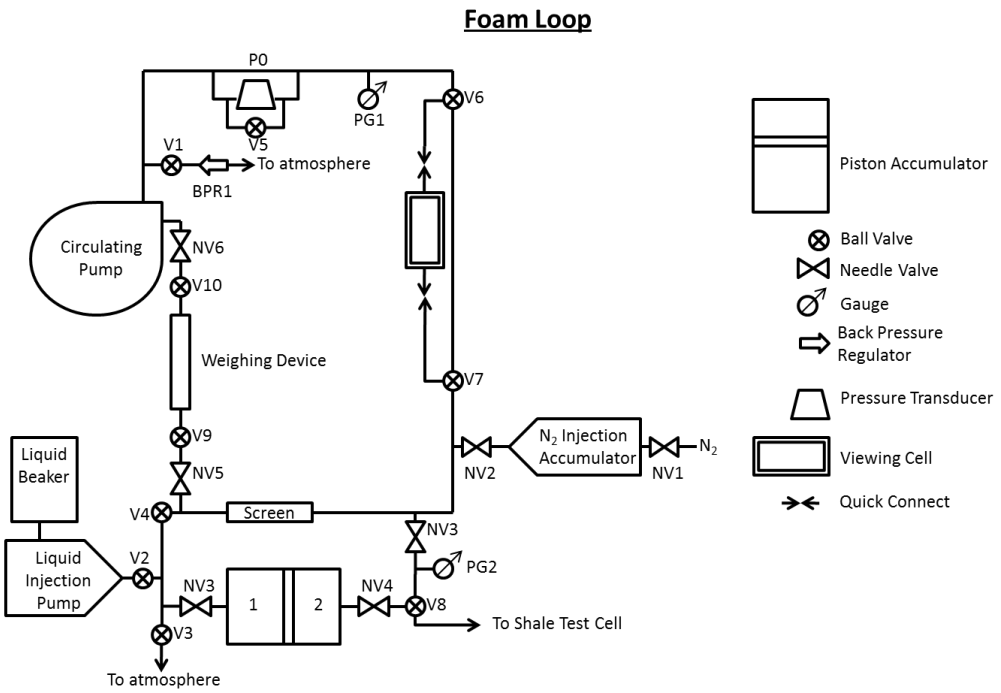

Figure 10.1: Flow Diagram of Foam Flow Loop

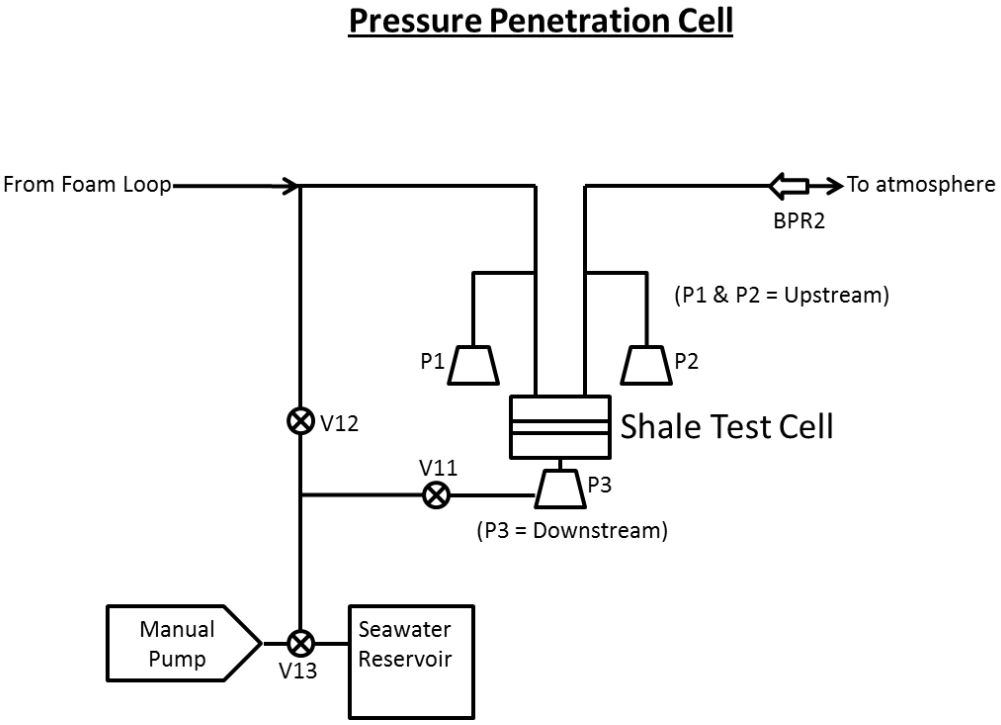

Figure 10.2: Flow Diagram of Pressure Penetration Cell

Liquid Injection Pump: The liquid injection pump is Beckman Model 100A which is a standard piston pump; this one had a maximum rate of 24mL/min and a maximum pressure of 10,000 psi.

All liquids delivered to the system went through this pump. This pump injects the initial liquid solution into the flow loop

Circulation Pump: For foam circulation a Micropump Gear Pump was used. The gears were driven by a magnetically coupled 1 hp electric motor and capable of flow rates up to 2 gallons/min and pressures up to 2,000 psi. This pump circulates the liquid and foam inside the flow loop.

Manual Pump: To set the initial downstream pressure a manually operated piston screw pump has been used. It has a capacity of 48mL and a maximum pressure of 10,000 psi.

N_2 Injection: To control the amount of gas injected, an accumulator is used. This accumulator is a 500mL accumulator with a maximum pressure of 3000 psi. It is without a piston inside and has needle valves on either side (NV1 and NV2).

Viewing Cell: The viewing cell used is a custom made piece of equipment. It is depicted in Appendix A in Figure A.3, and is constructed out of a pipette enclosed in hardened acrylic and has been pressure tested up to 1,000 psi. The viewing cell is a direct indication of the homogeneity of the foam as the quality is increased. It also allows for the measure of the stability of the foam by connecting quick-connect fittings to both sides and capturing foam at high pressure and measuring the time it takes for the foam to break down.

Weighing Device: The weighing device is also a custom made piece of equipment. It is a ¾" section of tubing with a needle valve outside a ball valve on both sides as shown in Appendix A in Figure A.4. It is used to measure the density of the foam and ensure a consistent foam quality between foam tests.

Piston Accumulator: The piston accumulator is used to flow liquid and foam across the shale surface in the shale test cell. It is a 1000mL accumulator with a PTFE piston. The liquid injection pump pushes the piston to push either seawater or foam to the shale cell.

Shale Test Cell: The test cell is exactly same with PPT test cell.

Foam Generator/Screen: Mixing is achieved using a 140 micron screen inside a tubing filter. Originally a beadpack with 180 micron beads was installed, but pressure drop across the beadpack was too high for the pump to push fluids through.

Below are some pictures of the equipment and setup used to perform the tests discussed above.

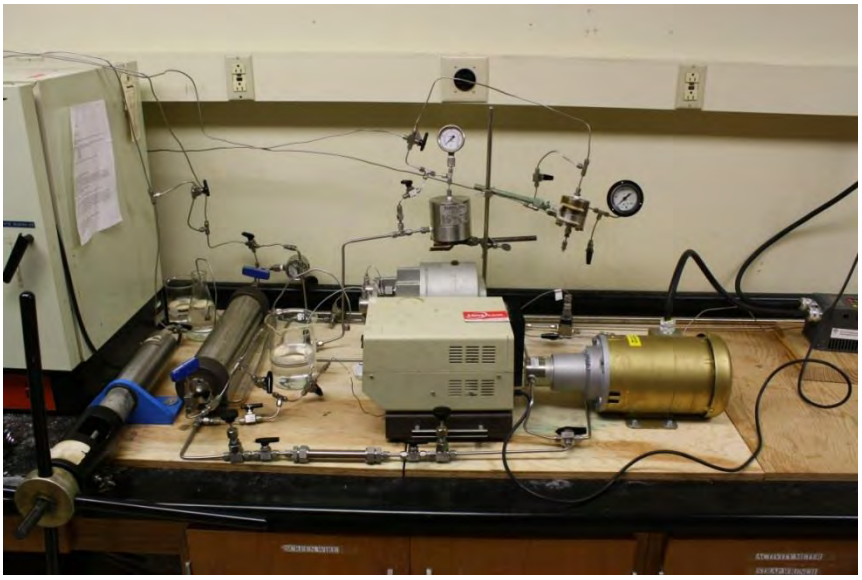

Figure 10.3: Left Half of the Foam Loop

The liquid injection pump, circulation pump, both back pressure regulators, the manual pump, the accumulator, and density measuring device can all be seen in the above picture.

Figure 10.4: Shale Test Cell and Pressure Transducers

Figure 10.5: Close View of the Left Half of the Foam Loop

Figure 10.6: Foam Viewing Cell with Quick Connects

10.5 Experimental Procedures

In order to compare shale samples, a base seawater test is performed on every shale sample before the foam testing commences. For every shale sample, the seawater test is run first, followed by a foam test, and lastly followed by a NP foam test. After both foam tests are performed, the stability of the foam is measured. During the foam generation, when homogeneous foam has been produced, measurements of the pressure drop across the line are taken to calculate the viscosity. The following sections describe the procedure used during these tests.

10.5.1 Screen Wire Construction

In order for foam to flow over the shale sample in the shale test cell, screen wire discs must be used. If more viscous fluids will be used, screen wire with larger hole-size should be used.

1. With a piece of both 240 mesh and 400 mesh screen wire, outline a shale sample using a permanent marker. You will need two of these so follow this procedure twice.
2. Spread a very thin layer of epoxy over the outline made from the permanent marker. This layer should be approximately 0.5 cm wide.
3. When the epoxy is dry, cut out the screen wire disc and shave the edges so that the screen wire disc will not touch an O-ring when placed inside.

10.5.2 Foam and Foam with NP's Pressure Penetration Test

These tests are identical except for the starting liquid injected.

1. Make up the liquid solution to be injected into the flow loop. For regular foam mix 0.3g of SDS per 100mL of de-ionized water. Dilute NP solution to desired NP concentration with de-ionized water. Then add 0.3g SDS per 100mL of solution. Fill side 1 of the piston accumulator completely with seawater (volume of side 2 is 0).
2. Raise the N2 accumulator pressure to 500psi opening NV1, while keeping NV2 closed. Open V4, V2, V1, V5, V9, V10, NV5, and NV6. Make sure V6 and V7 are set to flow through the viewing cell. Close NV3, NV4, and NV7 and make sure V8 is directed toward the flow loop.
3. Make sure a clean beaker is at the outlet of BPR1 to catch the extra solution during initial injection. Set the pump to maximum flow rate and start pumping in the liquid solution for foam generation. Pump and redeliver liquid solution for 30 min or until all air is out of the flow loop.
4. Set BPR1 to 350psi and let the pump continue to run until PG1 reads 350 psi. Once PG1 reads 350psi stop the pump and start up the circulation pump. The circulation pump should be kept below 1000 rpm's to for safety (700-900 rpm).
5. Circulate the pump until P0 is at a constant level. Then open V5 and slowly inject N2 by opening NV1 while keeping NV2 closed. Once NV1 is all the way open, shut it completely and open NV2 to set the accumulator pressure back to 500 psi. Close V5 and once again turn on the circulation pump to the same rpm setting as before.
6. Repeat Step 5 until the foam circulating through the viewing cell is homogeneous. When the circulation pump is stopped, there should be no liquid layer in the bottom of the tube. Adding more N2 to the foam loop past this point can vapor-lock the pump.
7. To calculate density or quality of the foam, while the circulation pump is off, close NV5, NV6, V9, and V10. Then disconnect the tubing between NV6 and V10, and NV5 and V9. Then weigh the tubing with the foam inside and calculate density as described in section 3.3.2. The density should be around 0.3, which equates to a quality of 70%.
8. If the foam is homogenous and the quality is ~70%, record the rpm's and the P0 reading to calculate the viscosity.
9. Begin to fill up the accumulator by opening NV7 and make sure V8 is set toward the path of the accumulator. Slowly open V3 to allow a dripping of water to exit side 1 of the piston accumulator. With the circulation pump on, begin to inject more solution into the system at a very low rate. Keep the pressure reading of P0 constant while additionally solution is being injected. When the pressure drops to 325 psi. Shut V3, stop liquid

injection, and turn stop the circulation pump. Inject N2 into the system to reach 350psi again.

10. Let the circulation pump run until P0 is constant again. Repeat Step 7 to check the quality of foam. Then repeat Step 9 until the amount of liquid that has exited from the piston accumulator is 750mL. As the pressure continues to drop as foam is filling up the accumulator, stop liquid and gas injection at a point where the final pressure in the system is 300 psi (this takes some practice and system know-how).
11. Close NV4 and NV7, and turn V8 so that it directs flow towards the shale test cell. Set BPR2 to 300 psi and slowly open NV4.
12. Use the manual pump to set P3 to 50 psi and close V11 once 50 psi is reached. Then turn on the injection pump with V2 and NV3 open and V3 and V4 closed. Set the pump to a low flow rate so that foam will drip out of the outlet of BPR2 at 1 drop per 5 seconds.
13. Record the data on the computer to calculate permeability.

10.5.3 Foam Stability Test

1. After the piston accumulator is full, close V2 and NV3. Open V3 and fill a graduated cylinder, without letting the foam hit the sides, with 100 mL of foam.
2. Start a stopwatch as soon as the foam hits the 100 mL mark and record the time that the foam takes to completely break down.

10.6 Results and Discussion

10.6.1 Results

10.6.1.1 Atoka Results

The first sets of tests to be presented are the Atoka Shale results from the Pressure Penetration Tests performed. Each test, as described in Chapter 3, has three subsequent steps. The first uses either tap water or seawater as the fluid injected and the permeability is calculated. The second step uses foam as the injection fluid and the third step is foam with the addition of NP's. From each fluid, permeability is calculated and is then compared with the other tests. Each test is labeled using the final concentration of NP's added to the foam.

1.1 5% NP Foam

The first step in this test used tap water as the injection. The results are plotted below.

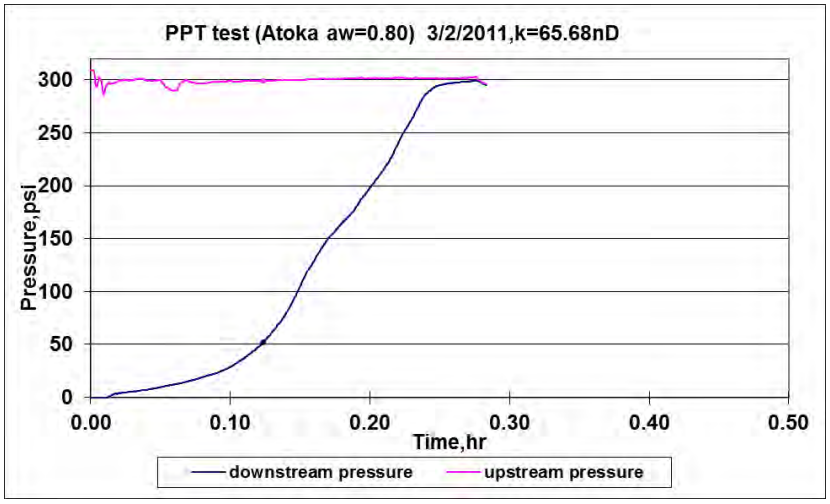

Figure 10.7: Atoka Shale permeability with tap water

Figure 10.7 above shows a high permeability at 65.68 nD, this is most likely due to a small micro-fracture. The fluctuations in the downstream pressure further suggest the presence of a micro-fracture. Although evidence shows that a micro-fracture exists, without the use of a microscope, this cannot be verified. Therefore, the subsequent foam step was performed.

70 % quality foam was used as the injection fluid with the same shale sample used in Figure 7 above. Figure 10.8 shown below shows the results from the foam step of the Pressure Penetration Test.

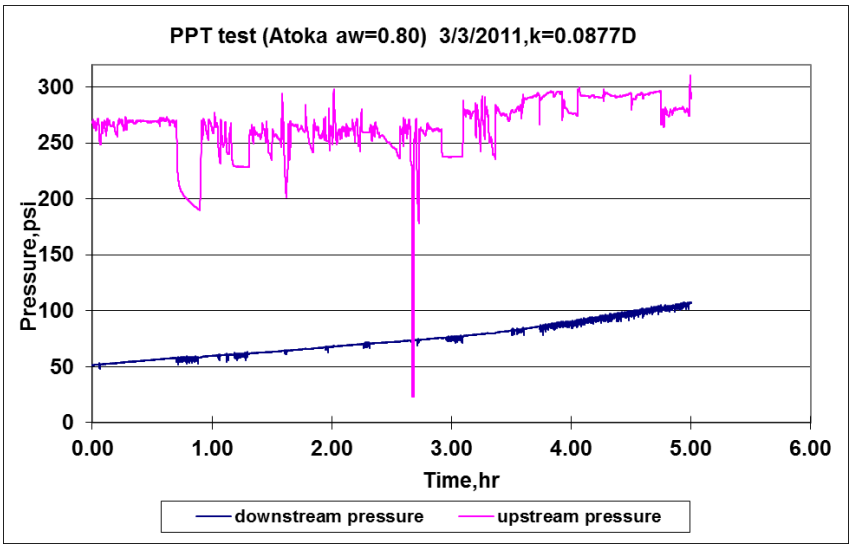

Figure 10.8: Atoka permeability with Foam

Figure 10.8 shows the downstream pressure rise using foam as the injection fluid. The test only lasted 5 hours because the foam was fully consumed. The permeability calculated from this step was 0.0877 nD, much lower than the tap water.

Following the normal foam test, a test using foam with 5% NP's by weight as the injection fluid was performed. To be able to compare both foam steps, the foam quality was set at 70% again. Figure 10.9 shown below displays the results from this step.

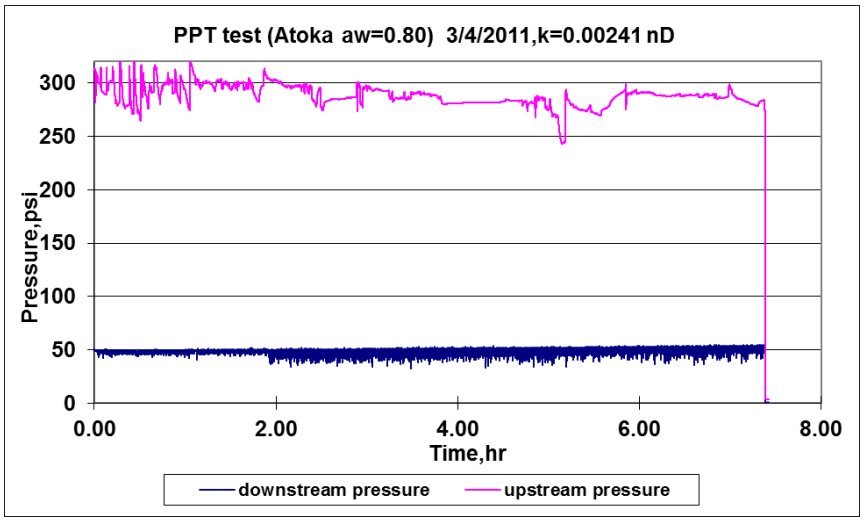

Figure 10.9: Atoka permeability with 5% NP Foam

Figure 10.9 above shows that pressure barely increased at all, resulting in a very low permeability of 0.00214 nD. Figure 10 below show each step in the test on the same graph for comparative purposes.

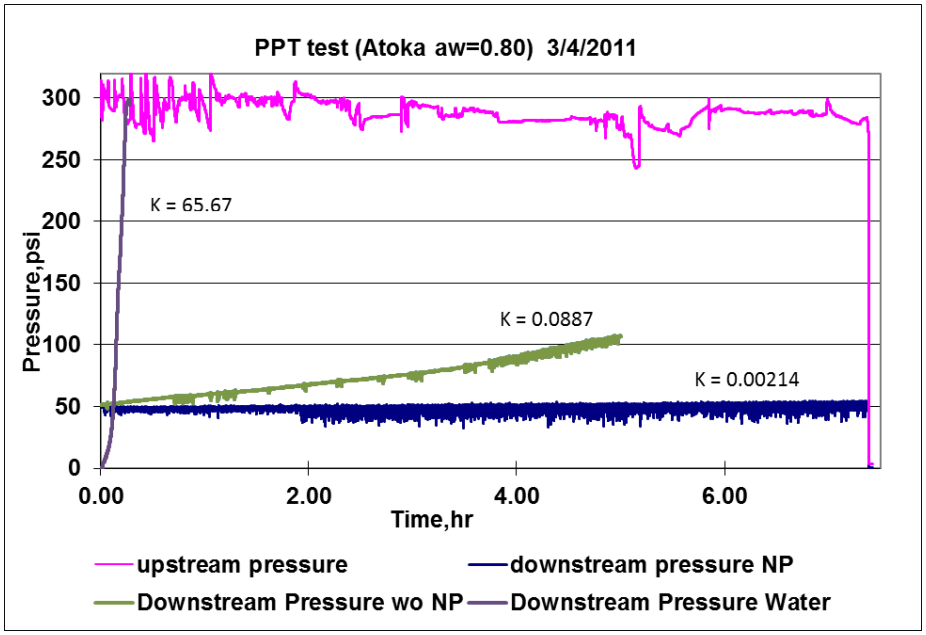

Figure 10.10: Three Step 5% NP Foam Test

Figure 10.10 above shows the reduction in permeability between each of the steps. The extremely large reduction from the tap water step to the foam step is most likely due to a micro-fracture in the shale sample. The smoothness of the foam curve indicates that the foam does not flow through the micro-fracture and the true permeability of the shale is measured. Furthermore, the foam with 5% NP almost completely plugs off the shale with an extremely low permeability of 0.00214 nD.

1.2 2% NP Foam

Again the first step of the test used tap water as the injection fluid. Figure 10.11 below shows the results from this step.

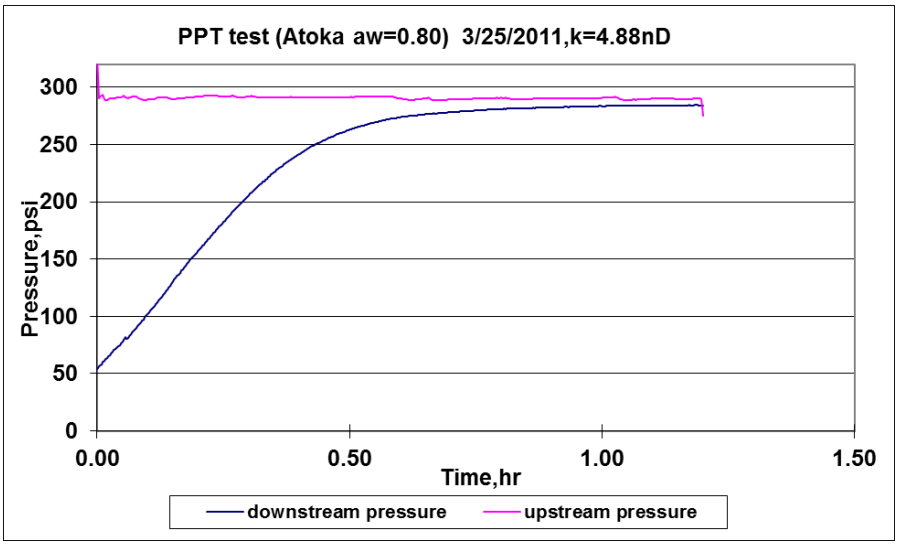

Figure 10.11: Atoka permeability with tap water

Unlike the first step of the previous test with tap water, the permeability is much lower, indicating that this sample of shale is not cracked. From past experience, Atoka shale with water as the injection fluid has a permeability range approximately between 1 and 10 nD. Moving on to the next step of the test using foam, Figure 12 is shown below.

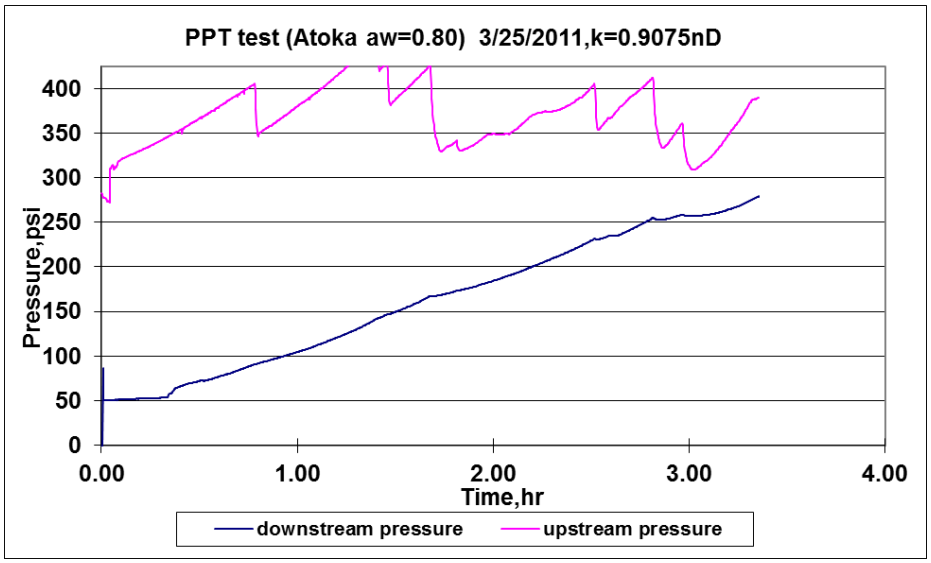

Figure 10.12: Atoka permeability with Foam

The variation of the upstream pressure above is due to injecting the foam to the shale test cell using a needle valve and opening it manually. The needle valve was extremely sensitive and a turn of only a few degrees could raise pressure 20-50 psi. The curve above is not a smooth curve with a few spots of rapid increase. The likely cause of this roughness could be due to a small micro-fracture developing. With the successful results shown above, the third step of the test was performed using foam with 2% NP as the injection fluid. Figure 10.13 shown below displays the results from this step.

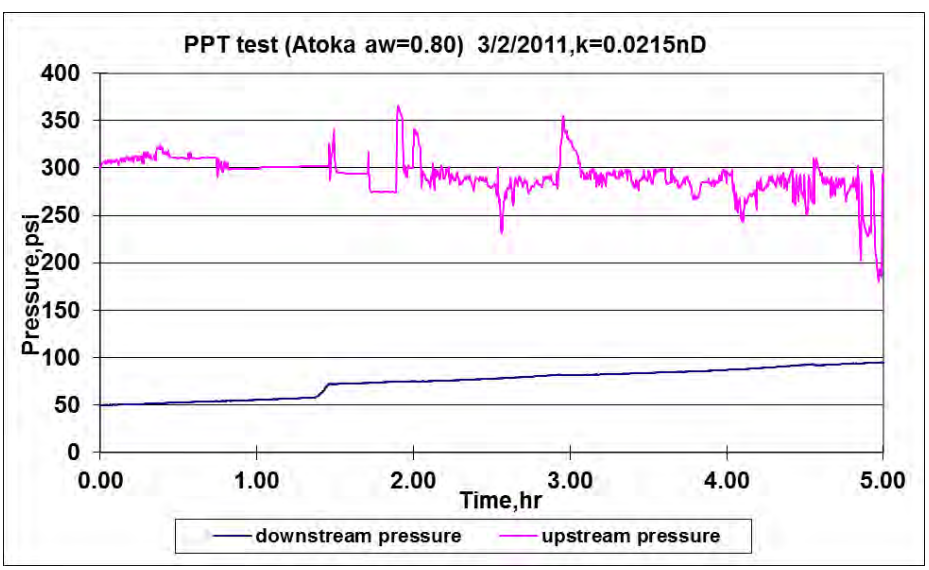

Figure 10.13: Atoka permeability with 2% NP Foam

Figure 10.13 above has a point in the downstream pressure where a rapid increase occurs. The cause of this could be the opening of a small micro-fracture in the shale, of which then

closed up. This jump confirms the speculation from the previous foam step. The most interesting graph in this series is the graph comparing all three curves together. The NP's are behaving as predicted and large reductions in permeability can be observed.

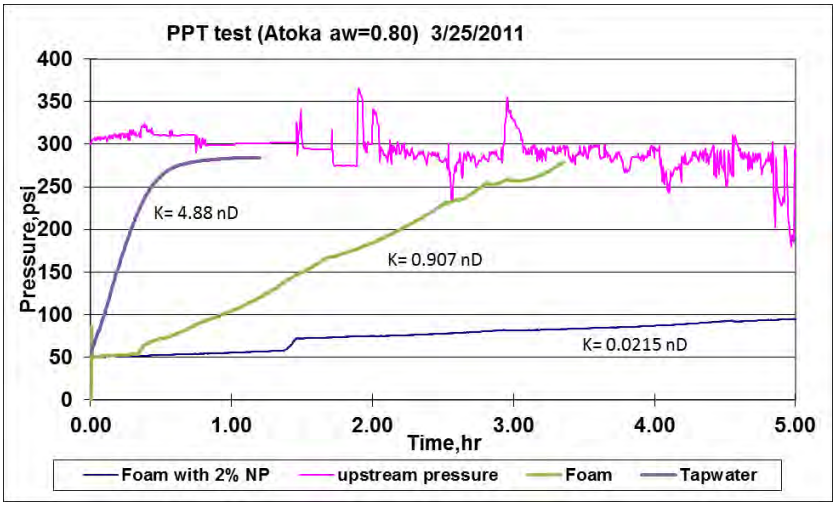

Figure 10.14: Three Step 2% NP Test

From Figure 10.14 above, each successive step in the test displayed a lower permeability, about a whole order of magnitude. After this three step test, a 1000 mL accumulator was installed to allow more control on the flow rate of the injection fluids as well as allowing more foam to be produced for longer tests.

1.3 1% NP Foam Results

The three step test using 1% NP foam as the last step was the first full set of steps to include a 1000 mL accumulator in the flow loop. The following steps were much longer compared to the previous tests. Also, there was a large period of time when all of the samples of shale tested were found to be cracked or fractured. Figure 10.15 below shows the first step in our test using 4% by weight seawater (4% refers to the amount of sea salt added to water).

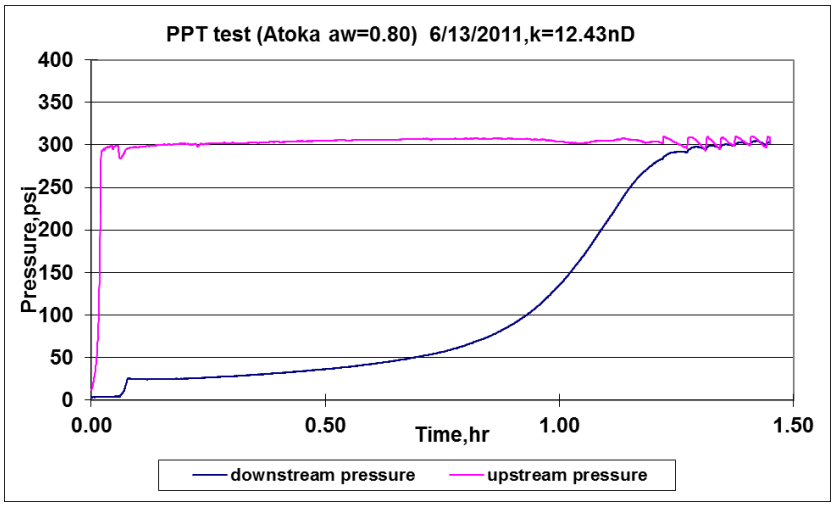

Figure 10.15 Atoka permeability with sea water

Figure 10.15 above shows another Atoka shale sample with seawater as the injection fluid. To combat extra effects due to osmosis, seawater is now used. Seawater has a water activity of 0.98, closer to the water activity of the shale than the tap water previously used. The permeability is a little high, so it is possible the calculated permeability is influenced by a small micro-fracture. It is very close to the generally accepted permeability range resulting in continuation to the foam step of the test. The results from this foam test are shown below in Figure 10.16.

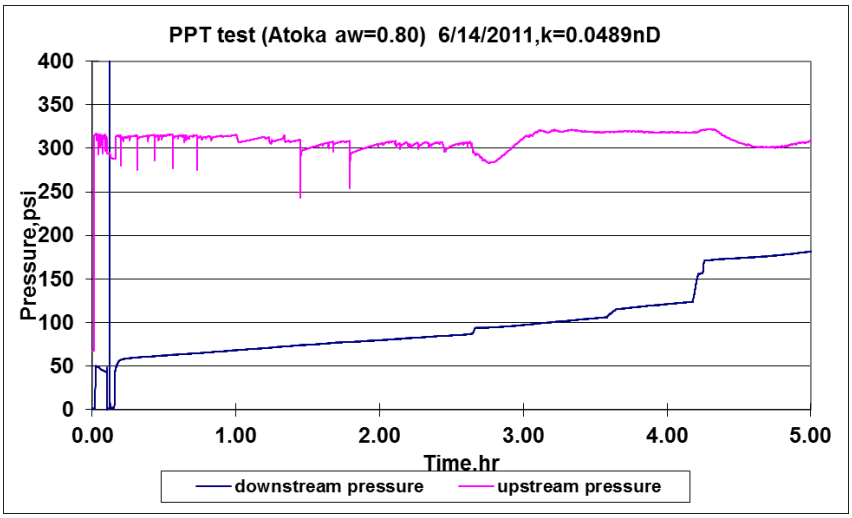

Figure 10.16: Atoka with Foam

As with the other samples, the points of rapid pressure increase are most likely due to small micro-fractures in the shale sample. The smooth parts of the slope however are representative of the fluid flowing through the shale pores. The relatively high entrance pressure of nitrogen restricts the foam from using small micro-fracture as a continuous conduit for flow. The third step of this test using 1% NP foam is shown below in Figure 10.17.

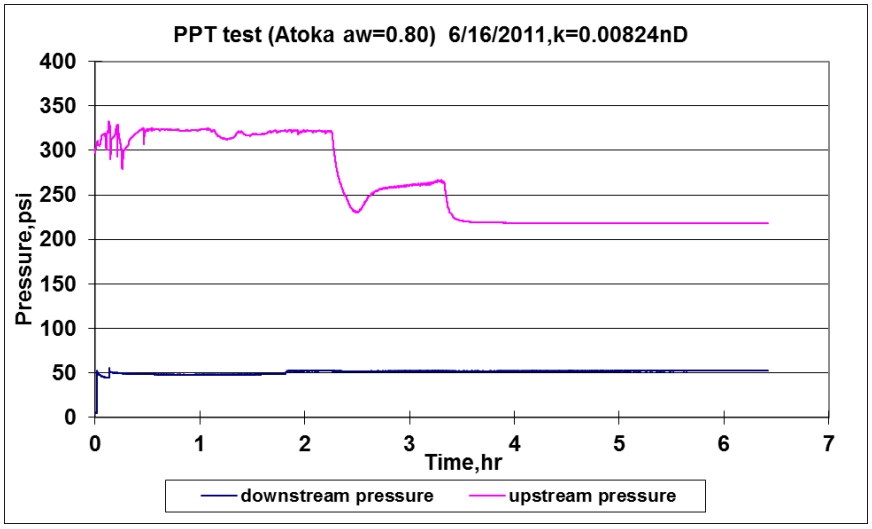

Figure 10.17: Atoka with 1% NP Foam

Figure 10.17 shows that the foam all but plugged up the shale sample, the permeability reduction from normal foam is still almost a whole order of magnitude smaller even at 1% NP concentration in the foam. The drop in pressure in the upstream from is most likely due to a small leak in the back pressure regulator. This can occur when NP's build up around the seal inside. If the back pressure regulator becomes stuck open, the compressibility of foam will cause the foam to flow at a high rate out of the accumulator, hence the relatively short duration of this step. To properly compare the three steps of the test, Figure 10.18 is shown below.

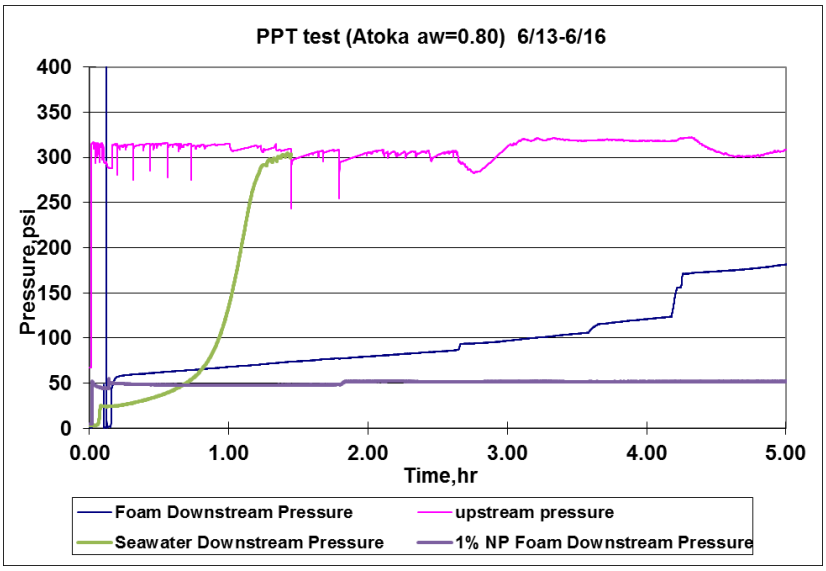

Figure 10.18: 1% NP Foam Three Step Test

Like the earlier tests the permeability of each subsequent step in the test displayed a significantly lower permeability. The 1% NP foam reduced the pressure transmission through the shale sample to an increase of 2 psi in 5 hours.

10.6.1.2 Eagle Ford shale Results

Initial plans for the gas shale were to run a set of tests matching the set of tests on the Atoka shale. When running the Eagle Ford shale samples, large micro-fractures were found to be in most of the samples. Appendix A will introduce some plausible causes for these fractures to occur in the shale. However, one sample was found that was believed to be unfractured. The results for this test are as follows.

1.4 2% NP Foam

Without any other Eagle Ford shale results to compare to, the following test is thought to be a true permeability reading of the rock and not a microfracture. Following these results, pictures of the sample will be included supporting the unfractured assumption. The first step of the 2% NP foam test using the Eagle Ford shale is seawater for comparison to all the other shale samples used. The results are shown in Figure 10.19 below.

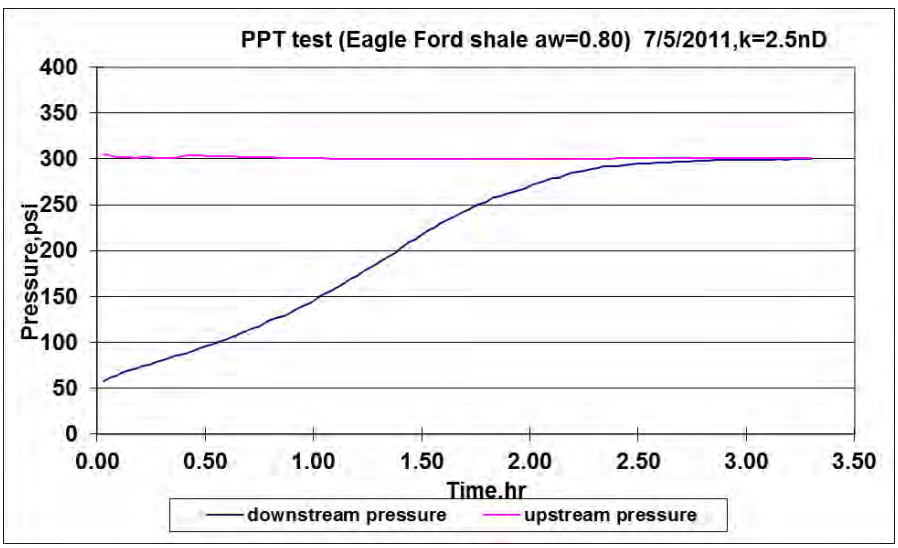

Figure 10.19: Eagle Ford shale with Seawater

The permeability calculated from this test is in the normal permeability range for shale as we have seen in the past. Although this kind of test has never run before using reservoir rock, the pore sizes should be similar in size with Atoka shale and therefore the permeability should be similar to what has been seen with Atoka Shale. The next step in the test is using foam as the injection fluid. Figure 10.20 shown below are the results of using 70% quality foam.

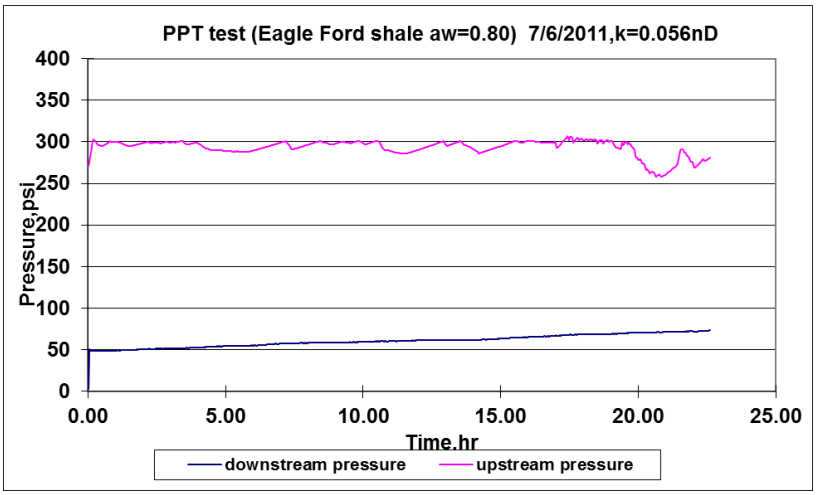

Figure 10.20: Eagle Ford Shale with Foam

The above figure shows the test ran for about 23 hours. This is much longer than the previous tests due to the use of a more accurate and precise injection pump. At 23 hours the 1000 mL accumulator was empty. With the Eagle Ford shale sample, foam displayed a very low permeability, so low the upstream and downstream pressures did not equilibrate. The next step in the test is to run the 2% NP foam as the injection fluid. A very small permeability was expected for the NP foam due to the already small permeability shown with normal foam. Figure 10.21 shown below confirms these expectations.

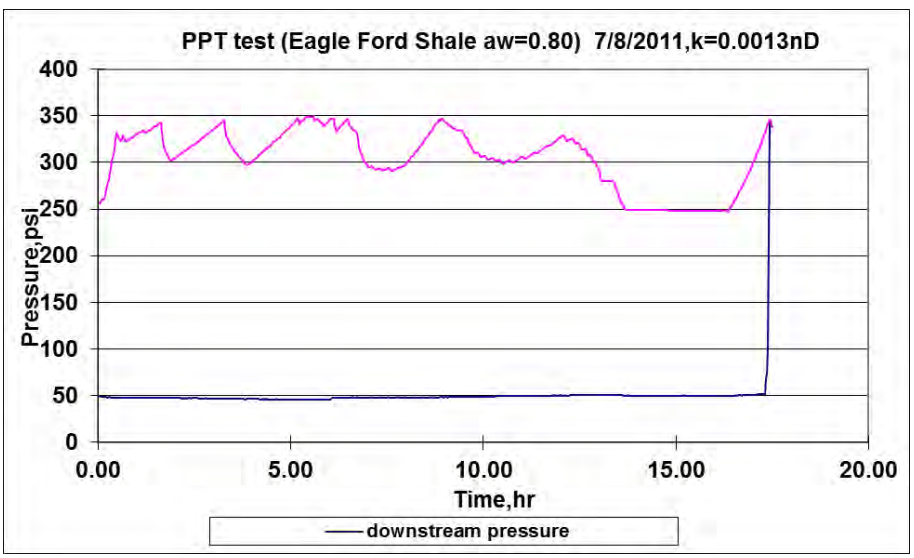

Figure 10.21: Eagle Ford shale with 2% NP Foam

2% NP foam was chosen for this test due to its successful results with Atoka shale. At this time, this was the only sample that was found to be unfractured. At first, the downstream pressure decreased from the initial set 50 psi. This can be a result of osmosis pressure

differences between the seawater on the bottom of the Shale Test Cell and inside the shale sample. The test ended at 17 hours due to the shale cracking at the end. The upstream pressure increased rapidly due to the foam compressing, the shale fatigue point had probably been crossed and the shale cracked. There was, however, plenty of time to calculate a permeability from this step, k = 0.0013 nD. In order to compare the previous Eagle Ford shale results, Figure 10.22 displays all three steps on the same graph shown below.

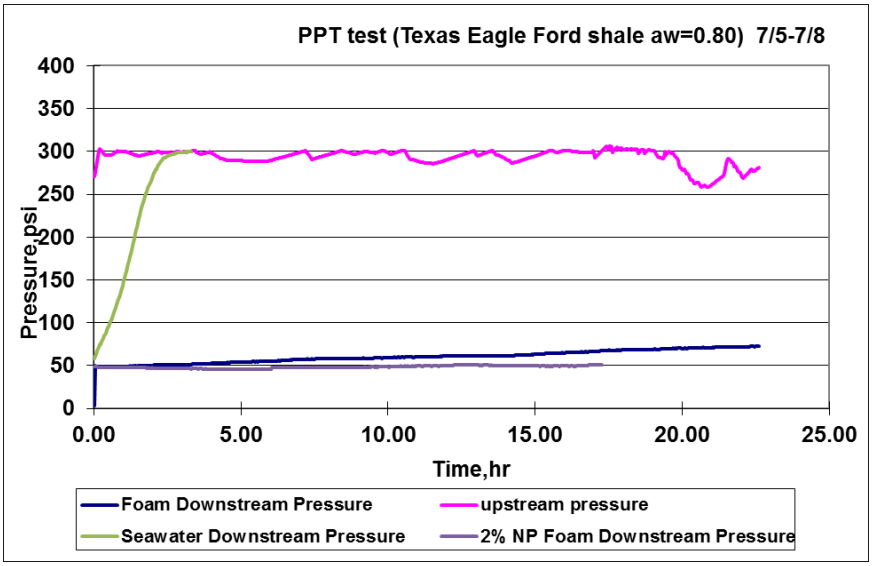

Figure 10.22: Three Step Test with 2% NP Foam

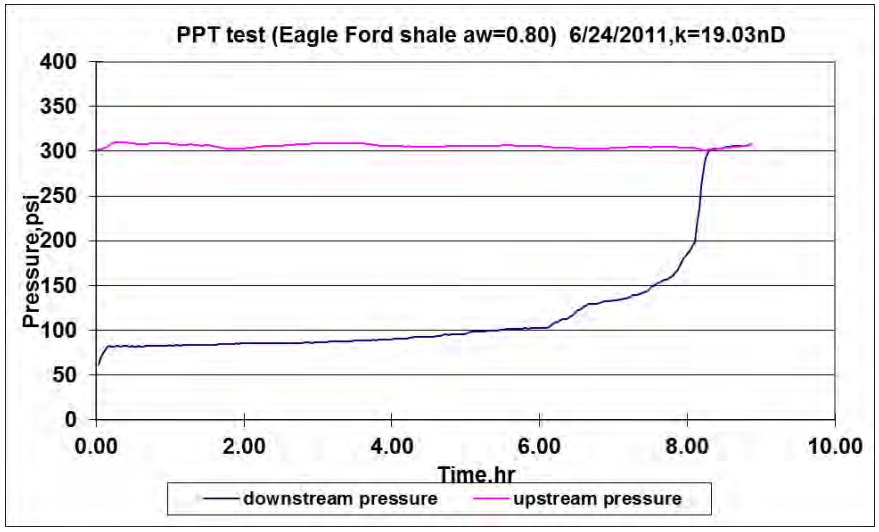

Figure 10.23: Eagle Ford shale with Seawater

Figure 10.23, above, shows the increase in pressure at the beginning of the test is normal. At about 6 hours the downstream pressure rapidly increased without flattening out. This is a great indication of a crack in the shale. The 19.03 nD permeability is an estimate from the steepest part of the curve. After the initial seawater step was run, a Darcy type flow experiment was performed. Pressure was held constant on the top of the shale and a flow rate was recorded using a graduated cylinder and a stopwatch. After which, the permeability of the "crack" was calculated. Figure 10.24 are the results from the Darcy test that held 200 psi constant as the upstream pressure and atmospheric on the downstream pressure.

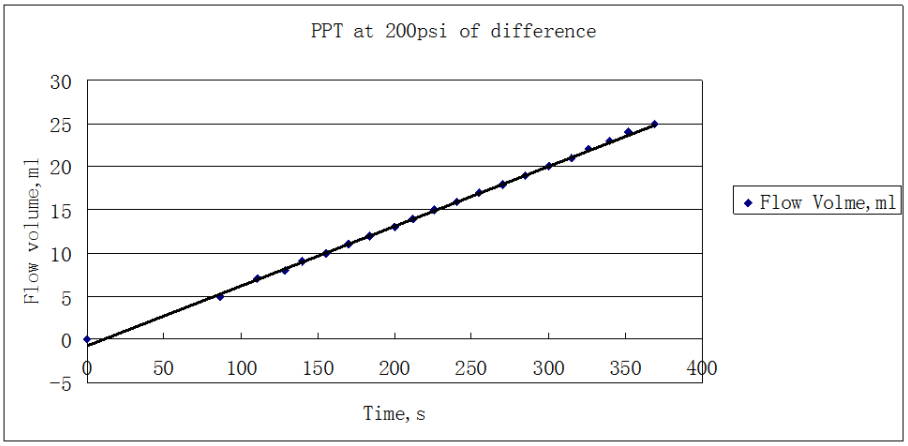

Figure 10.24: Darcy Flow Test with Eagle Ford shale

The resulting permeability is 281999 nD using the typical Darcy permeability equation. Figure 10.25 shows the second Darcy test keeping the upstream pressure to 100 psi and again measuring flow rate and calculating permeability.

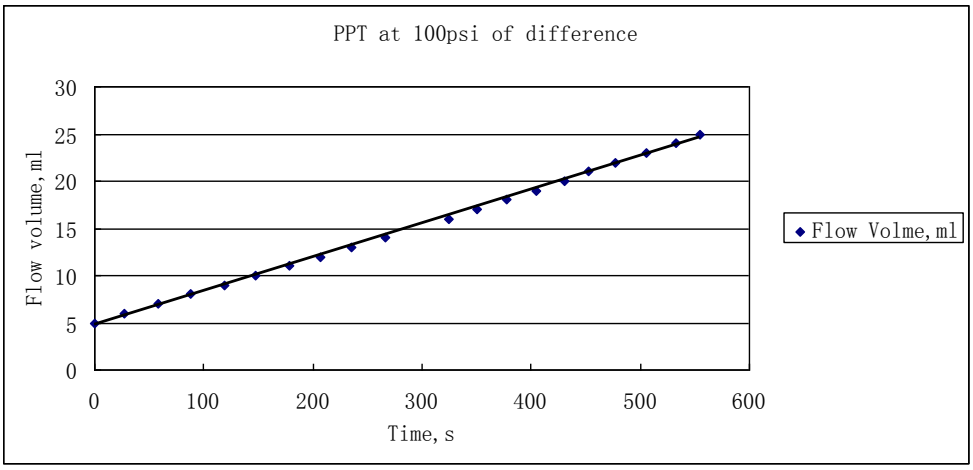

Figure 10.25: Darcy Flow Test with Eagle Ford shale

The resulting permeability from this test is 290964 nD (0.29 mD), and thus confirms the results from the first Darcy test. A permeability this high can only mean that the shale is cracked, observing that the permeability is almost in the milli-Darcy range. To see if the mud could plug this crack we followed the Darcy flow tests with the second step of the original test using a water-based mud. Figure 10.26 shows these results.

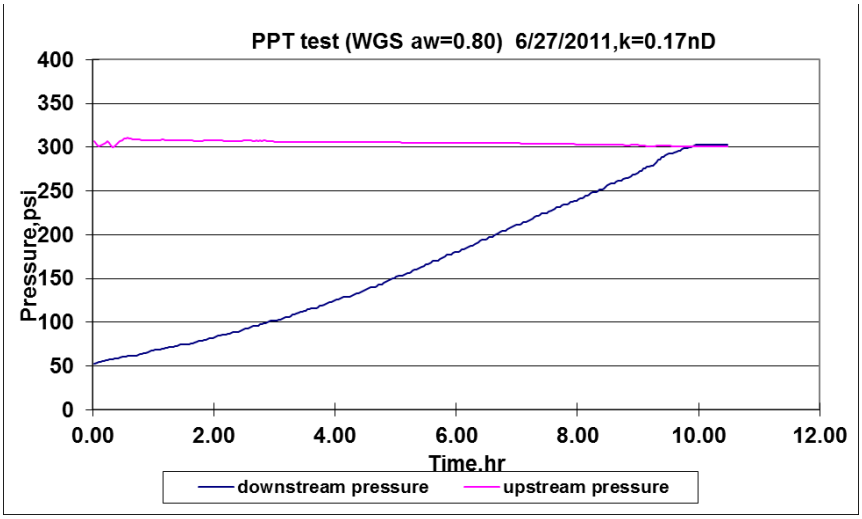

Figure 10.26: Eagle Ford shale with Water-based Mud

Even though the assumption that the shale is cracked, a very smooth curve is generated from this step. The smooth curve and low permeability of this step indicates that the water-based mud created a plug in the fracture or crack in the shale, and thus a normal permeability measurement can be assumed. The subsequent test confirms the assumption that the shale crack is plugged by the mud particles. Figure 10.27, below, shows the result of the same mud with 10 ppb of NP's added as the injection fluid.

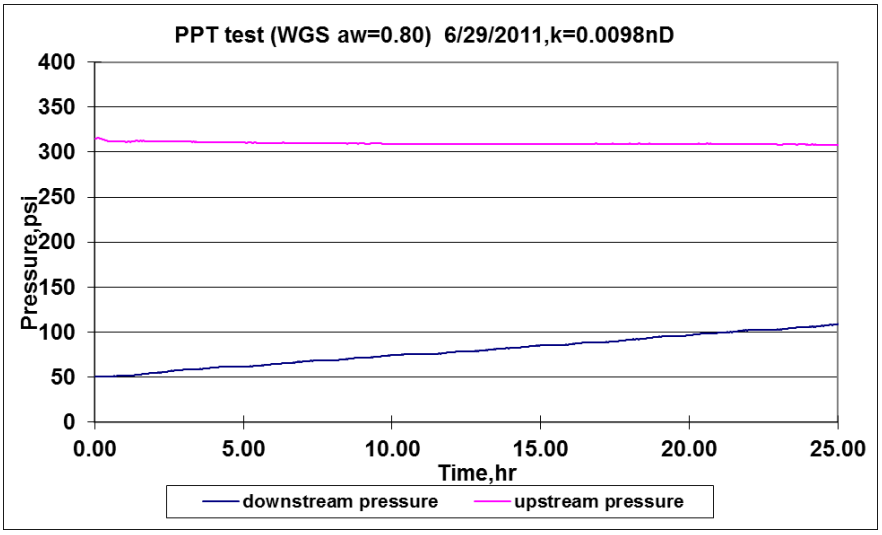

Figure 10.27: Eagle Ford shale with 10 ppb NP Water-based Mud

Comparing the three steps is vital to understanding what is occurring during the test. Figure 10.28, shown below, displays each step on the same time scale for comparison. In Figure 28 below, the permeability labeled "1. k = 0.073 nD" refers to the permeability before the shale cracks. The permeability after the crack is labeled with "2. k = 19.0 nD." The downstream pressure of the seawater step rapidly jumps indicating there is a crack at around 7 hours. After the initial seawater step was run, a Darcy type flow experiment was performed. The mud test, when compared to the seawater test, only partially plugged the crack in the Eagle Ford shale sample due to its permeability being higher than the permeability of the sample before it cracked. The last step of the test using the NP's in the mud seemed to seal off the crack quite well. The resulting permeability from the NP mud is almost a whole order of magnitude lower than the original seawater test, even with the crack. The lower permeability also indicates that the NP's are actually plugging the pores of the shale.

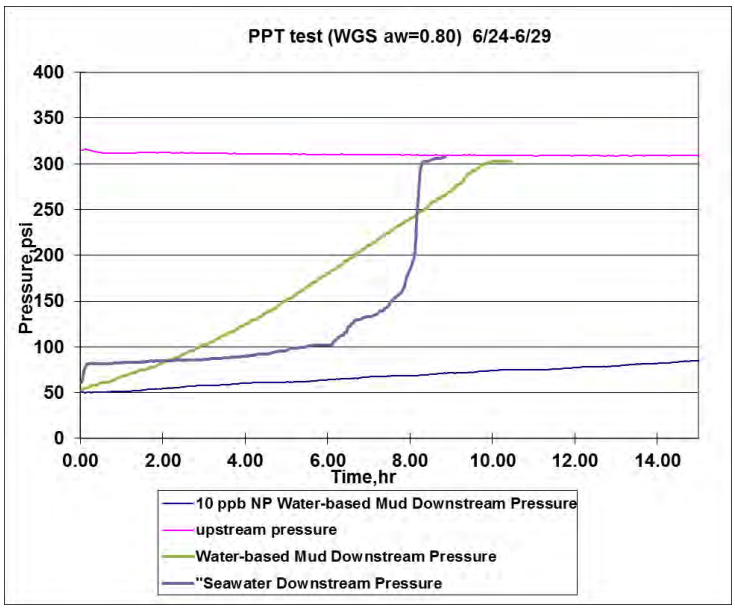

Figure 10.28: Three Step Mud Test with 10 ppb NP Mud

After this test was over, a physical analysis of the shale sample was made. The sample was removed from the Shale Test Cell and cleaned. The surface was then photographed; Figure 10.29 displays cracks in the shale sample.

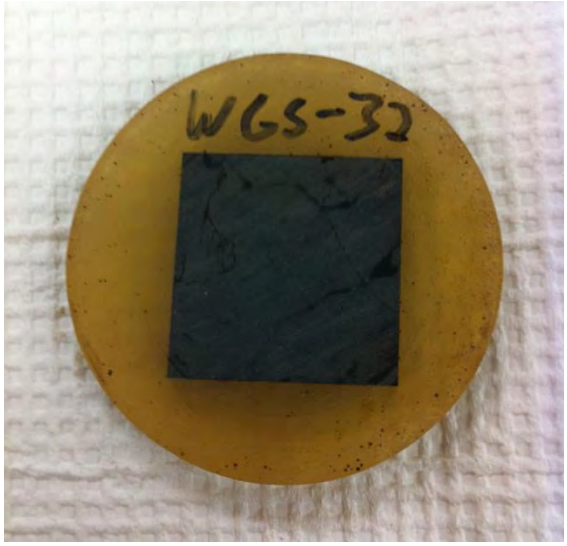

Figure 10.29: Cracked Eagle Ford shale Sample

Looking closely at Figure 10.29, the dark lines in the shale surface are a result of fluid in the cracks of the sample. The surface was wiped clean and then washed with hexane to remove any residue from the mud. The picture was then taken, if too long of a period elapses before a picture is taken the fluid from the cracks will dry up and makes the cracks much more difficult to see. Figure 10.30, below, shows the sample before it was washed as well as a bird's eye view of the cell with a brass ring on top of the sample to allow a gap for mud to flow across the surface.

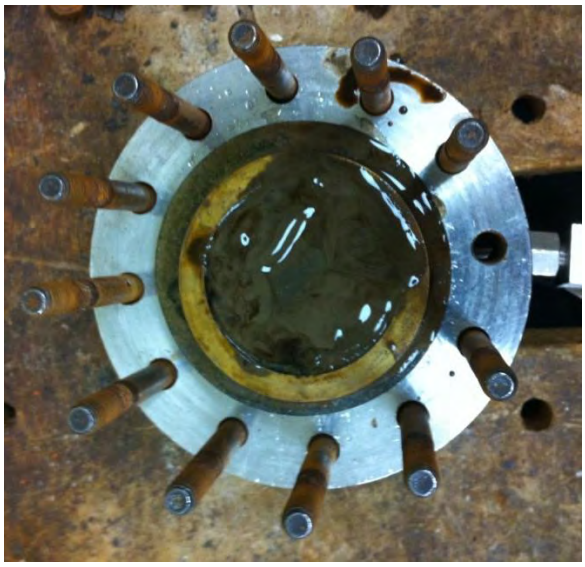

Figure 10.30: Unwashed Eagle Ford shale Sample with Mud in the Shale Test Cell

10.6.1.3 Foam Stability Test Results

After making enough foam to fill the 1000 mL accumulator, the previously mentioned stability tests were run on the foam with the different concentrations of NP's added. Table 1 tabulates the time it took for the foam to break down at atmospheric pressure.

NP Concentration (wt %)	Phase Separation (min)
0%	75
1%	94
2%	130
5%	123

Table 10.1: Phase Separation Time

10.6.2 Discussion

10.6.2.1 Atoka Foam

Quantitative analysis of the permeability results is easier shown using graphical displays. Table 10.2 tabulates the permeability measurements from each test using Atoka Shale.

5% by wt. NP k (nD)			2% by wt. NP k (nD)			1% by wt. NP k (nD)		
Tapwater	Foam	NP Foam	Tapwater	Foam	NP Foam	Seawater	Foam	NP Foam
65.67	0.0887	0.00214	4.88	0.907	0.0215	12.5	0.0489	0.00824

Table 10.2: Permeability Results from Pressure Penetration Tests with Atoka

The color coding used in Table 10.2 is correlated to the shale sample used and is consistent throughout Chapter 5. In order to compare samples, Figures 10.31, 10.32, and 10.33 display the water, foam, and NP foam permeability measurements respectively.

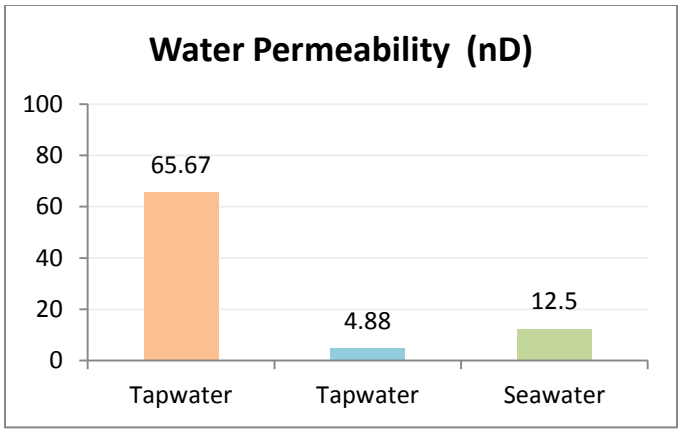

Figure 10.31: Water Permeability Bar Graph

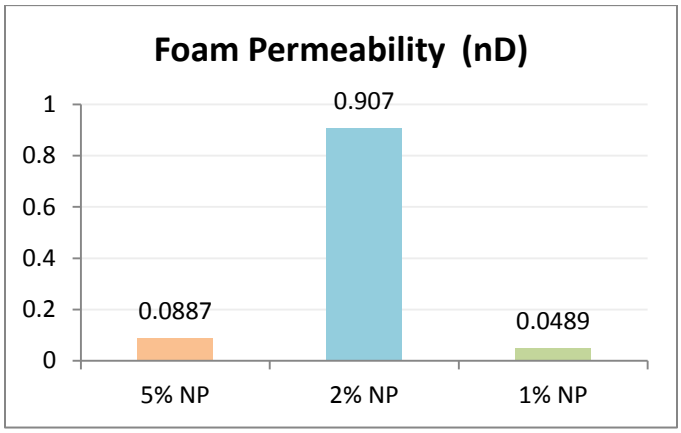

Figure 10.32: Foam Permeability Bar Graph

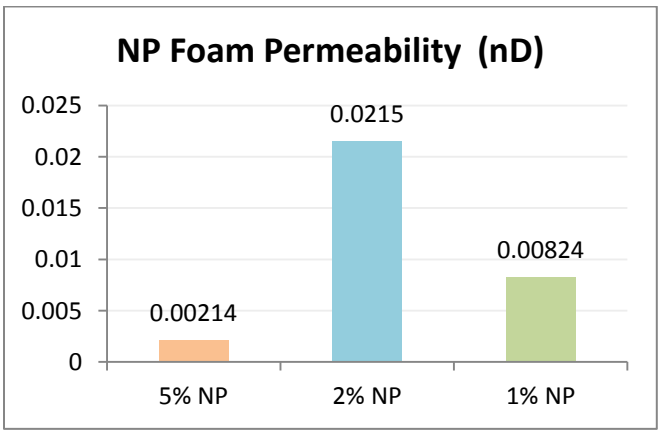

Figure 10.33: NP Foam Permeability Bar Graph

Figure 10.31 and 10.32 show the range of permeability between samples using the same fluids. Figure 10.34 below indicates the reduction of permeability from the water step to the

initial foam without NP's step for each sample run. The 2% NP sample has a lower permeability reduction that the other two samples.

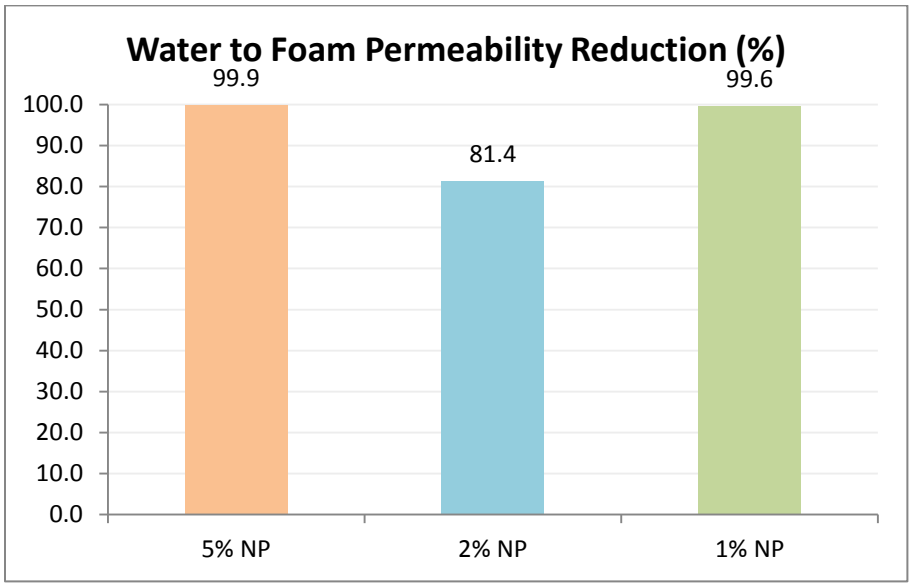

Figure 10.34: Water to Foam Permeability Reduction Bar Graph

The lower permeability reduction could possibly be due to a micro-fracture in the sample that had widened sufficiently to allow foam to pass through the sample. It also could be just a natural phenomenon in variability in the shale sample.

With the assumption that nitrogen cannot enter the pores of the shale and that water can, permeability is reduced by the physical exclusion of water contact to the shale surface by nitrogen due to 70% of the volume of foam being nitrogen. With 70% of that area of the shale not contacting water, a 70% reduction of permeability would be expected as there is a direct correlation between permeability and area contacted. However, these results display an even further reduction in permeability. The surfactant enhanced liquid phase of the foam reduces surface tension between the nitrogen and the liquid film. The reduction in surface tension stabilizes the bubble surface and decreases the break down rate of the foam. When contacting the stable foam with the shale surface, the foam bubbles do not readily break down, thus further limiting the amount of liquid available to flow into the shale. This mechanism of foam stability is likely the cause for the greater than 70% reduction in permeability. Figure 10.35, shown below displays the reduction between the foam and foam with NP's.

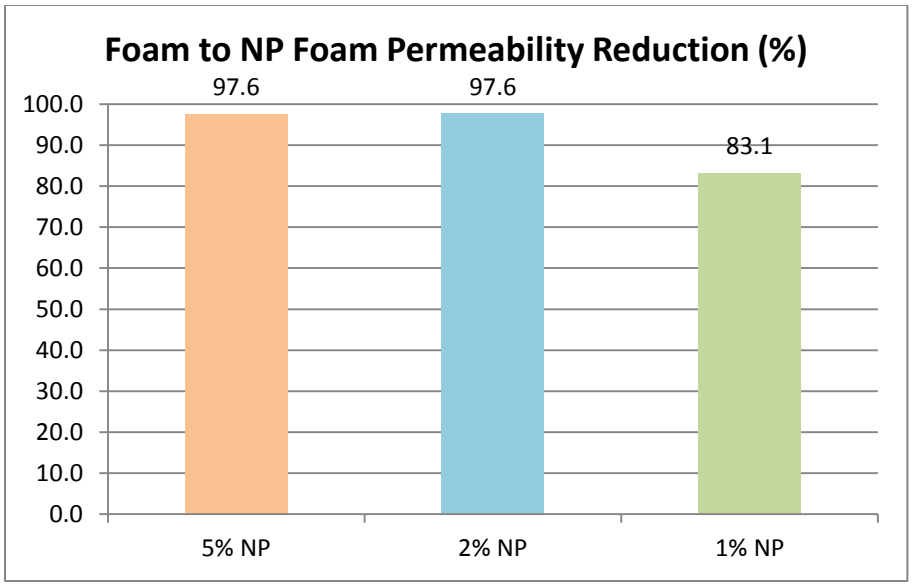

Figure 10.35: Foam to NP Foam Permeability Reduction Bar Graph

Figure 35 suggests that a critical concentration of NP's added to foam exists. At 1% NP's added, the permeability reduction of the foam with NP's decreased to 83.1%. This may also be a natural phenomenon of the shale sample; further testing is needed to solidify this theory.

10.6.2.2 Eagle Ford shale Analysis

Unsure whether the NP's would plug the pore throats of the Eagle Ford shale, a three step mud test and two "Darcy Flow" tests were performed on the Eagle Ford shale. The permeability measurements are tabulated in Table 10.3, shown below.

Step	Test	Injection Fluid	k (nD)
1a	PPT	Seawater	0.073
1b	PPT	Seawater	19
2	DP =200 psi Darcy	Seawater	281999
3	DP =100 psi Darcy	Seawater	290964
4	PPT	Water-based Mud	0.17
5	PPT	10 ppb Water-based Mud	0.0098

Table 10.3: Eagle Ford shale with Water-based Mud (a denotes before crack, b denotes after crack)

The permeability measurements in steps 1-3 above indicate that the shale sample cracked, and the crack was then further widened by the two "Darcy Flow" tests due to the high flow rate of fluid through the crack. After the "Darcy Flow" tests, a Pressure Penetration Test was run using a WBM. The permeability measurement of 0.017 nD from this test suggests that the mud partially plugged the crack in the shale because it is lower than the 19.0 nD recorded in the shale sample using seawater after the crack was formed. After the normal WBM test was performed, the same Pressure Penetration Test was performed using the same mud with the addition of 10 ppb of NP's. The permeability measurement of 0.0098 from this test is a whole order of magnitude smaller than both the normal WBM test as well as the seawater test before the crack formed. This reduction in permeability suggests that the crack was successfully sealed as well as NP's were plugging the pore throats of the shale. This is a very important assumption because it validates the possibility of the Eagle Ford shale being plugged by the NP's.

The major difficulty using this Eagle Ford shale is the ease with which the samples crack. Unlike using mud, foam has no larger solid particles to plug a crack. Many samples were tested, of which only one sample suggested that the shale had no cracks of fractures. Table 10.4 below tabulates the permeability measurements from the one successful Eagle Ford shale sample.

Eagle Ford shale 2% by wt. NP		
Seawater	Foam	NP Foam
2.5	0.056	0.0013

Table 10.4: Permeability Results from Pressure Penetration Tests with Eagle Ford shale

These results receive validity when compared to the Atoka results discussed previously. Figures 10.36 and 10.37, below, shows the permeability reductions compared with the Atoka results.

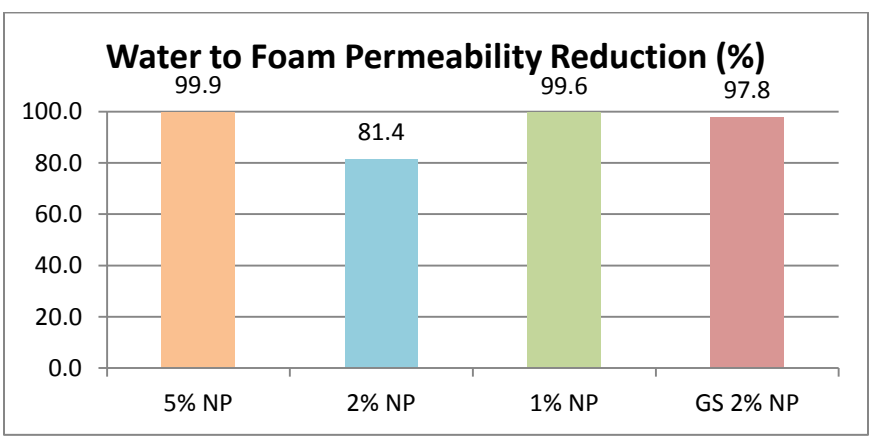

Figure 10.36: Water to Foam Permeability Reduction with Both Shale Cores

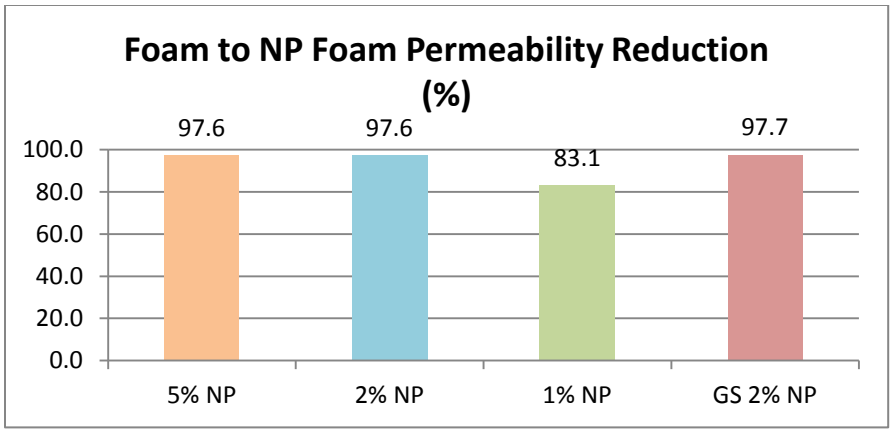

Figure 10.37: Foam to NP Foam Permeability Reduction with Both Shale Cores

Figures 10.36 and 10.37 indicate that the results with the Eagle Ford shale sample are consistent with the Atoka Shale results. Further confirmation that the shale pore-throats were being plugged by NP's was uncovered as the sample of Eagle Ford shale was removed from the Shale Test Cell. Figure 10.38, shown below, has a high gloss coating on the surface of the shale sample. No other chemicals were added to the liquid phase of the foam besides surfactant and NP's. Process of elimination suggests that the sheen displayed below is a layer of NP's aggregating on the shale surface.

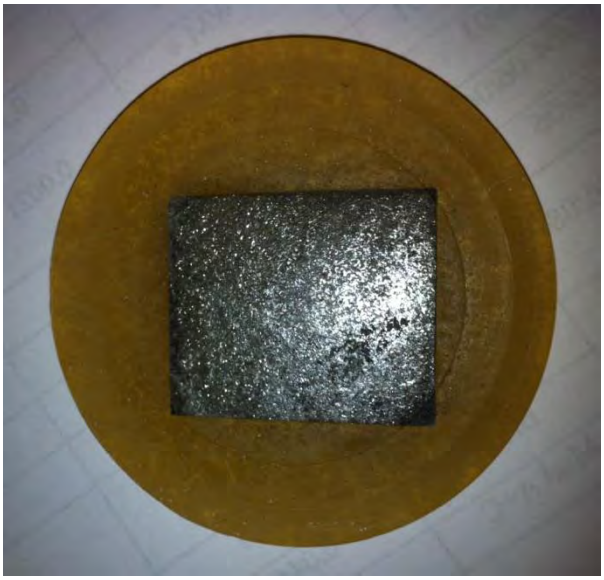

Figure 10.38: Upstream Side of Eagle Ford shale Sample After Three Step 2% NP Foam Test

In order to compare with the original sample appearance the opposite side of the shale sample is shown below in Figure 10.39.

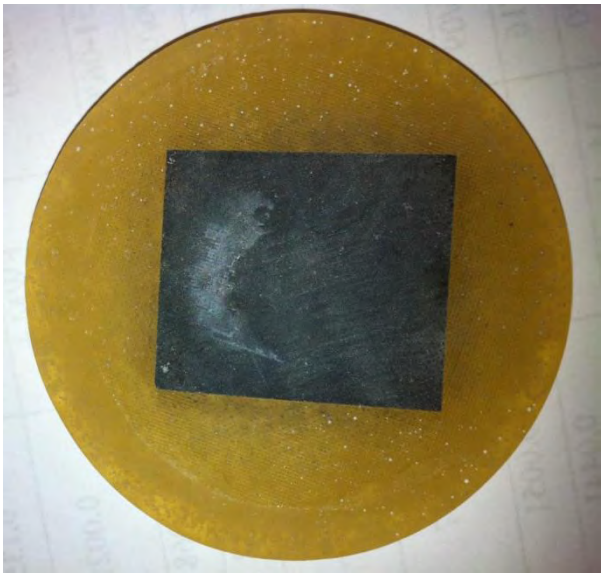

Figure 10.39: Downstream Side of Eagle Ford shale Sample After Three Step 2% NP Foam Test

From these results, it appears that the NP's are indeed plugging the shale pore-throats and partially responsible for the reduction in permeability between the foam and NP foam steps. Further testing of Eagle Ford shale needs to be completed for continued validation of these results.

10.6.2.3 Foam Stability Analysis

When using foam in the field, mud pits may not have the capacity to hold the volume of foam needed to fracture or drill a well. The volume of gas increases as it exits the wellbore due to a reduction in pressure. Standard practice is to break the foam down on the rig floor so the liquid phase of the foam can be reused. To analyze the impact of the addition of NP's on breaking foam down at the rig floor under atmospheric conditions, several "table top" tests were performed to measure the time it takes for the foam to fully separate into separate phases. The results displayed in Table 10.2 are displayed graphically in Figure 10.40, shown below, to better understand the effect NP's have on foam stability at atmospheric pressure.

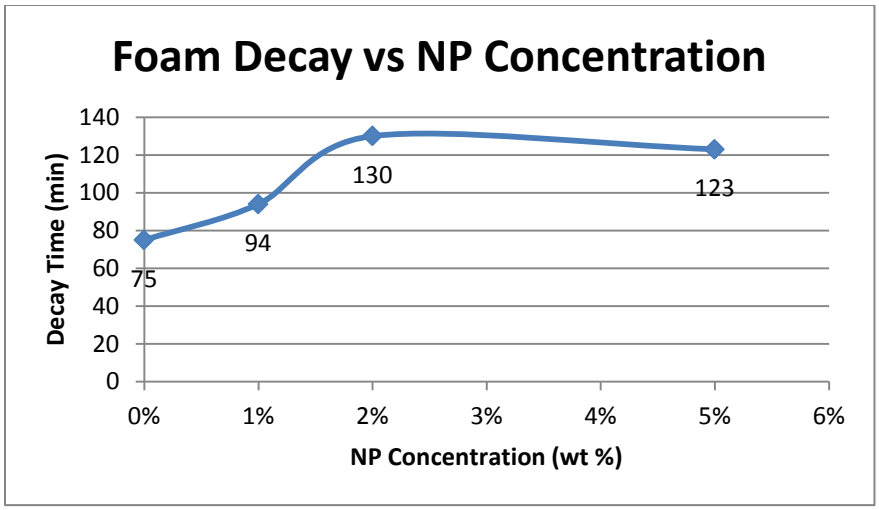

Figure 10.40: Foam Decay vs NP Concentration

The "Foam Decay" time is the time it took for the phases to completely separate. Figure 40 above suggests that a maximum NP concentration exists where increase of additional NP's to the foam decreases the stability of the foam. The extra weight of the NP's as concentration is increased, increases the force of gravity on the bubble surfaces causing an increased rate of drainage for the liquid phase.

The "Pickering Emulsion" predicts an increase in stability of the foam with the addition of solid particles. The increase in stability by adding NP's to the foam is confirmed in Figure 40 by comparing the Decay Time between the foam without the addition of NP's to the 2% addition of NP's. The addition of 2% NP's doubled the Decay Time of the foam. The main concern at the rig floor is the power of the de-foaming agents normally used to break down the foam. Are these de-foaming agents strong enough to break down foam with NP's as well? Further testing is needed to investigate this issue.

10.7 Conclusions

We have investigated the use of nanoparticle stabilized foams for the reduction in permeability of the shale. Based on the experiments conducted, the increased stability of the foam due to the addition of NP's decreases the amount of liquid contacting the shale surface by adding resistance to the breaking of the bubbles in the foam. Similarly to the surfactant used as the foaming agent, the NP's enhance the exclusion of water contacting the shale surface by forming stable bubbles in the foam. The bubbles cannot enter the pore throats due to the higher entrance pressure of nitrogen into the pores of the shale. Another possible mechanism for the reduction of permeability for NP enhanced foam is the plugging of pores by the NP's in the liquid phase of the foam. The liquid that does enter the pore throats contains NP's and has been shown to plug the pore throats of the shale. The physical blocking of the pore throats restricts the flow of water into the pores of the shale. Nanoparticle enhanced foams lower the permeability of both outcrop and reservoir shale formations. These tests clearly indicate that this technology is applicable to both drilling and fracturing fluids. The use of foams has the added advantage that that the volume of water used is reduced dramatically and the amount of nanoparticles used is reduced by an order of magnitude.

10.8 References

Cawiezel, K.E. and Niles, T. D. 1987. Rheological Properties of Foam Fracturing Fluids Under Downhole Conditions. Paper SPE 16191 presented at the SPE Hydrocarbon Economics and Evaluation Symposium in Dallas, Texas, USA, 2-3 March

Espinosa, D., Cladelas, F., Johnston, K., Bryant, S. L., Huh, C. 2010. Nanoparticle-Stabilized Supercritical CO2 Foams for Potential Mobiliy Control Applications. Paper SPE 129925 presented at the SPE Improved Oil Recovery Symposium, Tulsa in Oklahoma, USA, 24-28 April.

Hitchins, R.D and Miller J. M. 2003. A Circulating-Foam Loop for Evaluating Foam at Conditions of Use. This paper (SPE 80242) presented at the SPE International Symposium on Oilfield Chemistry in Houston, Texas, USA, 5–8 February.

Negrao, A.F. and Lage, A. C. V. M. 1997. An Overview of Air/Gas/Foam Drilling in Brazil. Paper SPE 37678 presented at the SPE/IADC Drilling Conference in Amsterdam, The Netherlands, 4-6 March.

Paknejad, A., Schubert, J., and Amani, M. 2009. Key Parameters in Foam Drilling Operations. Paper SPE 122207 presented at the IADC/SPE Managed Pressure Drilling and Underbalanced Operations Conference and Exhibition in San Antonio, Texas, USA, 12-13 February.

Saintpere, S., Herzhaft, B., Toure, A. and Jollet, S. 1999. Rheological Properties of Aqueous Foams for Underbalanced Drilling. Paper SPE 56633 presented at the SPE Annual Technical Conference and Exhibition, Houston, Texas, 3-6 October.

Sensoy, T., Chenevert, M. E., and Sharma, M. M. 2009. Minimizing Water Invasion in Shale Using Nanoparticles. Paper SPE 124429 presented at the SPE Annual Technical Conference and Exhibition in New Orleans, Louisiana, USA, 4-7 October.

Wendorff, C. L. and Earl, R. B. 1983. Foam Fracturing Laboratory. Paper SPE 12025 was presented at the 58th Annual Technical Conference and Exhibition, San Francisco, California, USA, 5-8 October.

Appendix A – Technology Transfer

In accordance with contract, efforts were made to provide technology transfer to the public. The project was showcased either by paper/presentation or display at the following conferences:

- SPE Annual Technical Conference and Exhibition (ATCE) 2012 and 2013
- SPE Offshore Technology Conference (OTC) 2013
- American Rock Mechanics Association (ARMA) 2013
- SPE & AAPG Unconventional Resources Technology Conference (URTEC) 2013

A list of publications is provided below:

1. "The Impact of Shale Preservation on the Petrophysical Properties of Organic-Rich Shales," SPE 166419, prepared for presentation at the 2013 SPE Annual Technical Conference and Exhibition, September 30 – October 2, 2013, New Orleans, LA, U.S.A. Jung, C.M.; Zhou, J.; Chenevert, M.E.; and Sharma, M.M.

2. "A New Standardized Laboratory Protocol to Study the Interaction of Organic-Rich Shales with Drilling and Fracturing Fluids," SPE 166216, prepared for presentation at the 2013 SPE Annual Technical Conference and Exhibition, September 30 – October 2, 2013, New Orleans, LA, U.S.A. Jung, C.M.; Zhou, J.; Pedow, J.W.; Chenevert, M.E.; and Sharma, M.M.

3. "High-Performance Water-Based Mud Using Nanoparticles for Shale Reservoirs," SPE-168799/URTeC ID 1581549, prepared for presentation at the 2013 Unconventional Resources Technology Conference, August 12-14, 2013, Denver, Colorado, USA. Jung, C.M.; Zhang, R., China University of Petroleum; Chenevert, M.E.; Sharma, M.M.

4. "A Systematic Approach to Petrophysical Characterization of Organic-Rich Shales in Barnett and Eagle Ford Formations," SPE 168792/URTeC ID 1581323, prepared for presentation at the 2013 Unconventional Resources Technology Conference, August 12-14, 2013, Denver, Colorado, USA. Zhou, J.; Jung, C.M.; Chenevert, M.E.; Sharma, M.M.

5. "Petrophysical Characterization of Organic-Rich Shales: A New Standardized Protocol," ARMA 13-546, prepared for presentation at the 47th US Rock Mechanics/Geomechanics Symposium, June 23-26, 2013, San Francisco, CA, USA. Zhou, J.; Jung, C.M.; Chenevert, M.E.; Sharma, M.M.

6. "Laboratory Evaluation and Analysis of Physical Shale Inhibition of an Innovative Water-Based Drilling Fluid with Nanoparticles for Drilling Unconventional Shales," SPE 158895, prepared for presentation at the SPE Asia Pacific Oil and Gas Conference and Exhibition, October 22-24, 2012, Perth, Australia. Ji, L., Guo, Q., and Friedheim, J., M-I SWACO; Zhang, R., Chenevert, M.E. and Sharma, M.M.

7. "Decreasing Water Invasion Into Atoka Shale Using Non-modified Silica Nanoparticles," SPE 146979-PA, *SPE Drilling & Completions*, Vol.27, No. 1, pp. 103-112, March 2012,

ISSN 1064-6671, Cai, J., China University of Geosciences, Chenevert, M.E., Sharma M.M., and Friedheim, J. M-I Swaco.

8. "Decreasing Water Invasion into Atoka Shale Using Non-modified Silica Nanoparticles," SPE 146979, 2011 SPE Annual Technical Conference and Exhibition, October 30-November 2, 2011, Denver Colorado, USA Cai, J.; Chenevert, M.E.; Sharma, M.M.; Friedheim, J.

9. "Drilling Unconventional Shales with Innovative Water-Based Mud – Part I: Evaluation of Nanoparticles as a Physical Shale Inhibitor" AADE-12-FTCE-50, 2011 AADE Fluid Technical Conference and Exhibition, April 12-14, 2011, Houston, Texas, USA. Ji, L.; Guo, Q.; Friedheim, J.; Zhang, R.; Chenevert, M.; Sharma, M.M.

10. "Entrance Pressure of Oil-Based Mud Into Shale: Effect of Shale, Water Activity, and Mud Properties," *SPE Drilling & Completion*, Vol. 25, No. 1, pp. 39-44, March 2010, Oleas, A. M.; Osuji, C.E.; Chenevert, M.E.; Sharma, M.M.

11. "Minimizing Water Invasion in Shales Using Nanoparticles," SPE 124429, 2009 SPE Annual Technical Conference and Exhibition, October 4-7, 2009, New Orleans, Louisiana. Sensoy, T.; Chenevert, M.E.; and Sharma, M.M.

List of Tables

Table 2.1: Summary of experimental measurements made on shales and the corresponding sample requirements 12
Table 2.2: Saturated salt solutions and their respective relative humidity 14
Table 3.1: Mineralogy of Atoka, C5 and GOM-12 shales 20
Table 3.2: Mineralogy of TGS, WGS and Barnett shale 20
Table 3.3: Native water activities of seven shales. 21
Table 4.1: Precipitation temperatures of NP dispersions. 24
Table 4.2: 3M two steps test in contact with Atoka shale 25
Table 4.3: 3M 20 nm two step test in contact with Atoka shale 26
Table 4.4: 3M 20 nm three step test on C5 shale 27
Table 4.5: 3M 20 nm 29 wt % test in contact with Atoka shale 28
Table 4.6: 3M 20 nm 5 wt % test in contact with Atoka shale 29
Table 4.7: 3M 20 nm 10 wt % test in contact with Atoka shale 30
Table 4.8: Conditions in Test 5.7. 33
Table 4.9: Conditions in Test 4.8 and 4.9. 34
Table 5.1: Inventory of selected silica nanoparticle dispersions 37
Table 5.2: Composition of Atoka shale 37
Table 5.3: Formulation and properties of fresh water mud 37
Table 5.4: Formulation and properties of thick bentonite mud 38
Table 5.5: Formulation and properties of low solid mud (LSM) 38
Table 5.6: Properties of FWM w/wo NPs after 24 hours @ 176°F and 24 hours aging. 39
Table 5.7: Rheological and filtration performances of bentonite muds w/wo nanoparticles in pressure penetration (PP) tests 39
Table 5.8: Rheological and filtration performances of LSM w/wo nanoparticles in PP tests. 40
Table 5.9: Permeability changes of Atoka shales w/wo nanoparticles in PP tests 40
Table 5.10: Summary of PP tests using pure NP-A dispersion. 41
Table 5.11: Summary of PP tests using pure NP-B dispersion. 41
Table 5.12: Overview of basic three-step PP tests using various NP concentrations. 41
Table 6.1: Field muds properties. 49
Table 6.2: Properties of the field muds modified with CSN-4. 49
Table 6.3: Conditions for Test 6.1. 50
Table 6.4: Conditions for Test 6.2 52
Table 6.5: Composition in Test 6.2 52
Table 6.6: Conditions for Test 6.3. 53
Table 6.7: Conditions for Test 6.4. 55
Table 6.8: Mud composition in Test 6.4. 55
Table 6.9: Conditions for Test 6.5. 56
Table 6.10: Conditions for Test 6.6 58
Table 6.11: Mud composition in Test 6.6 58
Table 6.12: Conditions for Test 6.7. 59

Table 6.13: Conditions for Test 6.8. 61
Table 6.14: Mud composition in Test 6.8. 61
Table 6.15: Permeability values obtained with and without nanoparticles for Atoka 62
Table 6.16: Conditions for Test 6.9. 63
Table 6.17: Conditions for Test 6.10. 65
Table 6.18: Mud compostion in Test 6.10 65
Table 6.19: Conditions for Test 6.11. 66
Table 6.20: Conditions for Test 6.12. 68
Table 6.21: Mud composition in Test 6.12. 68
Table 6.22: Conditions for Test 6.13. 69
Table 6.23: Conditions for Test 6.14. 71
Table 6.24: Mud composition in Test 6.14 71
Table 6.25: Conditions for Test 6.15. 72
Table 6.26: Conditions for Test 6.16. 74
Table 6.27: Composition in Test 6.16. 74
Table 6.28: Conditions for Test 6.17 75
Table 6.29: Permeability values obtained with and without nanoparticles for GOM shale 76
Table 7.1: Mud properties (Ji et al., 2012) 79
Table 7.2: Permeability results for Texas Gas Shale 80
Table 9.1: Original fluid contents of Eagle Ford shale 95
Table 9.2: Physical properties of Eagle Ford shale 95
Table 9.3: Brinell hardness change before and after swelling 97
Table 9.4: P and S wave velocity 97
Table 9.5: Young's modulus and Poisson's ratio result 98
Table 9.6: Summary of test results 101
Table 10.1: Phase Separation Time 127
Table 10.2: Permeability Results from Pressure Penetration Tests with Atoka 127
Table 10.3: Eagle Ford shale with Water-based Mud (a denotes before crack, b denotes after crack) 130
Table 10.4: Permeability Results from Pressure Penetration Tests with Eagle Ford shale 131

List of Figures

Figure 2.1: Oil-cooled coring machines to cut large (left) and small (right) shale samples. 13
Figure 2.2: Shale samples prepared for characterization: (a) a cube, (b) a disk, and (c) a column. 13
Figure 2.3: Sample preparation procedure for the permeability test. 14
Figure 2.4: Adsorption isotherm test to determine shale's native water activity. 15
Figure 2.5: Side view of one swelling gauge with shale sample. 15
Figure 2.6: Pulse transmission set-up for measuring the acoustic wave velocities of shales. 17
Figure 2.7: Pressure penetration test and compressibility test set-up. 18
Figure 2.8: Downstream pressure build-up and graphical slope interpretation of dimensionless pressure versus time. 18
Figure 2.9: Brine compressibility test result and compressibility calculation equation. 19
Figure 3.1: Ternary diagram that shows the relative abundance of quartz, calcite and clay 21
Figure 3.2: Adsorption isotherms for determining the native water activities of shales 22
Figure 4.1: C5 Shale swelling test performed with fresh water and NP dispersion. 24
Figure 4.2: Three steps test in contact with Atoka shale 25
Figure 4.3: Two step test with and without NP 26
Figure 4.4: Three step test with C5 shale without and with NP 27
Figure 4.5: Results of the Atoka/ 29 wt % NP dispersion test. 28
Figure 4.6: Results of the Atoka/ 5 wt % NP dispersion test. 29
Figure 4.7: Results of the Atoka/ 10 wt % NP dispersion test. 30
Figure 4.8: NP tests with different concentrations in contact with Atoka shale. 31
Figure 4.9: SEM of 20 nm particles in contact with Atoka shale. (Dotted scale is 375 nm) 31
Figure 4.10: 20 nm silica NP in different scale 32
Figure 4.11: Group of particles plugged a pore throat 32
Figure 4.12. Results of the Test 4.8 which was performed with CSN-4 40 wt % 20 nm dispersion. 33
Figure 4.13. 3M's 17 wt % and CSN-3 dispersions in contact with Atoka. 34
Figure 5.1: Particle size scale, adapted from Abrams (1970) 44
Figure 5.2: Continuous PP plot of Atoka Shale 21B, in Bentonite Mud Containing NP-A 44
Figure 5.3: Continuous PP plot of Atoka shale 18B Contacted with Bentonite Mud Containing NP-B 45
Figure 5.4: Continuous PP plot of Atoka shale 34C in LSM Containing NP-A 45
Figure 5.5: Continuous PP plot of Atoka shale 33C Contacted by LSM Containing NP-B 46
Figure 5.6: Permeability Reduction of Atoka shale with bentonite mud w/wo NPs 46
Figure 5.7: Permeability Reduction of Atoka shale with LSM w/wo NPs 47
Figure 5.8: Effect of NP size on permeability reduction percent (Δk, %) 47

Figure 5.9: Effect of NP concentration in pure dispersions on permeability reduction percent 48
Figure 5.10: Effect of NP concentration in muds on permeability reduction percent 48
Figure 6.1: Results of Test 6.1 that was performed in contact with Atoka shale. 50
Figure 6.2: Results of Test 6.2 that was performed in contact with Atoka shale. 51
Figure 6.3: Comparison of Mud A with and without NP in contact with Atoka shale. 51
Figure 6.4: Results of Test 6.3 that was performed in contact with Atoka shale. 53
Figure 6.5: Results of Test 6.4 that was performed in contact with Atoka shale. 54
Figure 6.6: Comparison of Mud B with and without NP in contact with Atoka shale. 54
Figure 6.7: Results of Test 6.5 that was performed in contact with Atoka shale. 56
Figure 6.8: Results of Test 6.6 that was performed in contact with Atoka shale. 57
Figure 6.11: Comparison of Mud C with and without NP in contact with Atoka shale. 57
Figure 6.10: Results of Test 6.7 that was performed in contact with Atoka shale. 59
Figure 6.11: Results of Test 6.8 that was performed in contact with Atoka shale. 60
Figure 6.12: Comparison of Mud D with and without NP in contact with Atoka shale. 60
Figure 6.13: Permeability chart of Atoka shale 62
Figure 6.14: Results of Test 6.9 that was performed in contact with GOM shale. 63
Figure 6.15: Results of Test 6.10 that was performed in contact with GOM shale. 64
Figure 6.16: Comparison of Mud A with and without NP in contact with GOM shale. 64
Figure 6.17: Results of Test 6.11 that was performed in contact with GOM shale. 66
Figure 6.18: Results of Test 6.12 that was performed in contact with GOM shale. 67
Figure 6.19: Comparison of Mud B with and without NP in contact with GOM shale. 67
Figure 6.20: Results of Test 6.13 that was performed in contact with GOM shale. 69
Figure 6.21: Results of Test 6.14 that was performed in contact with GOM shale. 70
Figure 6.22: Comparison of Mud C with and without NP in contact with GOM shale. 70
Figure 6.23: Results of Test 6.15 that was performed in contact with GOM shale. 72
Figure 6.24: Results of Test 6.16 that was performed in contact with GOM shale. 73
Figure 6.25: Comparison of Mud D with and without NP in contact with GOM shale. 73
Figure 6.26: Results of Test 6.17 that was performed in contact with GOM shale. 75
Figure 6.27: Permeability chart of GOM shale. 76
Figure 7.1: SEM image of Texas gas shale: (a) original surface, (b) ion-milled surface with dual beam SEM/FIB, and (c) pore throat size of shale 79
Figure 7.2: Permeability reduction result chart 81
Figure 8.1: Swelling of TGS after exposed to fresh water, 4% NaCl and 2% KCl for 24 hours. 86
Figure 8.2: Weight change of TGS after exposed to fresh water, 4% NaCl and 2% KCl for 24 hours. 86

Figure 8.3: Swelling of WGS after exposed to fresh water, 4% NaCl and 2% KCl for 24 hours. 87
Figure 8.4: Weight change of WGS after exposed to fresh water, 4% NaCl and 2% KCl for 24 hours. 87
Figure 8.5: Swelling of Barnett shale after exposed to fresh water and 4% seawater for 24 hours. 88
Figure 8.6: Weight change of Barnett shale after exposed to fresh water and 4% seawater for 24 hours. 88
Figure 8.7: Brinell hardness of TGS after exposed to fresh water, 4% NaCl and 2% KCl for 24 hours. 89
Figure 8.8: Brinell hardness of WGS after exposed to fresh water, 4% NaCl and 2% KCl for 24 hours. 89
Figure 8.9: Brinell hardness of Barnett shale after exposed to fresh water and 4% seawater for 24 hours. 90
Figure 8.10: Wave velocity of TGS before and after immersed in fresh water, 4% NaCl and 2% KCl for 24 hours perpendicular (a) and parallel to bedding planes (b). 90
Figure 8.11: Wave velocity of WGS before and after immersed in fresh water, 4% NaCl and 2% KCl for 24 hours perpendicular (a) and parallel to bedding planes (b). 91
Figure 8.12: Wave velocity of Barnett shale before and after immersed in fresh water and 4% seawater for 24 hours perpendicular (a) and parallel to bedding planes (b). 91
Figure 8.13: Young's modulus (a) and Poisson's ratio (b) of TGS before and after immersed in fresh water, 4% NaCl and 2% KCl for 24 hours. 92
Figure 8.14: Young's modulus (a) and Poisson's ratio (b) of WGS before and after immersed in fresh water, 4% NaCl and 2% KCl for 24 hours. 92
Figure. 8.15: Young's modulus (a) and Poisson's ratio (b) of the Barnett shale before and after immersed in fresh water and 4% seawater for 24 hours. 92
Figure 9.1: Sample dimension for swelling test. 96
Figure 9.2: Weight change of the dry sample and the preserved sample before and after the swelling with 4wt% NaCl sea water. 96
Figure 9.3: Brinell hardness of shale before and after immersion in 4wt% NaCl for 24 hours. 97
Figure 9.4: Wave velocity result (a) perpendicular to bedding planes and (b) parallel to bedding planes 98
Figure 9.5: (a) Young's modulus change and (b) Poisson's ratio change of dry and preserved samples under swelling 99
Figure 9.6: Sea water permeability results of preserved sample from pressure penetration tests 100
Figure 9.7: Sea water permeability results of dried-out sample from pressure penetration tests 100
Figure 9.8: Nitogen permeability results of dried-out sample from pressure penetration tests 100
Figure 10.1: Flow Diagram of Foam Flow Loop 107
Figure 10.2: Flow Diagram of Pressure Penetration Cell 107

Figure 10.3: Left Half of the Foam Loop 109
Figure 10.4: Shale Test Cell and Pressure Transducers 109
Figure 10.5: Close View of the Left Half of the Foam Loop 110
Figure 10.6: Foam Viewing Cell with Quick Connects 110
Figure 10.7: Atoka Shale permeability with tap water 113
Figure 10.8: Atoka permeability with Foam 113
Figure 10.9: Atoka permeability with 5% NP Foam 114
Figure 10.10: Three Step 5% NP Foam Test 114
Figure 10.11: Atoka permeability with tap water 115
Figure 10.12: Atoka permeability with Foam 116
Figure 10.13: Atoka permeability with 2% NP Foam 116
Figure 10.14: Three Step 2% NP Test 117
Figure 10.15 Atoka permeability with sea water 118
Figure 10.16: Atoka with Foam 118
Figure 10.17: Atoka with 1% NP Foam 119
Figure 10.18: 1% NP Foam Three Step Test 119
Figure 10.19: Eagle Ford shale with Seawater 120
Figure 10.20: Eagle Ford Shale with Foam 121
Figure 10.21: Eagle Ford shale with 2% NP Foam 121
Figure 10.22: Three Step Test with 2% NP Foam 122
Figure 10.23: Eagle Ford shale with Seawater 122
Figure 10.24: Darcy Flow Test with Eagle Ford shale 123
Figure 10.25: Darcy Flow Test with Eagle Ford shale 123
Figure 10.26: Eagle Ford shale with Water-based Mud 124
Figure 10.27: Eagle Ford shale with 10 ppb NP Water-based Mud 124
Figure 10.28: Three Step Mud Test with 10 ppb NP Mud 125
Figure 10.29: Cracked Eagle Ford shale Sample 126
Figure 10.30: Unwashed Eagle Ford shale Sample with Mud in the Shale Test Cell 126
Figure 10.31: Water Permeability Bar Graph 128
Figure 10.32: Foam Permeability Bar Graph 128
Figure 10.33: NP Foam Permeability Bar Graph 128
Figure 10.34: Water to Foam Permeability Reduction Bar Graph 129
Figure 10.35: Foam to NP Foam Permeability Reduction Bar Graph 130
Figure 10.36: Water to Foam Permeability Reduction with Both Shale Cores 131
Figure 10.37: Foam to NP Foam Permeability Reduction with Both Shale Cores 132
Figure 10.38: Upstream Side of Eagle Ford shale Sample After Three Step 2% NP Foam Test 132
Figure 10.39: Downstream Side of Eagle Ford shale Sample After Three Step 2% NP Foam Test 133
Figure 10.40: Foam Decay vs NP Concentration 134